UNIVERSIDAD DE CONCEPCIÓN
FACULTAD DE CIENCIAS FÍSICAS Y MATEMÁTICAS
DEPARTAMENTO DE FÍSICA

TESIS DE MAGÍSTER

ACTIVE CARPETS AT VISCOUS INTERFACES

POR

Felipe Andrés Barros Cárdenas

Directores de Tesis: Dra. Francisca Guzmán Lastra
Dr. Juan Pablo Staforelli
Comité evaluador: Dr. Hugo Ulloa
Dr. Roberto Navarro
Dr. Héctor Sepúlveda

20 de Noviembre de 2024.
Concepción, Chile.

DOCUMENTO PRESENTADO A LA FACULTAD DE CIENCIAS FÍSICAS Y MATEMÁTICAS DE LA UNIVERSIDAD DE CONCEPCIÓN EN CUMPLIMIENTO PARCIAL DE LOS REQUERIMIENTOS PARA EL GRADO DE MAGÍSTER EN CIENCIAS CON MENCIÓN EN FÍSICA.

A mis padres.

AGRADECIMIENTOS

Agradezco profundamente a todas las personas que contribuyeron a este proyecto. Valoro mucho el tiempo y esfuerzo que dedicaron a mi y al desarrollo de esta investigación. Asimismo, agradezco a las personas cercanas a mi por su apoyo a lo largo de este proceso.

Este trabajo fue patrocinado por ANID a través de Núcleo Milenio Física de la Materia Activa NCN19 170, Fondecyt Regular 11220683 y realizado parcialmente con el apoyo del Laboratorio Nacional de Computación de Alto Rendimiento (NLHPC).

Contents

List of Figures

Resumen

Los entornos acuáticos de la Tierra y el cuerpo humano presentan sistemas estratificados en los que las interfaces entre las capas albergan nadadores microbianos en colonias conocidas como *alfombras activas*. Se ha demostrado anteriormente que estos nadadores mejoran la difusión térmica y el transporte de masas en medios semi-infinitos. Este estudio investiga la dinámica de fluidos de las “alfombras activas" en capas confinadas, como las llamadas *slicks* en masas de agua. Presentamos hallazgos novedosos sobre las fluctuaciones hidrodinámicas en medios confinados en los que varía la viscosidad del fluido. Nuestros resultados identifican tres regiones de fluctuación: las fluctuaciones verticales dominan cerca de la alfombra activa y la interfaz (Región I), las fluctuaciones isotrópicas se producen más arriba (Región II), y las fluctuaciones horizontales prevalecen cerca de la superficie (Región III). La extensión de estas regiones varía con el espesor de la capa y los cambios de viscosidad. También encontramos estructuras de flujo a gran escala dentro de estas capas confinadas, lo que ofrece nuevas perspectivas sobre la capacidad de mezcla de los sistemas biogénicos y posibles aplicaciones en ecología y bioingeniería.

Abstract

Earth's aquatic environments and human body feature layered systems where interfaces between layers host microbial swimmers in colonies known as *Active Carpets*. These swimmers have previously been shown to enhance thermal diffusion and mass transport in semi-infinite media. This study investigates the fluid dynamics of *Active Carpets* in confined layers, such as slicks on water bodies. We present novel findings on hydrodynamic fluctuations within confined environments where the fluid viscosity varies. Our results identify three regions of fluctuation: vertical fluctuations dominate near the *Active Carpet* and interface (Region I), isotropic fluctuations occur further up (Region II), and horizontal fluctuations prevail near the surface (Region III). These regions' extents vary with layer thickness and viscosity changes. We also discover large-scale flow structures within these confined layers, offering new insights into biogenic systems' mixing capacity and potential applications in ecology and bioengineering.

Chapter 1

Introduction

In nature, biological activity is often densely concentrated and covers large areas on solid or soft surfaces, forming boundary-driven fluctuations that stir the fluid around and generate globally directed flows and transport [1, 2]. These accumulations are found across different length scales, from cytoskeletal elements at the cell cortex to microorganisms accumulating near fluid-fluid interfaces or close to rigid surfaces forming biofilms [3, 4, 5, 6, 7, 8, 9, 10, 11]. In such crowded and confined environments, transporting molecules, suspended particles, and fluids are crucial for maintaining continuous biological processes. These include clearing pathogens, creating feeding currents, locomotion of reproductive cells, self-cleaning, and cargo transport, which have direct implications for various fields, including microfluidics and life sciences [12, 13, 14].

The emergence of these large quasi-two-dimensional boundary accumulations, termed *Active Carpets*, is a response to various taxis, such as viscosity or light in marine microorganisms, hydrodynamic interactions, mechanical responses, and optimization of metabolic activities [3, 15, 16, 17, 18, 19]. These accumulations change the spatial distribution of microorganisms on stratified environments characterized by abrupt gradients in fluid properties, including temperature (thermocline), salinity (haloclines), density (pycnoclines), dissolved oxygen (oxycline), dissolved chemicals (chemoclines), or sharp shifts in viscosity [20, 4, 21, 22, 23, 24, 25]. As an example, photosynthetic microbes habit around the thermocline, the zone of maximum vertical temperature gradient in the water column, separating the upper warmer layer from the deeper, nutrient-enriched colder layer [26, 15, 27]. Moreover, most of Earth's aquatic systems are capped by the air-water interface, the free surface where the atmosphere meets waters holding thin oil films or slicks lying at their surfaces. Such a layering environment creates a wide range of niches for microbial swimmers and inert suspended matter [6, 28, 29, 30], as well as vertical confinement that may control the ability of microbes to harvest food and self-clean via collective hydrodynamic fluctuations. Biogenic hydrodynamic stirring has been proved to enhance active diffusion [31, 32, 33, 34, 35, 36, 37, 38], generate persistent flows for feeding processes in collective and single microswimmers [1, 9, 39], produce aggregation [40, 41, 42, 43, 14, 44] and induce long-range hydrodynamic fluctuations [45, 46].

In [41], Aguayo et al. recently studied the hydrodynamic fluctuations induced by *Active Carpets* formed by dipole microswimmers organized into a thin layer beneath the free surface of a semi-infinite homogeneous fluid. The authors found that the hydrodynamics fluctuations produce anisotropic diffusion that decays slowly with distance, showing a remarkable biogenic long-range effect on vertical transport. In a different aspect, artificial carpets made of soft microswimmers, mimicking cilia and reacting to magnetic, light, and electric stimuli to generate transport, have gained interest in fluid manipulation. These carpets have demonstrated increasing potential in cargo delivery and fluid pumping, offering also a valuable experimental setup to study active carpets [47, 48, 49, 50, 51].

Vertical transport is essential for mixing and ventilation in stratified environments. A long-debated question is whether swimming organisms contribute to such processes in aquatic systems [52, 53]. To uncover the role of microorganisms in stratified liquid systems, Ardekani and Stocker [54] employed the multipole expansion technique to examine a single microswimmer known as stratlet. According to the biophysics operating at the micro-scale, the stratlet model considers an organism moving at low Reynolds numbers, $Re \ll 1$, in which viscous forces dominate over inertial ones. Their findings revealed that pullers moving in a stratified fluid do not generate persistent flows conducive to vertical mixing. Instead,

stratlets induce in-plane flows that strengthen the existing stratification [54]. Theoretical studies further corroborated these findings, demonstrating that at low-Re, a single microbe swimming perpendicular to isopycnals has minimal impact on mixing [55]. However, numerical and laboratory experiments have demonstrated that the collective vertical migration of small organisms–like zooplankton swimming at intermediate Reynolds number $Re \sim O(1)$ [56, 57]–can drive a significant enhancement of the transport and mixing across fluid-fluid interfaces [58, 59]. Recently, it has been theoretically predicted that *Active Carpets*, formed by large numbers of organisms swimming at low Reynolds numbers, can drive long-range hydrodynamic fluctuations that enhance transport in fluid environments. This prompts further investigation into the behavior of these hydrodynamic fluctuations within layered environments.

This work focuses on *Active Carpets* living within a confined layer, bounded above by a free surface (air-water interface) and below by a fluid-fluid interface characterized by a viscosity interface that separates two fluid layers of viscosities μ_1 and μ_2. Within this environment, an *Active Carpet* experiences two confining mechanisms: geometrical confinement, characterized by the thickness of the upper layer H (the floating film), and viscous confinement, characterized by the viscosity jump or ratio $\lambda = \mu_2/\mu_1$. We can posit two scenarios for λ. In a first scenario, $\lambda < 1$, the *Active Carpet* lives in a fluid that it is more viscous that its underlying layer. Whereas in the second scenario, $\lambda > 1$, the *Active Carpet* lives in a less viscous layer than the subject layer. In this case, λ tells us how soft ($\lambda \to 1$) or rigid ($\lambda \to \infty$) the fluid-fluid viscous interface is.

The results of this thesis work contrast significantly from previous studies on *Active Carpets*. In the case of [45], the authors investigated *Active Carpets* living near a no-slip surface, the fluctuations decay monotonically as $\langle v_i^2 \rangle \propto z_0^{-4}$ for parallel dipoles. Similarly, [41] found that fluctuations were long-ranged, with $\langle v_i^2 \rangle \propto z_0^{-2}$ in the case of a free surface. In the case investigated here, the hydrodynamic fluctuations decay in a more manner due to the confinement and the influence of the viscous fluid-fluid interface. Although all the variances maintain their anisotropic behavior, we found a non-monotonic trend, with a striking change in the amplitude of the variance components and the dominance of directional effects. At some distance $z_\star$ from the *Active Carpet*, the vertical fluctuations decay much more rapidly with z_0 than the horizontal fluctuations.

This thesis is organized as follows: First, goals and research questions are stated. Continuing, in Chapter 2 we review the essential fluid dynamics theory at low Reynolds number to model microswimmer fluid disturbances in the medium, this being free or near boundaries. Then, in Chapter 3 we review the microscopic particle dynamics that microswimmers follow in a fundamental model of active matter. Next, Chapter 4 presents the theoretical and numerical aspects of the theory of active carpets developed to date in detail. Finally, in Chapter 5 we start by presenting the hydrodynamic model for point forces and dipole forces in a floating film, and then in Sec.5.4 we present the main findings of this thesis work.

Goals and Research Questions

The main goal of this thesis is to characterize the effects produced by an Active Carpet (AC) near a fluid-fluid interface, constrained to hydrodynamic confinement by a free-surface interface using tools from low Reynolds number fluid dynamics and statistical mechanics. The questions guiding our research are the following:

1. How is the geometry of the induced flow fluctuations due to a confined active carpet?
2. What is the role of fluid-fluid interface and the size of confinement in transport and fluctuations induced by a confined active carpet in the surrounding fluid?
3. Can a confined active carpet induce hydrodynamic fluctuations that in turn generate coherent flows that may lead to fluid mixing?

To answer these questions, we will employ the active carpets framework developed so far, which combines an analytical approach and a series of numerical simulations. Initially, we will implement the flow field exerted by a single microswimmer moving between both interfaces. Subsequently, we will identify the geometry of the AC's flow fluctuations. An understanding of this will set a basis for describing the hydrodynamics and microscopic dynamics of passive tracer particles above the AC.

Afterwards, we will explore the explicit dependency of the flow fluctuations on the characteristic parameters of the problem to unveil the role of confinement and the interface in shaping the fluid flow. By characterizing their role, we aim to identify whether the effects of the AC can be enhanced or diminished on a series of different physical configurations. Following this, we will focus on exploring quantitatively the mixing capabilities of the AC in favorable conditions, delving deeper into the fundamental length scales involved in the agitation of the fluid and the emergence of coherent structures.

This comprehensive approach will allow us to further understand the relationship between fluid interfaces and Active Carpets from hydrodynamics and out-of-equilibrium statistical mechanics, contributing to the modeling of collective dynamics and giving perspective on the biogenic role of microorganisms in layered environments.

Chapter 2

Microhydrodynamics

Fluid dynamics at the microscale is well studied and has been theoretically robust for decades. To understand the hydrodynamics of micro-swimmers we must start by understanding how their time scales are characterized and how the physical motion is intertwined with the response of the medium. In this chapter I start by introducing the Reynolds number to understand fluid particle's motion at the microscale. Then, I present the mathematical model that describes the perturbations of point forces in fluid media at low Reynolds numbers. After this, I connect the previous concepts with the reality of the motion of micro-swimmers and finish with the modeling of their perturbations in fluids when they are close to surfaces.

2.1 Low Reynolds number hydrodynamics

To describe the dynamics of an incompressible, viscous fluid of viscosity μ and density ρ due to the perturbations produced by an organism of length L and velocity U we must take into account two time scales: an advective time scale $t_A = L/U$, at which the surrounding fluid moves along the swimmer, and a diffusive time scale $t_D = \rho L^2/\mu$, at which, due to viscosity effects, perturbations are dissipated [60]. The ratio t_D/t_A defines a dimensionless quantity known as Reynolds number [61, 62]

$$\mathrm{Re} = \frac{\rho U L}{\mu}. \tag{2.1.1}$$

This quantity is usually interpreted as a measure of the relative importance of the inertial forces compared to the viscous forces produced by the swimmer in the fluid [63, 64]. For instance, if we consider the fluid as water, such that $\mu/\rho \sim 10^{-6} m^2/s$ and a bacterium such as an *Escherichia coli*, whose characteristic velocity and length are $U \sim 10^{-6}\, m/s$ and $L \sim 10^{-6} m$, respectively, then $\mathrm{Re} \sim 10^{-4} \ll 1$. Since other microorganisms, such as spermatozoa or algae have velocities and lengths of similar order of magnitude, these are usually said to swim at low Reynolds number [64].

The complex dynamics of a Newtonian fluid are described by the Navier-Stokes equations. On the low Reynolds number regime, where the effects of inertia by advection of the fluid are neglected, these are reduced to their linearized, simpler version, the Stokes equations [61].

2.2 The Stokes equations

The governing equations of motion of an incompressible, stationary fluid at a low Reynolds number are the Stokes equations

$$\nabla p(\boldsymbol{x}) = \mu \nabla^2 \boldsymbol{u}(\boldsymbol{x}) + \boldsymbol{F}(\boldsymbol{x}) \tag{2.2.1}$$

$$\nabla \cdot \boldsymbol{u}(\boldsymbol{x}) = 0 \tag{2.2.2}$$

where $\boldsymbol{u}(\boldsymbol{x})$ is the velocity field of the fluid at location $\boldsymbol{x}$, $p(\boldsymbol{x})$ is the pressure, μ is the dynamic viscosity and $\boldsymbol{F}(\boldsymbol{x}) = f_j \hat{\boldsymbol{e}}_j$ is any external force acting on the fluid. The index $j \in \{x, y, z\}$ denotes Cartesian directions, with $\hat{\boldsymbol{e}}_j$ as unit vectors.

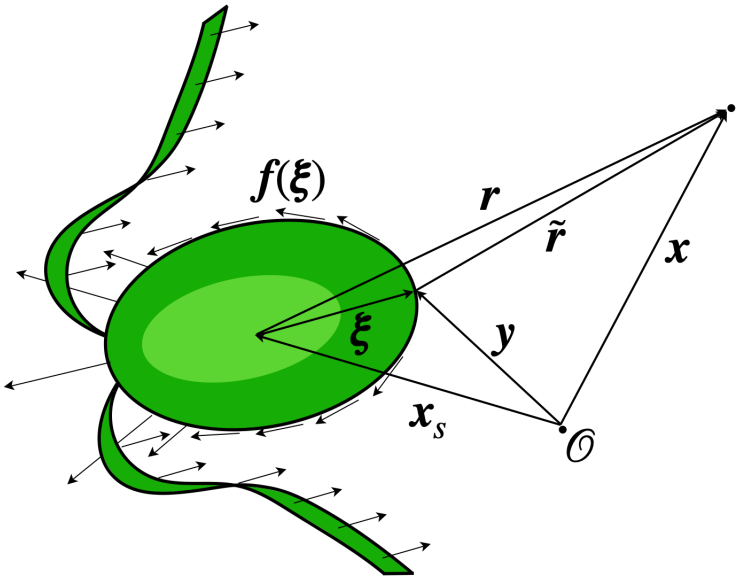

Figure 2.1: Scheme of microswimmer system of reference.

Consider the external force to be a point-force $\boldsymbol{F}(\boldsymbol{x},\boldsymbol{y}) = \delta^{(3)}(\boldsymbol{x}-\boldsymbol{y})\boldsymbol{f}^S$ acting at the fluid at position $\boldsymbol{y}$, where $\delta^{(3)}(\boldsymbol{x})$ is the Dirac delta function, and $\boldsymbol{f}^S$ is the force strength. We define $\tilde{\boldsymbol{r}} = \boldsymbol{x}-\boldsymbol{y}$ as the relative position of the force to the fluid. The three-dimensional, fundamental singular solution of the Stokes equations for the fluid velocity field $\boldsymbol{u}^S(\boldsymbol{x})$ due to the point-force $\boldsymbol{F}(\tilde{\boldsymbol{r}})$ is

$$u_i^S(\tilde{\boldsymbol{r}},\boldsymbol{f}^S) = f_j^S \mathcal{G}_{ij}(\tilde{\boldsymbol{r}}) \tag{2.2.3}$$

$$\mathcal{G}_{ij}(\boldsymbol{r}) = \frac{1}{8\pi\mu}\left(\frac{\delta_{ij}}{r} + \frac{r_i r_j}{r^3}\right) \tag{2.2.4}$$

where $r = |\boldsymbol{r}|$, δ_{ij} is the Kronecker delta, and $\mathcal{G}_{ij}(\boldsymbol{r})$ is the Green's function called the Oseen tensor. The resulting velocity field is well-known as the Stokeslet [65, 66, 67]. Note that we use the Einstein summation convention. The boundary condition on the velocity field is that far away from where the force is acting, the disturbance flow generated by the microswimmer should decay, such that

$$\lim_{|\boldsymbol{x}|\to\infty} u_i^S(\tilde{\boldsymbol{r}},\boldsymbol{f}^S) = 0 \tag{2.2.5}$$

The corresponding pressure field $p(\boldsymbol{x})$ due to the point-force $\boldsymbol{F}(\tilde{\boldsymbol{r}})$ is written similarly as

$$p(\tilde{\boldsymbol{r}},\boldsymbol{f}^S) = f_j^S \mathcal{P}_j(\tilde{\boldsymbol{r}}) \tag{2.2.6}$$

$$\mathcal{P}_j(\boldsymbol{r}) = \frac{r_j}{4\pi r^3} \tag{2.2.7}$$

The viscous stress tensor is defined as

$$\sigma_{ij} = -p\delta_{ij} + \mu\left(\frac{\partial u_i}{\partial x_j} + \frac{\partial u_j}{\partial x_i}\right) = -p\delta_{ij} + 2\mu \mathrm{E}_{ij} \tag{2.2.8}$$

where E_{ij} is the strain-rate (or rate of deformation, shear stress) tensor

$$\mathrm{E}_{ij} = \frac{1}{2}\left(\frac{\partial u_i}{\partial x_j} + \frac{\partial u_j}{\partial x_i}\right) \tag{2.2.9}$$

The stress tensor in terms of the Oseen tensor is defined as

$$\sigma_{ik}(\tilde{\boldsymbol{r}},\boldsymbol{f}^S) = f_j^S \mathrm{T}_{ijk}(\tilde{\boldsymbol{r}}) \tag{2.2.10}$$

$$\mathrm{T}_{ijk}(\boldsymbol{r}) = -\delta_{ik}\mathcal{P}_j(\boldsymbol{r}) + \frac{\partial \mathcal{G}_{ij}(\boldsymbol{r})}{\partial r_k} + \frac{\partial \mathcal{G}_{kj}(\boldsymbol{r})}{\partial r_i} \tag{2.2.11}$$

The stress field $\sigma_{ik}(\boldsymbol{x})$ due to a point-force $\boldsymbol{F}(\tilde{\boldsymbol{r}})$ is obtained from replacing Eq.(2.2.4) and Eq.(2.2.8) in Eq.(2.2.11), such that

$$\mathrm{T}_{ijk}(\boldsymbol{r}) = -\frac{3r_i r_j r_k}{4\pi r^5} \tag{2.2.12}$$

2.3 Multipole Expansion

Consider a finite microswimmer with surface $S(\boldsymbol{\xi})$ located at position $\boldsymbol{y} = \boldsymbol{x}_s + \boldsymbol{\xi}$. We define the relative position of a point in the fluid according to the swimmer's center as $\boldsymbol{r} = \boldsymbol{x} - \boldsymbol{x_s}$. The geometry is shown in Fig.2.1. As it swims, it exerts forces on the fluid on each point of its surface so there is a distribution $\boldsymbol{f}(\boldsymbol{\xi})$ of forces acting on the fluid. Using the singular solution we can write the full flow field as the sum of the Oseen tensor over the swimmer's surface

$$u_i^{sw}(\boldsymbol{r}) = \int_{S(\boldsymbol{\xi})} \mathcal{G}_{ij}(\boldsymbol{r} - \boldsymbol{\xi}) f_j(\boldsymbol{\xi}) dS \tag{2.3.1}$$

Performing a multipole expansion around $\boldsymbol{r}$ for small values of $\boldsymbol{\xi}$ so we neglect higher-order terms we have

$$u_i^{sw}(\boldsymbol{r}) = \int_{S(\boldsymbol{\xi})} \left(\mathcal{G}_{ij}(\boldsymbol{r}) - \frac{\partial \mathcal{G}_{ij}(\boldsymbol{r})}{\partial r_k} \xi_k + \frac{1}{2} \frac{\partial \mathcal{G}_{ij}(\boldsymbol{r})}{\partial r_k \partial r_l} \xi_k \xi_l + \cdots \right) f_j(\boldsymbol{\xi}) dS \tag{2.3.2}$$

Since the Oseen tensor and its derivative do not depend on $\boldsymbol{\xi}$,

$$u_i^{sw}(\boldsymbol{r}) = \mathcal{G}_{ij}(\boldsymbol{r}) \int_{S(\boldsymbol{\xi})} f_j(\boldsymbol{\xi}) dS - \frac{\partial \mathcal{G}_{ij}(\boldsymbol{r})}{\partial r_k} \int_{S(\boldsymbol{\xi})} f_j(\boldsymbol{\xi}) \xi_k dS + \frac{1}{2} \frac{\partial \mathcal{G}_{ij}(\boldsymbol{r})}{\partial r_k \partial r_l} \int_{S(\boldsymbol{\xi})} f_j(\boldsymbol{\xi}) \xi_k \xi_l dS + \ldots \tag{2.3.3}$$

These integrals correspond to the multipole moment tensors of the expansion so that we rewrite them as

$$u_i^{sw}(\boldsymbol{r}) = \mathcal{G}_{ij}(\boldsymbol{r}) F_j - \frac{\partial \mathcal{G}_{ij}(\boldsymbol{r})}{\partial r_k} D_{jk} + \frac{1}{2} \frac{\partial \mathcal{G}_{ij}(\boldsymbol{r})}{\partial r_k \partial r_l} Q_{jkl} + \ldots \tag{2.3.4}$$

Here note that F_j is the net force exerted over the swimmer's surface, but swimmers are known to be neutrally buoyant so there are no exerted forces over them. Then, assuming that the effects of inertia are negligible, $F_j = 0$. From this, we get that the leading order term in the expansion is the dipolar contribution, which captures perfectly the fluid perturbation made by a swimming microorganism in the far-field [68, 69, 70]

$$u_i^{sw}(\boldsymbol{r}) = -\frac{\partial \mathcal{G}_{ij}(\boldsymbol{r})}{\partial r_k} D_{jk} \tag{2.3.5}$$

where D_{jk} is the dipole moment tensor and the whole term scales as r^{-2}. For an axisymmetric swimmer, the symmetric part of D_{jk}, known as the stresslet tensor, can be written as [71, 72, 73, 60]

$$D_{jk} = \sigma_0 p_j p_k \tag{2.3.6}$$

where $\sigma_0 \approx -F_0 \ell$ is the stresslet magnitude and p_j the force dipole orientation. Here F_0 is the magnitude of the opposite forces involved in its motion and ℓ is a characteristic length on the order of the cell dimensions. The sign of σ_0 depends on the position of the thrust and drag forces. In Fig.2.2 (top) a scheme is shown on the swimming mechanism by a "pusher" ($\sigma_0 < 0$) and a "puller" ($\sigma_0 > 0$) microswimmer. The first one, a pusher microswimmer, generates a net thrust $-F_0\boldsymbol{p}$ due to the rotation of the flagellar bundle, which must balance the viscous drag force $F_0\boldsymbol{p}$ exerted by the cell body as it translates through the fluid, resulting in an extensile dipole force. On the other hand, a puller microswimmer, by beating its flagella, generates a net thrust $-F_0\boldsymbol{p}$ towards the cell body, generating an opposite drag force $F_0\boldsymbol{p}$ needed to move the cell body, resulting in a contractile dipole force [73].

In [70], from direct measurements of the flow field around freely swimming *Escherichia coli* bacteria, they obtained that $\ell = 1.9\,\mu m$ and $F_0 \approx 0.42\,pN$, such that $\sigma_0 \approx -0.8\,pN\,\mu m$. Similarly, in [69, 74] they measured for the single-celled, biflagellate swimming alga *Chlamydomonas reinhardtii*, $\ell = 5\,\mu m$ and $-F_0 \approx 9.4\,pN$ [75], such that $\sigma_0 \approx 47\,pN\,\mu m$. In comparison, a *C. reinhardtii* alga is approximately 58% stronger or more capable of exerting power than a *E. coli* bacterium.

Using Eq.(2.3.6) and the definition of stresslet magnitude, σ_0, we can rewrite the expression for the far-field dipole velocity field from Eq.(2.3.5) as

$$u_i^D(\boldsymbol{r}) = F_0 \ell p_k \frac{\partial \mathcal{G}_{ij}(\boldsymbol{r})}{\partial r_k} p_j \tag{2.3.7}$$

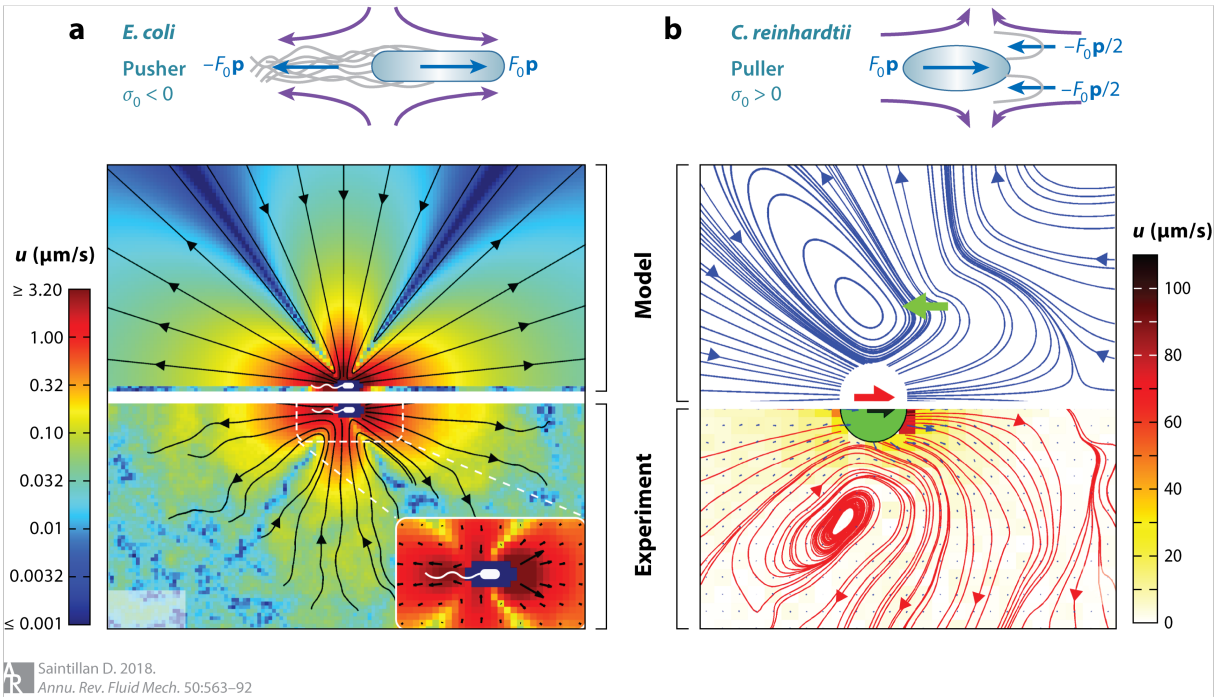

Figure 2.2: Disturbance flows induced by swimming microorganisms. (a) Drescher et al.'s (2011) particle image velocimetry measurements around individual *Escherichia coli* cells (bottom) compared to a theoretical stresslet flow (top). (b) Drescher et al.'s (2010) time-averaged particle image velocimetry measurements using *Chlamydomonas reinhardtii* show a complex flow in the near field that is well approximated by three off-centered point forces. Reproduced from [73].

Note that the Stokelet velocity field definition from Eq.(2.2.3) appears from inserting p_j in the derivative, then we can also rewrite it in terms of the Stokeslet, now in vector notation, as

$$\frac{\boldsymbol{u}^D(\boldsymbol{r})}{8\pi\mu} = \kappa(\boldsymbol{p}\cdot\nabla_s)(\mathcal{G}\cdot\boldsymbol{p}) \tag{2.3.8}$$

where $\kappa = F_0\ell/8\pi\mu$ which now is the stresslet magnitude, and has units of $[\mu m^3/s]$. This definition is more commonly used and the sign determines if the microswimmer is a pusher ($\kappa > 0$) or a puller ($\kappa < 0$) inversely to the convention of σ_0. The dimensions of κ are $[\kappa] = [\text{velocity} \times \text{length}^2]$, and it scales as $\kappa \sim a^2 v_s$, where $a = \ell$ is the characteristic size of the microswimmer ($\approx 1 - 10\,\mu m$) and v_s its the swimming speed ($\approx 10 - 100\,\mu m/s$), ranging from 8 to 75 $\mu m^3/s$ [76, 4, 69, 70, 77].

2.4 Microswimmers swimming near boundaries

Motile microorganisms are commonly known to be attracted by surfaces. Their presence can impact dramatically their ability to generate forces for locomotion. We can take advantage of the properties of the Stokes equations and through its singular solutions solve the hydrodynamics of microswimmers near boundaries by using the method of images to fulfill the induced hydrodynamic boundary conditions. In Sec.2.4.1 I review the boundary conditions that the velocity field and stress must satisfy when there is a fluid a solid wall, and a fluid-fluid interface. In Sec.2.4.2, I present the application of the method of images to solve the hydrodynamics of a microswimmer swimming near a specified boundary.

2.4.1 Boundary conditions at solid walls and fluid interfaces

In general, a fluid near a rigid, solid boundary, must not slip at the boundary so that the fluid moves with the prescribed velocity of the boundary (which is often stationary). This can be broken down into

conditions on the normal and tangential components, as

$$\boldsymbol{u}\cdot\boldsymbol{n} = \mathbf{v}\cdot\boldsymbol{n} \qquad \text{(kinematic condition)} \tag{2.4.1}$$

$$\boldsymbol{u} - (\boldsymbol{u}\cdot\boldsymbol{n})\boldsymbol{n} = \mathbf{v} - (\mathbf{v}\cdot\boldsymbol{n})\boldsymbol{n} \qquad \text{(dynamic condition)} \tag{2.4.2}$$

where $\mathbf{v}$ is the velocity of the boundary, and $\boldsymbol{n}$ is a unit vector normal to the boundary. Here, Eq.(2.4.1), is sometimes referred to as a no-penetration (impermeability) condition, while Eq.(2.4.2), is the no-slip condition. Normally, it's assumed that the boundary is stationary, so $\mathbf{v} = \mathbf{0}$ reduces the no-slip condition to its most common form

$$\boldsymbol{u} = \mathbf{0} \qquad \text{at the solid wall} \tag{2.4.3}$$

As an example, this condition applies at the bed of a glacier that is frozen to its bed, or a rough, non-porous surface where nearby microswimmers move disturbing the surrounding fluid. Furthermore, as the fluid velocity vanishes at the solid surface, there are significant velocity gradients towards the boundary (which form a boundary layer), resulting in non-zero shear stress acting tangential to the surface.

Another important scenario is the one of a fluid-fluid interface. Assuming the interface is non-deformable neither in space nor in time, both fluid velocities must satisfy the kinematic condition, such that

$$\boldsymbol{u}^{(1)}\cdot\boldsymbol{n} = \boldsymbol{u}^{(2)}\cdot\boldsymbol{n} = 0 \qquad \text{at the interface} \tag{2.4.4}$$

Then the dynamic condition requires the continuity of the fluid velocity across the interface

$$\boldsymbol{u}^{(1)} = \boldsymbol{u}^{(2)} \qquad \text{at the interface} \tag{2.4.5}$$

Also, it requires a stress balance that comes from a force equilibrium condition on the interface, as it is assumed to be a surface of zero thickness, such that it can be entirely characterized by a surface or interfacial tension,γ, that is a function of the local thermodynamic state, such as temperature or pressure, but is independent of whether the interface is undergoing any macroscopic motion or deformation. Mathematically, the stress balance is expressed as the following condition

$$\Delta\boldsymbol{\sigma}\cdot\boldsymbol{n} + \nabla_s\gamma - \gamma\boldsymbol{n}(\nabla\cdot\boldsymbol{n}) = 0 \tag{2.4.6}$$

where $\Delta\boldsymbol{\sigma} = \boldsymbol{\sigma}^{(1)} - \boldsymbol{\sigma}^{(2)}$, $\boldsymbol{\sigma}^{(i)} = -p^{(i)} + 2\mu^{(i)}\mathbf{E}^{(i)}$ and $\nabla_s \equiv \nabla - \boldsymbol{n}(\boldsymbol{n}\cdot\nabla)$. It's useful to express this condition in its tangential and normal directions

$$\boldsymbol{n}\cdot\Delta\boldsymbol{\sigma}\cdot\boldsymbol{n} - \gamma(\nabla\cdot\boldsymbol{n}) = 0 \qquad \text{(normal-stress balance)} \tag{2.4.7}$$

$$\boldsymbol{n}\cdot\Delta\boldsymbol{\sigma}\cdot\boldsymbol{t}_{(i)} + \nabla_s\gamma\cdot\boldsymbol{t}_{(i)} = 0 \qquad \text{(tangential or shear-stress balance)} \tag{2.4.8}$$

where $\boldsymbol{t}_i$ are two orthogonal unit tangent vectors that are normal to $\boldsymbol{n}$. The first one is interpreted as that in crossing an interface, the normal component of the total stress is discontinuous, as undergoes a jump equal to $\gamma(\nabla\cdot\boldsymbol{n})$, where $\nabla\cdot\boldsymbol{n}$ is the curvature of the interface. Note that a planar, non-deforming interface has zero curvature, so the normal stress becomes continuous across the interface.

On the other hand, the second condition implies that the shear stress is discontinuous across the interface whenever $\nabla_s\gamma$ is non-zero. Nonetheless, in the absence of significant surface tension gradients, $\nabla_s\gamma = 0$, it requires the continuity of shear stress

$$\left[(\mathbf{E}^{(1)} - \lambda\mathbf{E}^{(2)})\cdot\boldsymbol{n}\right]\cdot\boldsymbol{t}_{(i)} = 0 \tag{2.4.9}$$

where $\lambda = \mu_2/\mu_1$. In particular, if one of the fluids is considerably more viscous than the other, e.g., a gas-liquid interface, $\lambda \approx 0$, then the condition reduces to

$$\left[(\mathbf{E}^{(1)})\cdot\boldsymbol{n}\right]\cdot\boldsymbol{t}_{(i)} = 0 \tag{2.4.10}$$

in the fluid with a larger viscosity. This condition is often known as the "zero-shear-stress" condition (though it is strictly the velocity gradient that is approximately zero rather than the stress) and applies to free surfaces.

2.4.2 Microswimmer's velocity field image system

Consider an infinite, planar boundary, extended over the plane $z = 0$, as shown in Fig.2.3. A microswimmer is located at position $\boldsymbol{x}_s$, with surface $S(\boldsymbol{\xi})$, located at $\boldsymbol{y} = \boldsymbol{x}_s + \boldsymbol{\xi}$, which has a force distribution $\boldsymbol{f}(\boldsymbol{\xi})$ exerted by the swimmer's body. The relative position of a point $\boldsymbol{x}$ in the fluid according to the swimmer's center and swimmer's surface are $\boldsymbol{r} = \boldsymbol{x} - \boldsymbol{x}_s$ and $\tilde{\boldsymbol{r}} = \boldsymbol{x} - \boldsymbol{y}$, respectively. According to the method of images, we introduce an image swimmer, located at position $\boldsymbol{x}_s^*$, with surface $S(\boldsymbol{\xi}^*)$ located at $\boldsymbol{y}^* = \boldsymbol{x}_s^* + \boldsymbol{\xi}^*$ and a force distribution $\boldsymbol{f}(\boldsymbol{\xi}^*)$. Also, equivalent relative positions according to the image swimmer's center and the image swimmer's surface, $\boldsymbol{r}^* = \boldsymbol{x} - \boldsymbol{x}_s^*$ and $\tilde{\boldsymbol{r}}^* = \boldsymbol{x} - \boldsymbol{y}^*$, respectively.

As in Sec.2.2, we consider a point force $\boldsymbol{F}(\boldsymbol{x}, \boldsymbol{y}) = \delta^{(3)}(\boldsymbol{x} - \boldsymbol{y})\boldsymbol{f}^S$ acting at point $\boldsymbol{y}$ on the surface of the swimmer, with force strength $\boldsymbol{f}^S$. Following the scheme on Fig.2.3, the Stokes equations for fluid 1 are

$$\nabla p^{(1)} = \mu_1 \nabla^2 \boldsymbol{u}^{(1)} + \delta^{(3)} \boldsymbol{f}^S(\boldsymbol{x} - \boldsymbol{y}), \tag{2.4.11}$$

$$\nabla \cdot \boldsymbol{u}^{(1)} = 0, \tag{2.4.12}$$

while for fluid 2 we have

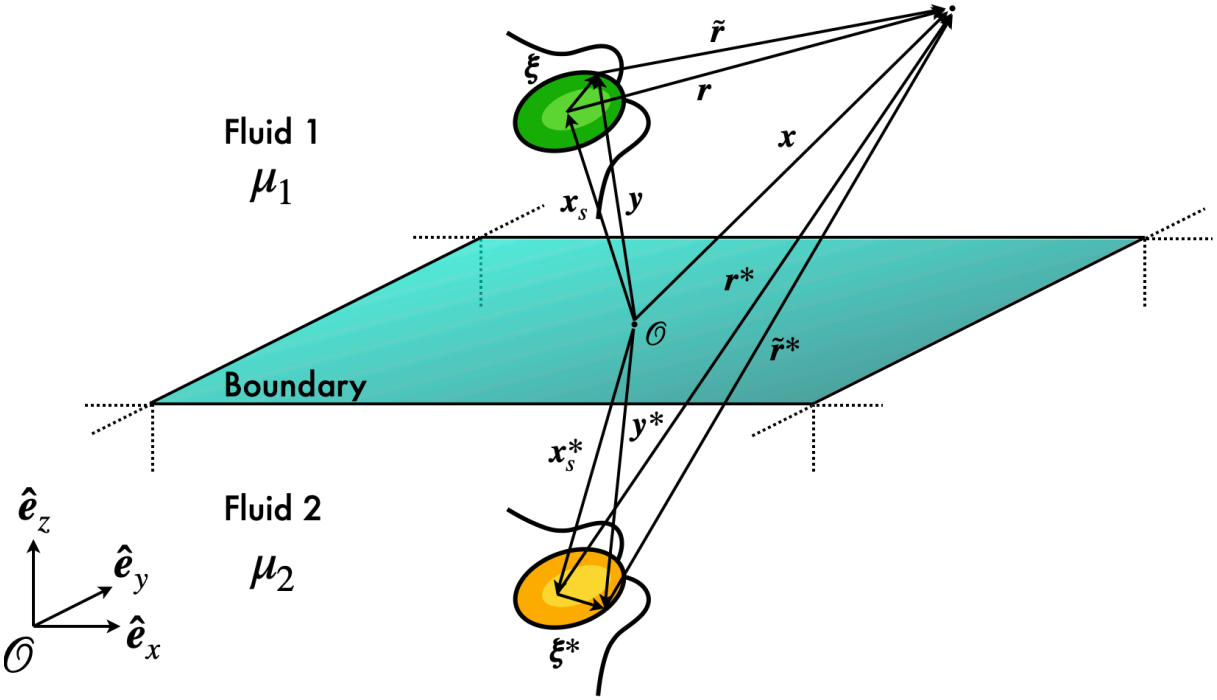

Figure 2.3: Scheme of the image system for a single microswimmer moving near a fluid-fluid interface.

$$\nabla p^{(2)} = \mu_2 \nabla^2 \boldsymbol{u}^{(2)} + \boldsymbol{F}^{\text{im}}(\boldsymbol{x}, \boldsymbol{y}^*), \tag{2.4.13}$$

$$\nabla \cdot \boldsymbol{u}^{(2)} = 0. \tag{2.4.14}$$

where $\boldsymbol{F}^{\text{im}}(\boldsymbol{x}, \boldsymbol{y}^*)$ is any force required from the image system that is needed to satisfy the boundary conditions on the velocity field $\boldsymbol{u}^{(1)}(\boldsymbol{x})$. Note that as a general boundary condition, as in bulk, both fluid velocities must decay in the far field,

$$\lim_{|\boldsymbol{x}| \to \infty} \boldsymbol{u}^{(i)}(\boldsymbol{x}) = \boldsymbol{0} \qquad \text{with } i = 1, 2. \tag{2.4.15}$$

The solution of Eq.(2.4.11) is the Stokeslet, while the solution of Eq.(2.4.13) will depend strongly on the specification of the boundary, such that the effective velocity field will be

$$\boldsymbol{u}^{(1)}(\boldsymbol{x}, \boldsymbol{y}, \boldsymbol{y}^*, \boldsymbol{f}^S) = f_j^S \mathcal{G}_{ij}(\boldsymbol{x}, \boldsymbol{y}) + f_j^S \mathcal{Y}_{ij}(\boldsymbol{x}, \boldsymbol{y}^*) = u_i^S(\boldsymbol{x}, \boldsymbol{y}, \boldsymbol{f}^S) + u_i^{S*}(\boldsymbol{x}, \boldsymbol{y}^*, \boldsymbol{f}^S) \tag{2.4.16}$$

where $\mathcal{Y}_{ij}(\boldsymbol{x},\boldsymbol{y}^*)$ is the appropriate Green's function, i.e., the image system, that is needed to fulfill the boundary conditions, and $\boldsymbol{u}^{S*}(\boldsymbol{x})$ its velocity field. In the following, I show the boundary conditions and the respective image system required for a free surface boundary (e.g. an air-liquid interface), a solid boundary, and a liquid-liquid interface between two fluids with different viscosities:

1. Considering the boundary as a non-deformable, stationary free surface (e.g., an air-liquid interface), the boundary conditions for fluid 1 at the interface are the kinematic and zero-shear-stress conditions, Eq.(2.4.4) and Eq.(2.4.10), respectively

$$\boldsymbol{u}^{(1)}\cdot\boldsymbol{n}=0 \tag{2.4.17}$$

$$\hat{\boldsymbol{e}}_z\cdot\mathbf{E}^{(1)}\cdot\hat{\boldsymbol{e}}_x=\hat{\boldsymbol{e}}_z\cdot\mathbf{E}^{(1)}\cdot\hat{\boldsymbol{e}}_y=0 \tag{2.4.18}$$

The velocity field of the image system for fluid 1 near an air-liquid boundary is

$$u_i^{S*}(\boldsymbol{x},\boldsymbol{y}^*,\boldsymbol{f}^S)=f_j^S\mathcal{F}_{ij}(\tilde{\boldsymbol{r}}) \tag{2.4.19}$$

$$\mathcal{F}_{ij}(\boldsymbol{r})=\mathsf{M}_{jk}\mathcal{G}_{ik}=\frac{1}{8\pi\mu_1}\mathsf{M}_{jk}\left(\frac{\delta_{ik}}{r}+\frac{r_ir_k}{r^3}\right) \tag{2.4.20}$$

where $\mathsf{M}_{jk}=(\delta_{j\alpha}\delta_{\alpha k}-\delta_{j3}\delta_{3k})=\mathrm{diag}(1,1,-1)$ is a mirror matrix, with $\alpha=1,2$.

2. Considering the boundary as a stationary, solid surface, the boundary condition at the surface is the no-slip condition, Eq.(2.4.2),for fluid 1

$$\boldsymbol{u}^{(1)}=\boldsymbol{0} \tag{2.4.21}$$

The velocity field of the image system for fluid 1 near a solid surface is

$$u_i^{S*}(\boldsymbol{x},\boldsymbol{y}^*,\boldsymbol{f}^S)=f_j^S\mathcal{B}_{ij}(\tilde{\boldsymbol{r}}) \tag{2.4.22}$$

$$\mathcal{B}_{ij}(\boldsymbol{r})=\frac{1}{8\pi\mu_1}\left[-\left(\frac{\delta_{ij}}{r}+\frac{r_ir_j}{r^3}\right)+2x_{s,3}\mathsf{M}_{jk}\frac{\partial}{\partial r_k}\left(\frac{x_{s,3}r_i}{r^3}-\left(\frac{\delta_{i3}}{r}+\frac{r_ir_3}{r^3}\right)\right)\right] \tag{2.4.23}$$

3. Considering the boundary as a non-deformable, stationary liquid-liquid interface, the boundary conditions are the kinematic condition,Eq.(2.4.4), and the continuity of the fluid velocity and shear stress at the interface, Eq.(2.4.5) and Eq.(2.4.9), respectively

$$\boldsymbol{u}^{(1)}\cdot\boldsymbol{n}=\boldsymbol{u}^{(2)}\cdot\boldsymbol{n}=0 \tag{2.4.24}$$

$$\boldsymbol{u}^{(1)}=\boldsymbol{u}^{(2)} \tag{2.4.25}$$

$$\hat{\boldsymbol{e}}_z\cdot\mathbf{E}^{(1)}\cdot\hat{\boldsymbol{e}}_\alpha=\hat{\boldsymbol{e}}_z\cdot\lambda\mathbf{E}^{(2)}\cdot\hat{\boldsymbol{e}}_\alpha\qquad\text{with}\,\alpha=y,z \tag{2.4.26}$$

where $\lambda=\mu_2/\mu_1$. The velocity field of the image system for fluid 1 near a liquid-liquid interface is

$$u_i^{S*}(\boldsymbol{x},\boldsymbol{y}^*,\boldsymbol{f}^S)=f_j^S\mathcal{A}_{ij}^{(1)}(\tilde{\boldsymbol{r}}) \tag{2.4.27}$$

$$\mathcal{A}_{ij}^{(1)}(\boldsymbol{r})=\frac{1}{8\pi\mu_1}\left[-\mathsf{M}_{jk}^{\lambda}\left(\frac{\delta_{ik}}{r}+\frac{r_ir_k}{r^3}\right)+2\Lambda_1x_{s,3}\mathsf{M}_{jk}\frac{\partial}{\partial r_k}\left(\frac{x_{s,3}r_i}{r^3}-\left(\frac{\delta_{i3}}{r}+\frac{r_ir_3}{r^3}\right)\right)\right] \tag{2.4.28}$$

where $\mathsf{M}_{jk}^{\lambda}=\Lambda_2\delta_{\alpha k}\delta_{\alpha k}+\delta_{j3}\delta_{3k}=\mathrm{diag}(\Lambda_2,\Lambda_2,1)$, with $\Lambda_2=(\lambda-1)/(\lambda+1)$, $\Lambda_1=\lambda/(\lambda+1)$, and $\alpha=1,2$. The resulting velocity field of fluid 2 is directly

$$u_i^{(2)}(\boldsymbol{x},\boldsymbol{y}^*,\boldsymbol{f}^S)=f_j^S\mathcal{A}_{ij}^{(2)}(\tilde{\boldsymbol{r}}) \tag{2.4.29}$$

$$\mathcal{A}_{ij}^{(2)}(\boldsymbol{r})=\frac{1}{8\pi\mu_2}\frac{2}{1+\lambda}\left[\delta_{j\alpha}\left(\frac{\delta_{i\alpha}}{r}+\frac{r_ir_\alpha}{r^3}\right)+x_{s,3}\frac{\partial}{\partial x_j}\left(-\frac{x_{s,3}r_i}{r^3}-\left(\frac{\delta_{i3}}{r}+\frac{r_ir_3}{r^3}\right)\right)\right] \tag{2.4.30}$$

As in Sec.2.3, we model the microswimmer's velocity field by considering a distribution of forces, $\boldsymbol{f}(\boldsymbol{\xi})$, over its body's surface, $S(\boldsymbol{\xi})$, and the same for the image system, such that now the effective velocity field from Eq.(2.4.16) is integrated as

$$u_i^{sw}(\boldsymbol{r},\boldsymbol{r}^*)=\int_{S(\boldsymbol{\xi})}\left(\mathcal{G}_{ij}(\boldsymbol{r}-\boldsymbol{\xi})+\mathcal{Y}_{ij}(\boldsymbol{r}^*-\boldsymbol{\xi}^*)\right)f_j(\boldsymbol{\xi})dS \tag{2.4.31}$$

After a multipole expansion for small $\boldsymbol{\xi}$ and $\boldsymbol{\xi}^*$, we obtain

$$u_i^{sw}(\boldsymbol{r},\boldsymbol{r}^*) = (\mathcal{G}_{ij}(\boldsymbol{r}) + \mathcal{Y}_{ij}(\boldsymbol{r}^*))F_j - \frac{\partial(\mathcal{G}_{ij}(\boldsymbol{r}) + \mathcal{Y}_{ij}(\boldsymbol{r}^*))}{\partial r_k} D_{jk} + \cdots \tag{2.4.32}$$

which, for neutrally buoyant microswimmers, the leading order term takes the form

$$u_i^{sw}(\boldsymbol{r},\boldsymbol{r}^*) = -\frac{\partial(\mathcal{G}_{ij}(\boldsymbol{r}) + \mathcal{Y}_{ij}(\boldsymbol{r}^*))}{\partial r_k} D_{jk} \tag{2.4.33}$$

According to the theory and experimental insights described in Sec.2.3, describing the velocity field of a microswimmer moving near a boundary requires the addition of an appropriate image system to take into account the effects of the boundary, which in this singularity description is straightforward for simple boundaries. In general, the far-field dipole velocity field can be written as

$$\frac{\boldsymbol{u}^D}{8\pi\mu} = \kappa(\boldsymbol{p}\cdot\nabla_s)\left[(\mathcal{G}_{ij} + \mathcal{Y}_{ij})\cdot\boldsymbol{p}\right] \tag{2.4.34}$$

Fig.2.4 shows the flow fields produced by microswimmers near a solid boundary (top row) and near a free surface (bottom row).

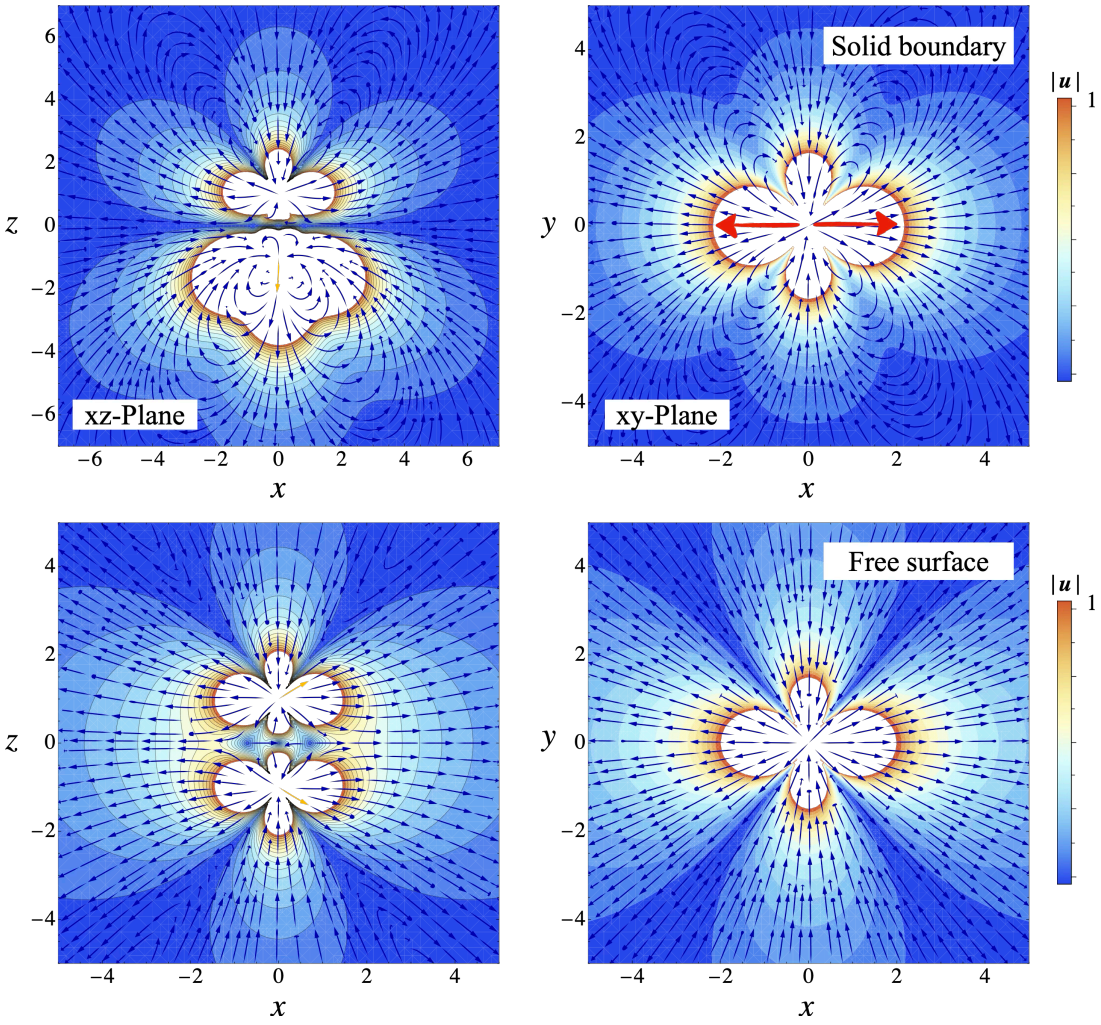

Figure 2.4: Flow fields produced by microswimmers (force dipoles) near interfaces.

In this chapter I presented the fundamental hydrodynamics for modeling the perturbation in the fluid medium produced by micro-swimmers. In the next chapter I investigate the dynamics of micro-swimmers as small particles moving in a medium and describe their transport properties.

Chapter 3

Dynamics and transport of microswimmers

An extensive experimental analysis and mathematical modeling of the single microswimmer dynamics have been performed intensively over at least the last two decades, leading, for instance, to the creation of bio-engineered, synthetic microswimmers that mimic the biological ones. As stated in Chap.2, microorganisms in the low Reynolds number world swim through their medium by non-reciprocal motion, disturbing the surrounding fluid in such a way that it allows one to model these disturbances in space accurately, but not in time. Yet, it is possible to understand and describe their motion dynamics robustly by studying the role of their intrinsic activity at the microscale. In this chapter, I first briefly introduce the concept of Brownian motion as a key to understanding transport in the microscale. Second, I present a model to describe the motion of a single microswimmer from a statistical mechanics point of view, focusing on its non-equilibrium and transport properties. Finally, I give a rationalization on why microorganisms swim as they do, based on the best-understood microorganism: the *Escherichia Coli* bacterium and its mechanism of motion, the run-and-tumble. Additionally, I give a quantitative overview of the transport capabilities of microorganisms such as E. coli and the microalgae *Chlamydomonas reindhartii*, and compare them with those of passive or non-motile micron-sized particles.

3.1 Brownian motion

In 1827, in one of its experiments, the botanist Robert Brown observed through a microscope the intriguing erratic, irregular motion of small pollen grain particles of the plant Clarkia pulchella immersed in water, leading him at first to think that they were alive [78]. Nonetheless, after testing this phenomenon thoroughly with other kinds of particles of inorganic matter, he concluded that the motion was not due to any living organism, but still of a purely physical nature. Later [79], this work, among others like the one from M. Gouy in 1888 [80], explored this phenomenon even in more detail. In 1905-06 [81, 82], the physicist Albert Einstein described Brownian motion theoretically, pointing out that Brownian motion was caused by the permanent, random thermal motion of the liquid molecules of the solution on the immersed particles. He was followed by M. Smoluchowski [83] in 1906 with a different approach to describe Brownian motion in terms of random walks and conditional probability [84]. Eintein's work allowed Jean Perrin to confirm the atomic nature of matter experimentally in 1909 [85]. Typical trajectories of colloidal particles undergoing Brownian motion are shown in Fig.3.1, directly from Perrin's experiments.

A simpler approach, which I present in the following, was given by P. Langevin in 1908 [86], who treated the random thermal agitation as the action of a stochastic force and wrote Newton's second law for an immersed particle of mass m. Denoting the position of the particle by $\boldsymbol{r}(t)$ in three dimensions, its dynamics are given by

$$\boldsymbol{v}(t) = \frac{d\boldsymbol{r}(t)}{dt}; \qquad m\frac{d^2\boldsymbol{r}(t)}{dt^2} = -\zeta\frac{d\boldsymbol{r}(t)}{dt} + \boldsymbol{f}_{\mathcal{B}}(t) \tag{3.1.1}$$

where $\zeta = 6\pi\mu R$ is the Stokes drag for a particle of radius R and fluid with viscosity μ, such that the first term on the RHS is the hydrodynamic drag force on the particle, $\boldsymbol{f}_{\mathcal{H}} = -\zeta\boldsymbol{v}(t)$. The second term

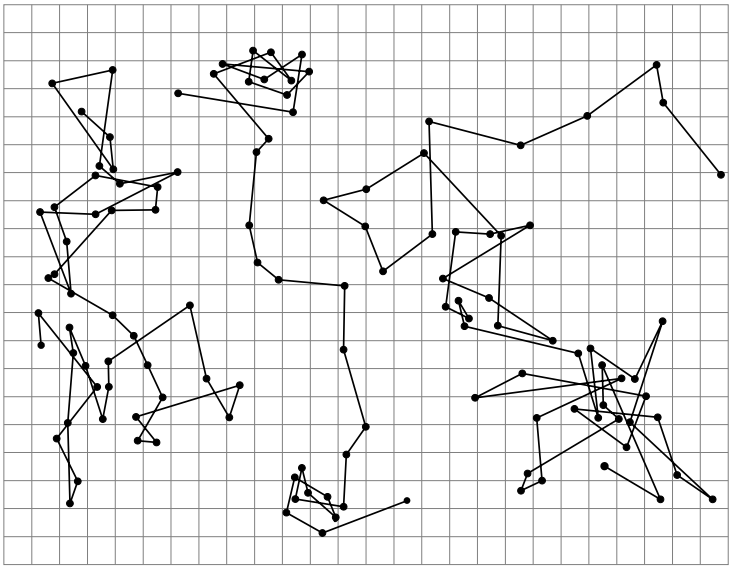

Figure 3.1: Three traced trajectories from colloidal particles of radius 0.53 μm with position measured every 30 seconds. The mesh size is 3.2 μm. By J. B. Perrin, SVG drawing by MiraiWarren - SVG drawing based on File:PerrinPlot2.gif, itself from J. B. Perrin, "Mouvement brownien et réalité moléculaire," Ann. de Chimie et de Physique (VIII) 18, 5-114 (1909).

on the RHS is the stochastic force which arises from the molecular collisions and is set to be Gaussian (white noise) distributed with independent components and delta-correlated in time [87], such that

$$\langle \boldsymbol{f}_{\mathcal{B}}(t) \rangle = 0 \tag{3.1.2}$$

$$\langle f_i^{\mathcal{B}}(t) f_j^{\mathcal{B}}(t') \rangle = 2k_B T \zeta \delta_{ij} \delta(t-t') = 2D\zeta^2 \delta_{ij} \delta(t-t') \qquad \text{with } i,j = x,y,z. \tag{3.1.3}$$

where the brackets denote ensemble averages over many realizations, k_B is the Boltzmann's constant ($k_B = 1.38 \times 10^{-23} J/K$) and T is the absolute temperature [85].

An expression for the mean square displacement MSD(t) of a (inertial) particle was introduced by Ornstein and Uhlenbeck in 1919 [88], computed by invoking equipartition theorem, such that

$$\text{MSD}(t) = \langle |\boldsymbol{r}(t) - \boldsymbol{r}(0)|^2 \rangle = 6Dt - 6\frac{k_B T}{m}\tau_m^2 \left(1 - e^{-t/\tau_m}\right) \tag{3.1.4}$$

where $\tau_m = m/\zeta$ is the momentum relaxation time, i.e., the time needed for the particle to adapt to inertial changes. For a micron-sized particle in water at room temperature, $\tau_m = \mathcal{O}(10^{-7} s)$. At short times $t \ll \tau_m$, the particle experiences a superdiffusive, ballistic motion, such that

$$\langle |\boldsymbol{r}(t) - \boldsymbol{r}(0)|^2 \rangle = 3\frac{k_B T}{m} t^2 = \boldsymbol{v}^2(0) t^2 \tag{3.1.5}$$

This is the inertial behavior that comes from the initial velocity $\boldsymbol{v}(0)$, where $\boldsymbol{v}^2(0) = 3k_B T/m$. At long times $t \gg \tau_m$, the mean square displacement is the result obtained by Einstein [81] for a particle moving in three dimensions

$$\langle |\boldsymbol{r}(t) - \boldsymbol{r}(0)|^2 \rangle = 6Dt \tag{3.1.6}$$

which has the characteristic scaling of diffusive processes [89]. Note that from this result appears a characteristic time for the particle to be transported by diffusion because of thermal fluctuations on a length scale similar to its size, $t_{\mathcal{D}} = a^2/D$, where $a = 2R$ is the particle diameter. For a micron-sized particle in water at room temperature, $t_{\mathcal{D}} = \mathcal{O}(5s)$. The diffusion constant, D, is given by the Einstein relation

$$D = \frac{k_B T}{\zeta} \tag{3.1.7}$$

The Einstein relation is a powerful example of the fluctuation-dissipation theorem: the fluctuations of the particle as it undergoes its random motion are directly related to the drag force, thus, the dissipation

of momentum, that the particle feels as it moves through the fluid [90, 91] (reason why its also called Stokes-Einstein relation).

A characteristic feature of this kind of motion emerges from the stochastic nature of the delta-correlated forces, affecting not only the quadratic displacement but quadratic velocities. A simple calculation leads to obtaining the velocity correlation function between velocities, which tells us information about the velocity of the particle at time t supposing we know its velocity at a time $t = 0$. The result is that decays exponentially as

$$\langle \boldsymbol{v}(t)\boldsymbol{v}(0)\rangle = \langle \boldsymbol{v}^2(0)\rangle e^{-t/\tau_m} \tag{3.1.8}$$

This means, indeed, we can be sure that the velocities at time $t = 0$ and time t will be similar, but for longer times $t \gg \tau_m$ one would not be even closer to predicting its velocity.

In [82], Einstein further provided a description of rotational Brownian motion, reasoning that molecular collisions not only generate translational random motion but also random rotation through fluctuating thermal torques, reorienting particles stochastically in a similar manner to the former. He derived the following expression equivalent to the Stokes-Einstein relation for a particle of radius R

$$D_r = \frac{k_B T}{\zeta_r} \tag{3.1.9}$$

where $\zeta_r = 8\pi\mu R^3$ is the rotational friction coefficient. Here, the rotational diffusion constant, D_r, has dimensions of frequency, s^{-1}, although more strictly, rad^2/s. In fact, if one assigns a unit orientation vector $\boldsymbol{p}(\theta, \phi)$ to a spherical particle, the obtained mean square angle at short times, where the polar angle θ is small, is

$$\langle \theta^2(t)\rangle \approx 4D_r t \tag{3.1.10}$$

showing a diffusive behavior for the polar angle and making more clear the reason for the dimensions of D_r as rad^2/s. This result also reveals a fundamental time scale, $\tau_r = D_r^{-1}$, for a single-order reorientation of the particle (as if considering the rotation for a single degree of freedom) due to thermal fluctuations. For a micron-sized particle in water at room temperature, $D_r = 0.16\,\mathrm{rad}^2/s$, thus $\tau_r = \mathcal{O}(5s)$. Note that if we compare τ_r to the time scale for the particle to be transported by diffusion a distance of its length scale, $t_{\mathcal{D}}$, we obtain that $t_{\mathcal{D}}/\tau_r = \mathcal{O}(1)$, indicating that it takes the same amount of time to reorient itself significantly as it takes to move that distance. Additionally, similar to the case of translational motion, the orientation (3D) correlation function decays exponentially, such that

$$\langle \boldsymbol{p}(t)\boldsymbol{p}(0)\rangle = e^{-2D_r t} = e^{-t/\tau_r} \tag{3.1.11}$$

meaning that the particle initially has a determined orientation, then loses it exponentially with rate $2D_r$, i.e., with orientational relaxation time $\tau_r = 1/2D_r$.

Although the above description of Brownian motion considers inertia to play a role through the momentum relaxation time τ_m, it is clear that it does to a very small lapse in the motion of colloidal, micron-sized particles or cells. Indeed, as estimated above, at equal equilibrium conditions, $t_{\mathcal{D}} \gg \tau_m$, meaning that their motion is dominated by diffusion, as if the momentum relaxation was instantaneous, such that its MSD obeys only to Eq.(3.1.6) for all times, and their velocities become completely uncorrelated in time, so there is no "memory". Nonetheless, note that in the case of rotational motion, memory is preserved, since the relaxation time is of the same time scale as diffusion. Anyways, this allows us to make a valid approximation that lets us neglect the inertial term from the equation of motion Eq.(3.1.1), obtaining the overdamped Langevin equation of motion

$$\zeta \frac{d\boldsymbol{r}(t)}{dt} = \boldsymbol{f}_{\mathcal{B}} \tag{3.1.12}$$

which connects very well with the fact that we are seeking to model motion at a low Reynolds number. From now on, we assume this equation to govern the motion of Brownian particles, and extend it to the motion of microswimmers in the next section.

3.2 Active Brownian motion

Living microorganisms have the ability to self-propel across their medium by taking energy from it and dissipating it in the form of heat through their motion mechanism, instantly driving them far out of

thermal equilibrium [92]. In the second decade of the 20th century, with the theory of Brownian motion taking a major role in the foundation of statistical physics, exploring the nature of small living organisms in this context was of great interest. Some of the first experiments on the motion of microorganisms were performed by Karl Przibram in 1913 [93], by observing protozoa swimming in water through a microscope. In his work, for instance, he traced the trajectory of a *Paramecium* of 0.27 mm, as shown in Fig.3.2. From these experiments obtained data, Przimbram calculated and showed that the mean square displacement increased linearly in time, just as for the Brownian motion of micron-sized particles, but with a larger diffusion coefficient than the one predicted by Einstein's 1905 equilibrium kinetic theory. Furthermore, in a subsequent work [94], he reported an increased diffusion coefficient from an increasing concentration of motile planktonic rotifers (in particular, the species *Epiphanes senta*), now known to be also due to hydrodynamic interactions. Later, in 1920, Reinhold Fürth, performed experiments similar

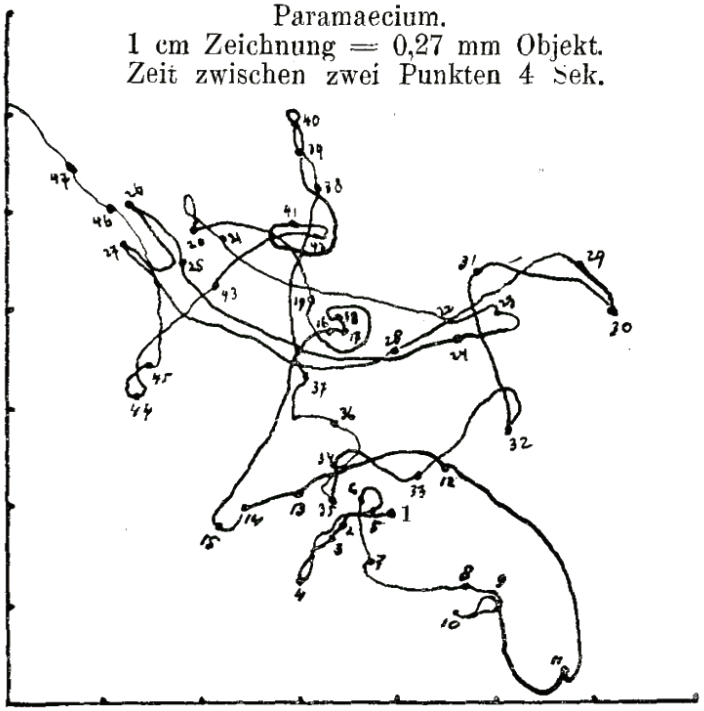

Figure 3.2: Trajectory of a Paramecium protozoan of 0.27 mm of size traced via real-time mechanical tracking with a microscope, with position measured every 4 seconds. The mesh size is 1.42 mm. Reproduced from [93].

to those of Pzribram [95]. However, as he measured the trajectory over time more frequently, he noticed that in reality, the mean square displacement was not proportional to time, but quadratically at short times, rejecting the applicability of Einstein's theory to the data obtained from his experiments. This led him to describe the motion of microorganisms differently, using the notion of persistent random (walk) motion, which became a standard model. The expression found by Fürth was the same as the one found by Ornstein and Uhlenbeck for inertial Brownian motion (see Sec.3.1), however, the former was motivated by experimental evidence focusing on motility when inertial effects were neglected and showed the same ballistic motion but for time scales much longer than one of the momentum relaxation time. The work of Przimbram and Fürth constitutes both the first experimental evidence of active Brownian motion by living organisms at the microscale, as well as the first accurate mathematical description of their motion as self-propelled particles [96], using tools from statistical physics and equilibrium kinetic theory for a phenomenon intrinsically out of equilibrium.

Just as in the case of Brownian motion, it is possible to write overdamped Langevin equations of motion for straight-swimming microswimmers as self-propelled, active Brownian particles [97, 98]. This is a paradigmatic minimal model of dry active matter [99], characterized by the absence of momentum conversation, thus no relevance of hydrodynamic interactions. In the following I present the general description of active Brownian motion given by H. Löwen in [100].

In two dimensions, the single trajectory of a particle at time t is described by its center position

vector, $\boldsymbol{r}(t) = (x(t), y(t))$ and orientation unit vector, $\boldsymbol{p}(t) = (\cos\phi(t), \sin\phi(t))$, where $\phi(t)$ is the angle of the particle orientation with the x-axis in the xy-plane, such that the equations of motion are

$$\zeta \frac{d\boldsymbol{r}(t)}{dt} = \zeta v_0 \boldsymbol{p}(t) + \boldsymbol{f}(t) \tag{3.2.1}$$

$$\zeta_r \frac{d\phi(t)}{dt} = f_r(t) \qquad \text{(2D)} \tag{3.2.2}$$

$$\zeta_r \frac{d\boldsymbol{p}(t)}{dt} = \boldsymbol{f}_r(t) \times \boldsymbol{p}(t) \qquad \text{(3D)} \tag{3.2.3}$$

where ζ and ζ_r are the translational and rotational friction coefficients, and v_0 is the self-propulsion speed of the active particle of size $a = 2R$, directed along the orientation, $\boldsymbol{p}(t)$. These equations represent the force and torque balance on the particle's translational and rotational motion originated by their surrounding's molecular agitation represented by the components of $\boldsymbol{f}(t)$ and $f_r(t)$ as Gaussian white noise, with

$$\langle \boldsymbol{f}(t) \rangle = 0 \tag{3.2.4}$$

$$\langle f_i(t) f_j(t') \rangle = 2D\zeta^2 \delta_{ij} \delta(t - t') \tag{3.2.5}$$

$$\langle f_r(t) \rangle = 0 \tag{3.2.6}$$

$$\langle f_r(t) f_r(t') \rangle = 2D_r \zeta_r^2 \delta(t - t') \tag{3.2.7}$$

where $\langle \cdot \rangle$ indicates thermal noise average, while D and D_r are the translational and rotational diffusion constants, respectively. In thermal equilibrium, both diffusion coefficients are related by the expression $D = D_r a^2/3$.

The orientational dynamics of an active Brownian particle are also characterized by the orientational correlation function (see Sec. 3.1), given by a single exponential

$$\langle \boldsymbol{p}(t) \cdot \boldsymbol{p}(0) \rangle = e^{-t/\tau_p} \tag{3.2.8}$$

where τ_p is the orientational relaxation time, defined as the persistence time

$$\tau_p = 1/D_r, \qquad \text{(2D)} \tag{3.2.9}$$

$$\tau_p = 1/2D_r. \qquad \text{(3D)} \tag{3.2.10}$$

The persistence time characterizes the duration over which a particle can track its initial orientation. After this period, the particle loses memory of its original direction. Correspondingly, one may define the persistence length,

$$\ell_p = v_0/D_r = v_0 \tau_p \tag{3.2.11}$$

which represents the distance a particle travels along its initial orientation before its motion becomes randomized.

A scaling of the equations of motion, Eq.(3.2.1) and Eq.(3.2.2) is made using the persistence time, τ_p, and persistence length, ℓ_p as units for time and length, respectively. Defining the following dimensionless parameters and functions

$$\tilde{t} = t/\tau_p, \quad \tilde{\boldsymbol{r}}(\tilde{t}) = \boldsymbol{r}(t)/\ell_p, \quad \tilde{\phi}(\tilde{t}) = \phi(t), \quad \tilde{\boldsymbol{f}}(\tilde{t}) = \sqrt{\frac{\tau_p}{2\zeta k_B T}} \boldsymbol{f}(t), \quad \tilde{f}_R(\tilde{t}) = \sqrt{\frac{\tau_p}{2\zeta_r k_B T}} f_R(t) \tag{3.2.12}$$

one obtains

$$\frac{d\tilde{\boldsymbol{r}}(\tilde{t})}{d\tilde{t}} = \tilde{\boldsymbol{p}}(\tilde{t}) + \sqrt{\frac{2D\tau_p}{\ell_p^2}} \tilde{\boldsymbol{f}}(\tilde{t}) \tag{3.2.13}$$

$$\frac{d\tilde{\phi}(\tilde{t})}{d\tilde{t}} = \sqrt{2} \tilde{f}_r(\tilde{t}) \tag{3.2.14}$$

with Gaussian white noises $\tilde{\boldsymbol{f}}(\tilde{t})$,$\tilde{f}_r(\tilde{t})$ of unit variance. From this result, a dimensionless translational diffusion coefficient is defined as

$$\tilde{D} = \frac{D}{\ell_p^2/\tau_p} = \frac{k_B T}{\zeta v_0^2 \tau_p}. \tag{3.2.15}$$

Here $\tilde{D}$ measures the strength of the translational diffusion relative to the diffusion generated by the persistent random walk, ℓ_p^2/τ_p. For $\tilde{D} \ll 1$, the particle's motion is a purely persistent random walk characterized by the persistence length and persistence time, which is normally assumed in this model, while for $\tilde{D} \gg 1$, particle's activity becomes dominated by translational diffusion, equivalent to a "passive" Brownian motion.

Additionally, another dimensionless parameter useful to quantify the importance between diffusive motion and self-propelled motion (or strength of activity) is the *Péclet number* [101, 102], Pe, which compares the characteristic time for an active particle to move a distance of its size, $t_a = a/v_0$, to the diffusive time scale, $t_\mathcal{D} = a^2/D$, such that

$$\mathrm{Pe} = \frac{t_\mathcal{D}}{t_a} = \frac{a v_0}{D} = \frac{3 v_0 \tau_p}{a}. \tag{3.2.16}$$

To emphasize the difference between the two distinct kinds of motion depending on $\tilde{D}$ is instructive to address the noise-averaged displacement as a function of time t for a prescribed initial orientation $\boldsymbol{p}(0)$ at time $t = 0$. When activity is dominated by translational diffusion ($\tilde{D} \gg 1$), although the particle is moving, it is equally likely to go in any direction, eventually going nowhere on average [86]. Then, for $t \to \infty$

$$\langle \boldsymbol{r}(t) - \boldsymbol{r}(0) \rangle = 0 \tag{3.2.17}$$

On the other hand, when persistent motion dominates ($\tilde{D} \ll 1$), we have [96]

$$\langle \boldsymbol{r}(t) - \boldsymbol{r}(0) \rangle = \frac{v_0}{D_r} \left(1 - e^{-D_r t}\right) \boldsymbol{p}(0) = \ell_p \left(1 - e^{-t/\tau_p}\right) \boldsymbol{p}(0) \tag{3.2.18}$$

so the noise-averaged displacement is a straight linear segment oriented along $\boldsymbol{p}(0)$, which at long times $t \to \infty$, has a total length equal to the persistence length ℓ_p. An intuitive interpretation of Eq.(3.2.18) is that, for a particle with persistent motion, it is possible to remember where it came from, because it was directed along its orientation for exactly a distance ℓ_p. This persistence arises because the orientation of the particle changes over time due to rotational diffusion, meaning that rotational fluctuations govern the persistence, not the translational ones. So even though the particle's trajectory might seem random, there is an underlying pattern due to the directional persistence. Fig.3.3 shows typical trajectories of passive and active Brownian particles and their corresponding diffusion regimes in terms of the passive and active diffusion parameters and the *Péclet number* Pe.

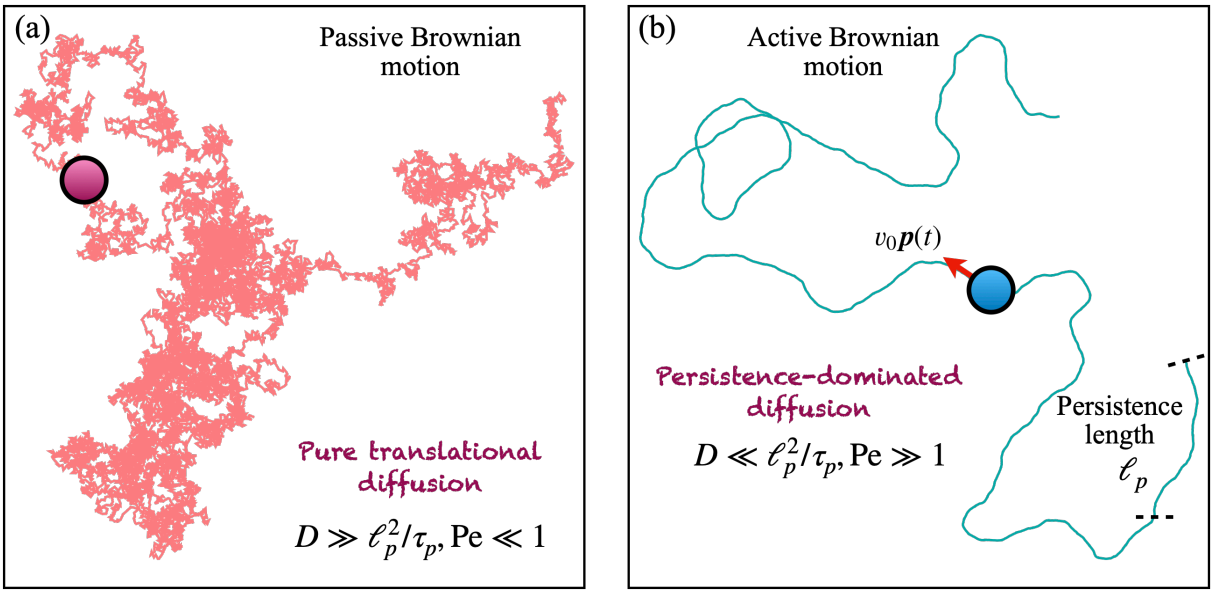

Figure 3.3: Typical trajectories of an active Brownian particle and a passive Brownian particle. (a) Trajectory of a passive Brownian particle characterized by random motion resulting in going nowhere on average. (b) The persistent random motion is characterized by retaining information about the initial orientation for a distance ℓ_p, before becoming randomized.

The mean square displacement (MSD) of an active Brownian particle in two dimensions is analytically given by [96, 103, 98]

$$\mathrm{MSD}(t) = \langle |\boldsymbol{r}(t) - \boldsymbol{r}(0)|^2 \rangle = 2\ell_p^2 \left(\frac{t}{\tau_p} - 1 + e^{-t/\tau_p} \right) + 4Dt \tag{3.2.19}$$

Due to rotational symmetry, the MSD does not depend on the initial orientation $\boldsymbol{p}(0)$. An analysis of the expression in Eq.(3.2.19) allows us to identify three regimes: For very short times, $t/\tau_p \ll \tilde{D}$, there is a diffusive behavior

$$\mathrm{MSD}(t) = 4Dt \tag{3.2.20}$$

This short-time diffusive regime can be seen in experiments if the activity of the particle is not very large [104, 105]. After the initial diffusive regime, for intermediate times, there is a superdiffusive, ballistic regime, where

$$\mathrm{MSD}(t) = v_0^2 t^2, \quad \text{for} \quad \tilde{D} \ll t/\tau_p \ll 1 \tag{3.2.21}$$

For long times, $t/\tau_p \gg 1$, the MSD becomes diffusive again, such that $\mathrm{MSD}(t) = 4D_{\mathrm{eff}}t$, however, this time with a larger long-time, effective diffusion coefficient given by

$$D_{\mathrm{eff}} = \lim_{t\to\infty} \frac{1}{4t} \langle |\boldsymbol{r}(t) - \boldsymbol{r}(0)|^2 \rangle = D + \frac{v_0^2 \tau_p}{2} = \frac{\ell_p^2}{\tau_p} (\tilde{D} + \frac{1}{2}) \tag{3.2.22}$$

For particles with strong self-propulsion, $\tilde{D} \ll 1$, D_{eff} is much larger than D. Indeed, in this case, $D_{\mathrm{eff}} = \ell_p^2/\tau_p$, consistent with the expected diffusion coefficient for persistent random motion assumed at the beginning of this analysis. Fig.3.4 shows a graphical summary of the behavior of an active Brownian particle in terms of its MSD for different self-propulsion speeds, v_0.

In the overdamped Brownian dynamics, the velocity of a particle is not a real observable since it fluctuates without constraints due to the noise induced by the surrounding fluctuating forces. Nonetheless, one still can define an averaged or drift velocity as

$$\boldsymbol{v}_d(t) = \lim_{\Delta t\to 0} \frac{\langle \boldsymbol{r}(t+\Delta t) - \boldsymbol{r}(t) \rangle}{\Delta t} = v_0 \boldsymbol{p}(t) \tag{3.2.23}$$

Then, it is possible to compute the velocity autocorrelation function, which results in a single exponential

$$\langle \boldsymbol{v}(t)\boldsymbol{v}(0) \rangle = v_0^2 e^{-t/\tau_p} = \langle \boldsymbol{v}^2(0) \rangle e^{-t/\tau_p} \tag{3.2.24}$$

decaying the persistence time, τ_p.

This section summarizes the theory necessary to understand the behavior of microswimmers on their own, without considering either short-range (repulsive) or long-range (hydrodynamic) interactions. The next section provides a rationalization of the reason for the characteristic motion of a bacterium such as the *Escherichia coli* and its connection to the model of an active Brownian particle.

3.3 Run-and-tumble and diffusion scaling

A well-studied case on the motion of microswimmers due to their inherent activity is the one of a swimming *E. coli* bacteria by Berg in [107]. In his work, he observed an interesting pattern in the motion of *E. coli*, going from periods of nearly straight swimming motion (runs, about one second long), in which they bundle their flagella in a clockwise (CW) rotation, to fast random direction reorientation events (tumbles, typically one-tenth of a second long) caused by the unbundling of their flagella due to a counter-clockwise (CCW) rotation, as shown in Fig.3.5.

A simple scaling argument by Purcell in [64] points out that they swim through this particular mechanism to outrun the dominating diffusion of the nutrient molecules in their surroundings, allowing them to compare chemical concentrations at different locations and swim towards a higher concentration location as a result of chemotaxis. In [60], E. Lauga presents Purcell's scaling argument as I describe in what follows. Consider a microswimmer moving with speed v_0 during a time interval t. The distance traveled by the microswimmer, ℓ_{swim}, scales as $\ell_{\mathrm{swim}} \sim v_0 t$. During the same interval, a particular

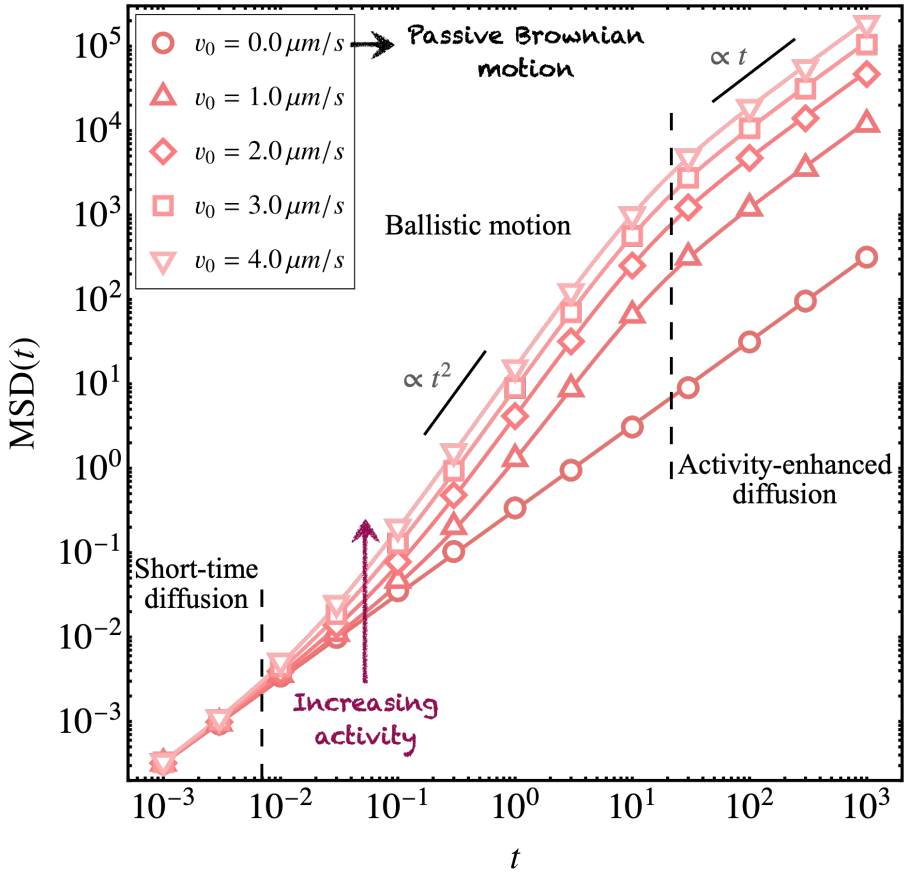

Figure 3.4: Mean square displacement (MSD) of a two-dimensional active Brownian particle for an increasing activity. Symbols are computed from numerical simulations (see, for example, [106]), while lines are theoretical curves obtained from Eq.(3.2.19).

nutrient molecule travels by an approximate distance, ℓ_{diff}, following a diffusing scaling, $\ell_{\text{diff}} \sim \sqrt{D_m t}$, where D_m is the molecular diffusion constant of the substance of interest. At very short times, diffusion always outruns the microswimmer, since $t^{1/2} \ll t$, at small t. For the microswimmer to outrun diffusion, at least it has to swim for a minimum of time t_c, such that $\ell_{\text{swim}} > \ell_{\text{diff}}$. The latter implies that

$$t > t_c = \frac{D}{U^2}. \tag{3.3.1}$$

As Purcell stated in [64], "If you don't swim that far, you haven't gone anywhere", so swimming for significantly less than t_c would not allow the microswimmer to compare concentration at different locations. On the contrary, swimming for a longer time than t_c would limit the microswimmer from exploring other convenient directions toward better nutrient concentration spots. Then, an *E. coli* outruns diffusion only for times just above t_c, tumbling after, which is exactly the aforementioned mechanism: a run and tumble. For nutrients with standard molecular diffusivities $D_m = \mathcal{O}(10^{-9} m^2/s)$ and microswimmers with speed on the order of $v_0 \approx 30\,\mu m/s$, the critical time is approximately $t_c \approx \mathcal{O}(1s)$, consistent with the average durations of runs for *E. coli* bacteria [107].

The reorientation process in the run-and-tumble motion of *E. coli* has been proven to be of stochastic nature by several experiments [77, 109]. Moreover, pre and post-tumble orientations are positively correlated, with an average change in orientation of $58 \pm 40°$ between consecutive runs [109], with mean duration τ_{run}, such that tumbles occur with the corresponding frequency, $\tau_{\text{tumble}}^{-1}$, while runs length are $\ell_{\text{run}} = v_0 \tau_{\text{run}}$. The coupling between orientation correlation and self-propelled swimming allows one to describe run-and-tumble as an effective diffusive process, adjusting with the whole concept of active Brownian motion for self-propelled particles described in Sec.3.2.

Denoting the microswimmer's unit orientation as $\boldsymbol{p}(t)$, its orientation correlation is exponentially

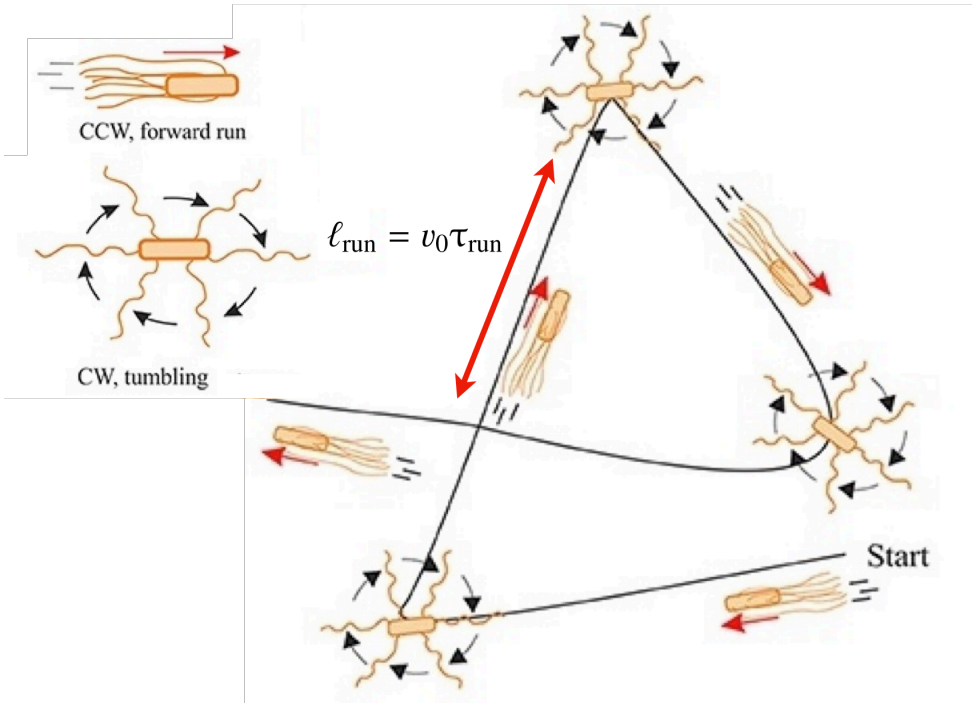

Figure 3.5: Scheme of the motion mechanism by an *E. coli* bacterium. Adapted from [108].

distributed, as for Eq.(3.2.8), such that

$$\langle \boldsymbol{p}(0) \cdot \boldsymbol{p}(t) \rangle = e^{-t/\tau_c}, \quad \text{with } \tau_c = \frac{\tau_{\text{run}}}{1-\alpha} \tag{3.3.2}$$

where $\alpha = \langle \cos\theta \rangle$ is the mean cosine of the reorientation angle (θ) between two successive runs, with an approximate value of $\alpha \approx 0.33$ [110]. Then, ignoring bare translational diffusion,$D = 0$, one can compute an effective diffusion coefficient for a bacterium performing run-and-tumble (in three dimensions) as

$$D_{\text{eff}} = D + \frac{v_0^2 \tau_{\text{run}}}{3(1-\alpha)}. \tag{3.3.3}$$

The effective diffusion coefficient for an *E. coli* swimming with speed $v_0 = 20\,\mu m/s$ and $\tau_{\text{run}} = 1\,s$ gives $\mathrm{D_{eff}} \approx 200\,\mu m^2/s$.

In [111], Saragosti et al. demonstrate that is possible to model the tumbling by rotational diffusion. For example, tumbler strain mutants that always tumble have a rotational diffusion of $D_r \approx 2.1\,\mathrm{rad}^2/s$, such that their persistence time (equivalent to the run duration time) is $\tau_{\text{run}} = 1/2D_r \approx 0.25\,s$, resulting in an effective diffusion $D_{\text{eff}} \approx 50\,\mu m^2/s$, smaller than the former case, but expected because the run duration is smaller. In comparison, a much smaller (passive) diffusion coefficient has dead unflagellate strains or flagellated paralyzed strains [112], where measured in the 2D plane of observation, $D \approx 0.17\,\mu m^2/s$ and $D_r \approx 0.11\,\mathrm{rad}^2/s$ for the first, and $D \approx 0.12\,\mu m^2/s$ and $D_r \approx 0.032\,\mathrm{rad}^2/s$ for the second. For reference, for a (non-motile) micron-sized sphere, $D \approx 0.22\,\mu m^2/s$ and $D_r \approx 0.16\,\mathrm{rad}^2/s$..

A good example of another well-studied biological model microorganism that performs run-and-tumble is the microalga *Chlamydomonas reindhartii*, a photosynthetic biflagellate eukaryote that swims by beating two anterior flagella at $\approx$ 50Hz in a breaststroke motion, analogous to human breaststroke. During the power stroke, the flagella synchronously sweep backward, remaining mostly perpendicular to the swimming direction to maximize thrust, pulling the cell forward [113]. In [114], Polin et al. showed using three-dimensional tracking that this cell swimming in the dark stochastically switches between synchronous and asynchronous flagellar beating, equivalent to go from a period of nearly straight swimming to abrupt large reorientations, every $\tau_{\text{run}} = 11.2s$, referred to as an eukaryotic version of run-and-tumble. Note that the run duration is approximately one order of magnitude larger than the one for an *E. Coli*. On the contrary, when in the presence of a light source they steer directly towards or away from it (they show both positive and negative phototaxis), not presenting any sign of the run-and-tumble motion [115].

In [70], Drescher et al. measured (in the 2D focal plane of a microscope) the rotational diffusion constants for a non-tumbling *E. coli* bacterium (of size $3\,\mu m$ and $v_0 = 22\,\mu m/s$) and a *C. reinhardtii* alga (of size $10\,\mu m$ and $v_0 \simeq 100\,\mu m/s$), both swimming freely, far from surfaces, obtaining $D_r = 0.057\,\mathrm{rad}^2/s$ and $D_r \simeq 0.4\,\mathrm{rad}^2/s$, for each, respectively. For reference, for a (non-motile) sphere of size $5\,\mu m$, we have $D_r \approx 1.32 \times 10^{-3}\,\mathrm{rad}^2/s$. As [60] indicates, for random reorientations (as in this case) $\alpha = 0$ so Eq.(3.3.3) simplifies to $D_{\text{eff}} \approx v_0^2 \tau_p/3 = v_0^2/6D_r$, so we estimate (in three-dimensions) that $D_{\text{eff}} = 2.83 \times 10^3\,\mu m^2/s$ and $D_{\text{eff}} = 8.33 \times 10^3\,\mu m^2/s$, for each microorganism respectively, so larger than the run and tumble case by at least two orders of magnitude, and more than an order of magnitude larger than the mutant tumbler case.

The above analysis gives us an idea of the scales of strength at which microorganisms can act on their environment by the mere fact of being intrinsically active.

In this chapter, I have presented the basic concepts that govern the behavior of an active agent in a dry active matter system. In the next chapter, I show how the capabilities of these active agents are exploited in a specific collective system known as Active Carpet, allowing them to impact their environment even more, by using the two great worlds explored so far in this work: microhydrodynamics and diffusion of active systems.

Chapter 4

Active carpets

Biological activity is known to concentrate on surfaces. This leads in most cases to the accumulation of biological agents that act through a collective that exhibits properties different from those that an individual agent might exhibit. These formations, sometimes called active carpets, can be key to various processes, both biological and environmental. From the point of view of physics, these formations are outside thermodynamic equilibrium, since the agents that constitute them consume energy that they then inject into the medium. In Chapter.2 I presented the hydrodynamics of these biological agents and in Chapter.3 I explained their dynamics and transport properties. In this chapter I use the above as a basis and introduce in detail the physical-mathematical theory for modeling active carpets and their collective-induced transport properties.

4.1 Definition of an active carpet

Consider a finite colony of microswimmers moving in a three-dimensional homogeneous fluid of viscosity μ, where their propulsion force and drag are balanced. In the colony, each microswimmer is located (in cartesian coordinates) at a position $\boldsymbol{r}_s = (x_s, y_s, z_s)$ and oriented along a unit orientation vector $\boldsymbol{p}_s = (p_x, p_y, p_z)$ near a non-moving interface located a the origin of coordinates, $z = 0$. Each microswimmer acts over tracer particles located at a position $\boldsymbol{r} = (x, y, z)$ above them. Conveniently, their position and orientation, together with the tracer's position can be written in cylindrical coordinates as

$$\boldsymbol{r}_s = (\rho_s \cos\varphi_s, \rho_s \sin\varphi_s, z_s) \quad \text{with} \;\; \rho_s \in [0, R], \;\; \varphi_s \in [-\pi, \pi], \tag{4.1.1}$$

$$\boldsymbol{p}_s = (\cos\phi_s \sin\theta_s, \sin\phi_s \sin\theta_s, \cos\theta_s) \quad \text{with} \;\; \phi_s \in [-\pi, \pi], \;\; \theta_s \in [0, \pi]. \tag{4.1.2}$$

$$\boldsymbol{r} = (\rho_s \cos\varphi, \rho_s \sin\varphi, z) \quad \text{with} \;\; \varphi \in [-\pi, \pi]. \tag{4.1.3}$$

where R is the radius of the colony if circular. Far from the interface (in bulk), each microswimmer is modeled as a dipole point force (see Sec.2.3), generating a (Stokeslet) flow field

$$\boldsymbol{u}(\boldsymbol{r}, \boldsymbol{r}_s, \boldsymbol{p}) = \kappa(\boldsymbol{p}_s \cdot \nabla_s)(\mathcal{G}(\boldsymbol{r}, \boldsymbol{r}_s) \cdot \boldsymbol{p}_s) \tag{4.1.4}$$

where κ is the dipole strength, $\mathcal{G}$ is the Oseen tensor and $\nabla_s \equiv \partial/\partial \boldsymbol{r}_s$ is the gradient operator with derivatives taken with respect to the microswimmer position $\boldsymbol{r}_s$.

On the contrary to bulk, as considered here, near the interface, each microswimmer's flow field must fulfill the appropriate hydrodynamic boundary conditions induced by that interface, which is done by using the method of images (see Sec.2.4). For this, consider an image microswimmer located at position $\boldsymbol{r}_s^* = (x_s, y_s, z_s^*)$, with orientation $\boldsymbol{p}_s$. The corresponding image flow field generated by this microswimmer is given by

$$\boldsymbol{u}^*(\boldsymbol{r}, \boldsymbol{r}_s^*, \boldsymbol{p}_s) = \kappa(\boldsymbol{p}_s \cdot \nabla_s)(\mathcal{Y}(\boldsymbol{r}, \boldsymbol{r}_s^*) \cdot \boldsymbol{p}_s) \tag{4.1.5}$$

where the tensor $\mathcal{Y}$ represents the image system of singularities that allows to satisfy the boundary conditions at the interface when summed with the real flow field, Eq.(4.1.4). Then, the effective flow field produced by each microswimmer moving above the interface is given by

$$\boldsymbol{u}(\boldsymbol{r}, \boldsymbol{r}_s, \boldsymbol{r}_s^*, \boldsymbol{p}_s) = \kappa(\boldsymbol{p}_s \cdot \nabla_s)(\mathcal{I}(\boldsymbol{r}, \boldsymbol{r}_s, \boldsymbol{r}_s^*) \cdot \boldsymbol{p}_s) \tag{4.1.6}$$

where $\mathcal{I}(\boldsymbol{r}, \boldsymbol{r}_s, \boldsymbol{r}_s^*) = \mathcal{G}(\boldsymbol{r}, \boldsymbol{r}_s) + \mathcal{Y}(\boldsymbol{r}, \boldsymbol{r}_s^*)$. For fluids in more complex geometries, where, for example, there is more than one interface [4], generating hydrodynamic confinement, one might need another image system, located at a new position $\boldsymbol{r}_s^{**}$, say, $\mathcal{W}(\boldsymbol{r}, \boldsymbol{r}_s^{**})$. In fact, the latter is the basis of this thesis work and is considered further below.

Then, an *Active Carpet*, abbreviated as *AC* (or *ACs* in plural), is defined as a colony (or cluster) of finite size R (or infinite if $R \to \infty$ as presented further below), composed of N_s microswimmers distributed over a plane at a fixed height $z_s = h$, swimming parallel to an infinite, non-moving interface located at the origin of a three-dimensional space, $z = 0$, in a cartesian coordinate system. In the active carpet, each microswimmer has a position $\boldsymbol{r}_s = (\rho_s \cos\varphi_s, \rho_s \sin\varphi_s, h)$, is oriented along a unit orientation vector $\boldsymbol{p}_s = (\cos\phi_s, \sin\phi_s, 0)$ and produces an effective flow field $\boldsymbol{u}(\boldsymbol{r}, \boldsymbol{r}_s, \boldsymbol{p}_s)$, Eq.(4.1.6), over a tracer (point) particle located at position $\boldsymbol{r}$ on which the flow is evaluated. Note that although we consider the flow field produced by microswimmers, one might use any flow disturbance concerned with the modeling of biological (swimming or sessile) microorganisms or swimming bio-inspired objects, which makes an active carpet powerful in a broad sense, even across length and time scales.

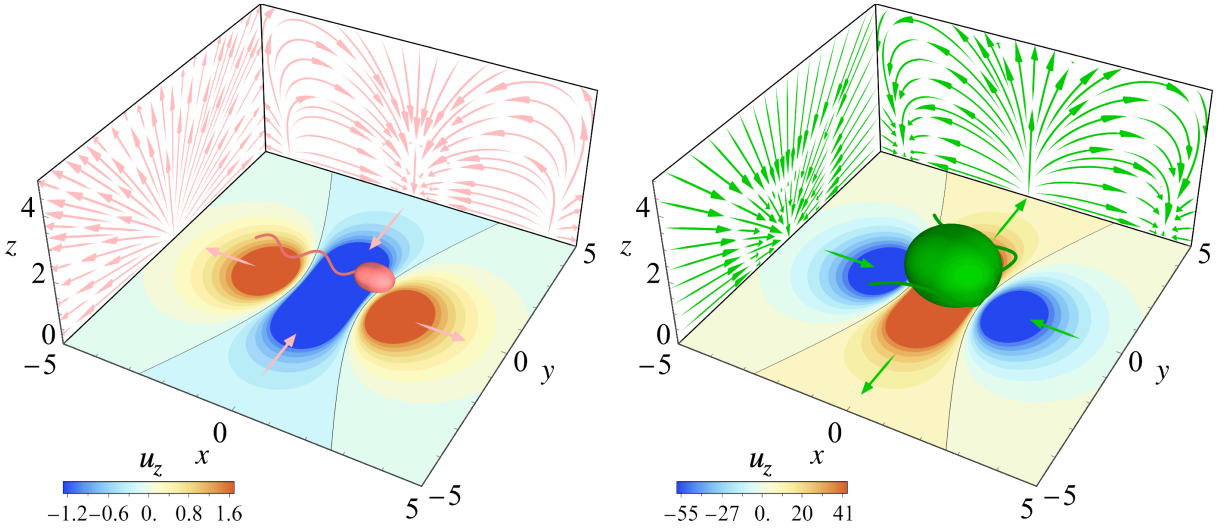

Figure 4.1: Single microswimmer flow in a carpet near a solid boundary produced by a bacterium (left panel) and an alga (right panel). Streamlines (pink and green, respectively) are shown for flows at $y = \pm 5\,\mu m$ (side view) and $x = \pm 5\,\mu m$ (front view) from the boundary to $z = 5\,\mu m$. Contours are the vertical velocities.

An active carpet is fundamentally characterized by its spatial architecture, i.e., the spatial distribution of microswimmers, formally defined by the probability density $f(\boldsymbol{r}_s, \boldsymbol{p}_s)$ of finding a microswimmer at position $\boldsymbol{r}_s$ with orientation $\boldsymbol{p}_s$. In particular, a carpet consisting of N_s microswimmers uniformly distributed and randomly oriented within a disk of radius R centered at the origin (without loss of generality) has a constant surface concentration $n = N_s/(\pi R^2)$, such that the carpet spatial distribution function is given by

$$f(\boldsymbol{r}_s, \boldsymbol{p}_s) = N_s \frac{\delta(z_s - h)\Theta(R - \rho_s)}{\pi R^2} \frac{\delta(|\boldsymbol{p}_s| - 1)\delta(\boldsymbol{p}_s \cdot \hat{z})}{2\pi}. \tag{4.1.7}$$

where $\Theta(x)$ and $\delta(x)$ are the Heaviside and Dirac delta functions. The domain of $\boldsymbol{r}_s$ and $\boldsymbol{p}_s$ allows to reduce the distribution function, which is also separable, as

$$f(\rho_s, \varphi_s, \phi_s) = N_s f_{\rho_s} f_{\varphi_s} f_{\phi_s} = N_s \frac{2}{R^2} \frac{1}{2\pi} \frac{1}{2\pi} = \frac{N_s}{\pi R^2} \frac{1}{2\pi} = \frac{n}{2\pi} \tag{4.1.8}$$

and it is normalized so that integrated it gives the number of microswimmers,

$$\int f(\boldsymbol{r}_s, \boldsymbol{p}_s) d\boldsymbol{r}_s d\boldsymbol{p}_s = \int_0^R \int_{-\pi}^{\pi} \int_{-\pi}^{\pi} \frac{N_s}{\pi R^2} \frac{1}{2\pi} \rho_s d\rho_s d\varphi_s d\phi_s = N_s. \tag{4.1.9}$$

See the SI from [2] for a more realistic approach using a Gaussian density profile.

In a general case where microswimmers are allowed to be oriented out of the plane of the carpet, the carpet distribution function is

$$f(\boldsymbol{r}_s, \boldsymbol{p}_s) = N_s \frac{\delta(z_s - h)\Theta(R - \rho_s)}{\pi R^2} \frac{\delta(|\boldsymbol{p}_s| - 1)}{4\pi}. \tag{4.1.10}$$

This distribution is normalized as before and reduces to $f(\rho_s, \varphi_s, \theta_s, \phi_s) = n/(4\pi)$.

Finally, note that if instead of being uniformly distributed over a disk of radius R, the microswimmers are distributed over a square of side $2L$, where $x_s, y_s \in [-L, L]$, the distribution function is written similarly as

$$f(x_s, y_s, \phi_s) = N_s f_{x_s} f_{y_s} f_{\phi_s} = N_s \frac{1}{2L}\frac{1}{2L}\frac{1}{2\pi} = \frac{N_s}{(2L)^2}\frac{1}{2\pi} = \frac{n_s}{2\pi} \tag{4.1.11}$$

where $n_s = N_s/(2L)^2$ is the square's surface concentration.

4.2 Average flow field due to an active carpet

Taken together, the average total flow (also named net drift or mean drift flow) due to all microswimmers combined evaluated at position $\boldsymbol{r}$ is given by

$$\langle \boldsymbol{v}(\boldsymbol{r}) \rangle = \int \boldsymbol{u}(\boldsymbol{r}, \boldsymbol{r}_s, \boldsymbol{p}_s) f(\boldsymbol{r}_s, \boldsymbol{p}_s) d\boldsymbol{r}_s d\boldsymbol{p}_s. \tag{4.2.1}$$

Again, considering the general case where microswimmers can be oriented out of the plane of the carpet (although not used in what follows), using the cylindrical and spherical coordinates defined in Sec.4.1, Eq.(4.1.1) and Eq.(4.1.2) respectively, the average total flow field is written explicitly as

$$\langle \boldsymbol{v}(\boldsymbol{r}) \rangle = \int_{\boldsymbol{\rho}_s=0}^{\boldsymbol{\rho}_s=R} \int_{\varphi_s=-\pi}^{\varphi_s=\pi} \int_{\phi_s=-\pi}^{\phi_s=\pi} \int_{\theta_s=0}^{\theta_s=\pi} \boldsymbol{u}(\boldsymbol{r}, \rho_s, \varphi_s, \theta_s, \phi_s) f(\rho_s, \varphi_s, \theta_s, \phi_s) \underbrace{\rho_s d\rho_s d\varphi_s}_{\text{Position}} \underbrace{\sin\theta_s d\theta_s d\phi_s}_{\text{Orientation}}. \tag{4.2.2}$$

For parallel microswimmers (this is, for $\theta_s = \pi/2$), as considered in the definition of an active carpet, Eq.(4.2.2) reduces to

$$\langle \boldsymbol{v}(\boldsymbol{r}) \rangle = \int_{\boldsymbol{\rho}_s=0}^{\boldsymbol{\rho}_s=R} \int_{\varphi_s=-\pi}^{\varphi_s=\pi} \int_{\phi_s=-\pi}^{\phi_s=\pi} \boldsymbol{u}(\boldsymbol{r}, \rho_s, \varphi_s, \phi_s) f(\rho_s, \varphi_s, \phi_s) \rho_s d\rho_s d\varphi_s d\phi_s. \tag{4.2.3}$$

To find the average total flow field due to an active carpet of parallel microswimmers, we must first compute the flow field of a single microswimmer in the carpet and then evaluate the integral from Eq.(4.2.3) together with Eq.(4.1.7). However, in general, this is not trivial, since these flow fields are quite complex when evaluated algebraically. Therefore, to make progress it is convenient to approximate the flows as being evaluated far from the interface, such that $h \ll z$. Making $h = \epsilon z$ with $\epsilon \ll 1$, we perform a Taylor expansion to first order in ϵ over the single microswimmer flow about $\epsilon = 0$,

$$\boldsymbol{u}(\boldsymbol{r}, \boldsymbol{r}_s, \boldsymbol{p}_s) = \boldsymbol{u}(\boldsymbol{r}, \boldsymbol{r}_s, \boldsymbol{p}_s)|_{\epsilon=0} + \left.\frac{\partial \boldsymbol{u}(\boldsymbol{r}, \boldsymbol{r}_s, \boldsymbol{p}_s)}{\partial \epsilon}\right|_{\epsilon=0} \epsilon + \mathcal{O}(\epsilon^2) \tag{4.2.4}$$

where $\boldsymbol{r} = (\rho\cos\varphi, \rho\sin\varphi, z)$, from Eq.(4.1.3), such that we explicitly have $\boldsymbol{u}(\rho, z, \rho_s, \varphi_s, \phi_s)$. Note that after doing the approximation, flows must not be dependent on ϵ, it's necessary to recover the dependency in h,z by using the relation $\epsilon = h/z$.

4.2.1 Average flow directly above the carpet

Directly above the carpet, i.e., on the z axis, we have that $\rho = 0$, such that the flow is evaluated at position $\boldsymbol{r} = (0, 0, z)$. In this case, we explicitly have that $\boldsymbol{u}(\boldsymbol{r}_s, \boldsymbol{p}_s) = \boldsymbol{u}(z, \rho_s, \varphi_s, \phi_s)$. In what follows I present the approximated individual flows produced by a microswimmer computed using Eq.(4.2.4) when the interface is a solid boundary, a free surface, and a fluid-fluid interface with viscosities ratio λ (see Sec.2.4), together with the average flow resulting from the integration of Eq.(4.2.3), as a function of the height z and the carpet radius R, $\langle \boldsymbol{v}(z, R) \rangle$.

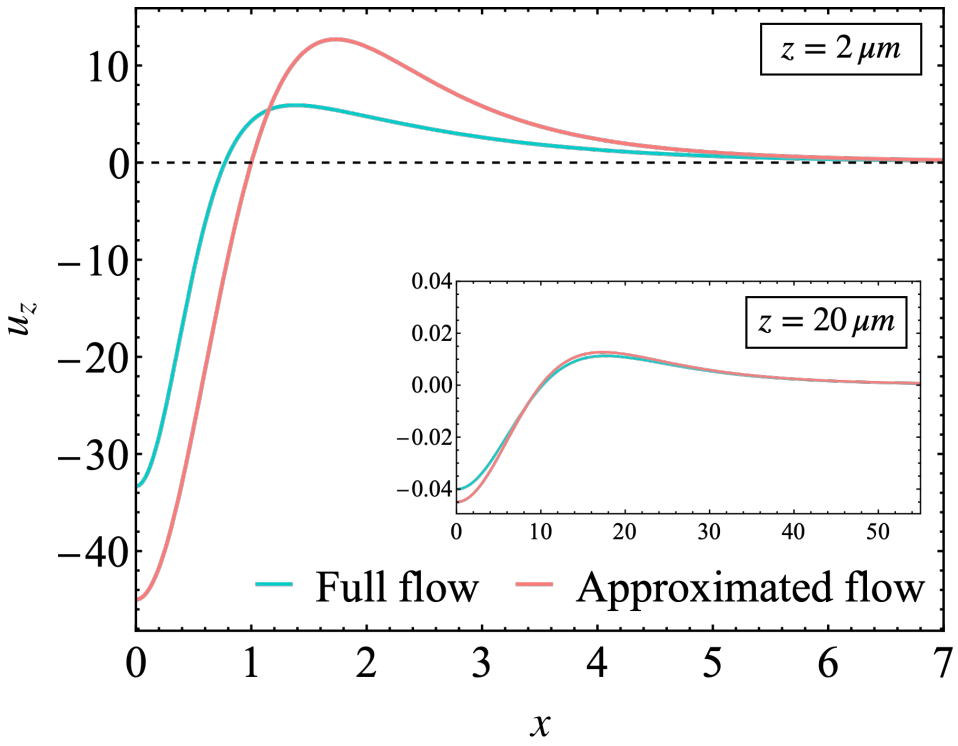

Figure 4.2: Comparison between the full flow field (cyan) and the approximated flow (pink) for $h \ll z$ at two different heights (a) $z = 2\,\mu m$ and (b) $z = 20\,\mu m$, when the interface is set as a solid boundary.

- For a solid boundary, the individual approximated flow components are

$$u_x = \frac{3h\kappa z\rho_s\left(-5\rho_s^2(\cos(2\phi_s - 3\varphi_s)) + (2z^2 - 3\rho_s^2)\cos(2\phi_s - \varphi_s) + \cos(\varphi_s)(6z^2 - 4\rho_s^2)\right)}{\left(\rho_s^2 + z^2\right)^{7/2}} \tag{4.2.5}$$

$$u_y = \frac{3h\kappa z\rho_s\left(5\rho_s^2(\sin(2\phi_s - 3\varphi_s)) + (2z^2 - 3\rho_s^2)\sin(2\phi_s - \varphi_s) + \sin(\varphi_s)(6z^2 - 4\rho_s^2)\right)}{\left(\rho_s^2 + z^2\right)^{7/2}} \tag{4.2.6}$$

$$u_z = \frac{6h\kappa z^2\left(\rho_s^2\left(5\cos\left(2\left(\phi_s - \varphi_s\right)\right) + 3\right) - 2z^2\right)}{\left(\rho_s^2 + z^2\right)^{7/2}} \tag{4.2.7}$$

  Then, the average flow is

$$\langle \boldsymbol{v}(z,R)\rangle = -12\pi nh\kappa\frac{z^2R^2}{(z^2+R^2)^{5/2}}\hat{\boldsymbol{z}} \tag{4.2.8}$$

  with optimal (maximized flow) carpet size $R^* = \sqrt{2/3}z$.

- For a free surface, the individual approximated flow components are

$$u_x = -\frac{\kappa\rho_s\cos\left(\varphi_s\right)\left(\rho_s^2\left(3\cos\left(2\left(\phi_s - \varphi_s\right)\right) + 1\right) - 2z^2\right)}{\left(\rho_s^2 + z^2\right)^{5/2}} \tag{4.2.9}$$

$$u_y = -\frac{\kappa\rho_s\sin\left(\varphi_s\right)\left(\rho_s^2\left(3\cos\left(2\left(\phi_s - \varphi_s\right)\right) + 1\right) - 2z^2\right)}{\left(\rho_s^2 + z^2\right)^{5/2}} \tag{4.2.10}$$

$$u_z = \frac{\kappa z\left(\rho_s^2\left(3\cos\left(2\left(\phi_s - \varphi_s\right)\right) + 1\right) - 2z^2\right)}{\left(\rho_s^2 + z^2\right)^{5/2}} \tag{4.2.11}$$

  Then, the average flow is

$$\langle \boldsymbol{v}(z,R)\rangle = -2\pi n\kappa\frac{zR^2}{(z^2+R^2)^{3/2}}\hat{\boldsymbol{z}} \tag{4.2.12}$$

  with optimal (maximized flow) carpet size $R^* = \sqrt{2}z$.

- For a fluid-fluid interface with viscosities ratio λ, the individual approximated flow components are

$$\begin{aligned} u_x =& -\frac{\kappa\rho_s}{2(\lambda+1)\left(\rho_s^2+z^2\right)^{7/2}}\left(-4z^3\left(3h\lambda\cos\left(2\phi_s-\varphi_s\right)+\left(9h\lambda+z\right)\cos\left(\varphi_s\right)\right)\right. \\ &+z\rho_s^2\left(-2(z-12h\lambda)\cos\left(\varphi_s\right)+3(10h\lambda+z)\cos\left(2\phi_s-3\varphi_s\right)\right. \\ &\left.\left.+\ 3(6h\lambda+z)\cos\left(2\phi_s-\varphi_s\right)\right)+2\rho_s^4\cos\left(\varphi_s\right)\left(3\cos\left(2\left(\phi_s-\varphi_s\right)\right)+1\right)\right) \end{aligned} \tag{4.2.13}$$

$$\begin{aligned} u_y =& \frac{\kappa\rho_s}{2(\lambda+1)\left(\rho_s^2+z^2\right)^{7/2}}\left(4z^3\left(3h\lambda\sin\left(2\phi_s-\varphi_s\right)+\left(9h\lambda+z\right)\sin\left(\varphi_s\right)\right)\right. \\ &+z\rho_s^2\left(2(z-12h\lambda)\sin\left(\varphi_s\right)+3(10h\lambda+z)\sin\left(2\phi_s-3\varphi_s\right)\right. \\ &\left.\left.-3(6h\lambda+z)\sin\left(2\phi_s-\varphi_s\right)\right)-2\rho_s^4\sin\left(\varphi_s\right)\left(3\cos\left(2\left(\phi_s-\varphi_s\right)\right)+1\right)\right) \end{aligned} \tag{4.2.14}$$

$$\begin{aligned} u_z =& \frac{\kappa z}{(\lambda+1)\left(\rho_s^2+z^2\right)^{7/2}}\left(z\rho_s^2\left(18h\lambda+3(10h\lambda+z)\cos\left(2\left(\phi_s-\varphi_s\right)\right)-z\right)-2z^3(6h\lambda+z)\right. \\ &\left.+\ \rho_s^4\left(3\cos\left(2\left(\phi_s-\varphi_s\right)\right)+1\right)\right) \end{aligned} \tag{4.2.15}$$

  Then, the average flow is

$$\langle\boldsymbol{v}(z,R)\rangle=-2\pi n\kappa\frac{zR^2\left(z(6h\lambda+z)+R^2\right)}{(\lambda+1)\left(R^2+z^2\right)^{5/2}}\hat{\boldsymbol{z}} \tag{4.2.16}$$

  with optimal (maximized flow) carpet size

$$R^*=\frac{\sqrt{\sqrt{3}\sqrt{z^2\left(108h^2\lambda^2+4h\lambda z+3z^2\right)}-18h\lambda z+z^2}}{\sqrt{2}} \tag{4.2.17}$$

  Note that in the limit $\lambda\to\infty$, one recovers Eq.(4.2.8), while for $\lambda=0$, one recovers Eq.(4.2.12).

A comparison between the full and the approximated flow is shown in Fig.4.2, for a microswimmer located at the center of the carpet, $\rho_s=0$, and oriented in the $\hat{\boldsymbol{x}}$ direction ($\phi_s=0$), while the interface is set as a solid boundary. At $z=2\,\mu m$ the velocities differ by a factor of approximately two with the approximated flow on the larger side, white $z=20\,\mu m$, apart from the flow being smaller (since it is far away from the boundary), both flows are approximately equal.

In Fig.4.3 are shown the analytical results obtained in Eq.(4.2.8),Eq.(4.2.12) and Eq.(4.2.16). Note that for solid and solid-like interfaces (solid boundary and fluid-fluid interface with $\lambda=10$) the average flows are small (although of the same order of magnitude) compared to the ones for fluid-fluid interfaces (free surface and fluid-fluid interface with $\lambda=0.1$).

4.2.2 Average flow everywhere above the carpet

For all space above the carpet, i.e., for all other positions $\rho\neq 0$ (see Fig.4.4(a) for a scheme), the approximated individual flow components are computed easily and one can still integrate Eq.(4.2.3), although the integral over positions ρ_s can be challenging due to the complete elliptic integrals appearing from the angular integration (see the Supplementary Information from [2] for the obtained expression for a solid boundary). In the following, instead of doing the integrals analytically, I compute them numerically and present the results in Fig.4.4, where I show the streamlines of the average flows, explicitly, $\langle\boldsymbol{v}(\rho,z)\rangle=\langle v_x(\rho,z)\rangle\hat{\boldsymbol{x}}+\langle v_z(\rho,z)\rangle\hat{\boldsymbol{z}}$ (this is, for $\varphi=0$), together with the average vertical flows $\langle v_z(\rho,z)\rangle$ as contours.

An active carpet near a solid boundary generates a steady current that brings tracer particles (nutrients) down towards the surface. As Fig.4.4(b) shows, the carpet yields a down-welling region for all lateral distance $\rho<R$ and all heights $z>h$, despite the random swimmer orientations and thermal particle diffusion. Subsequently, the tracer particles move from the center of the carpet to beyond its edge, $\rho>R$, where fluid is transported back up, resulting in a large toroidal recirculation as consequence of steep velocity gradients (boundary layer, due to no-slip condition), leading to significant flow up to approximately 40 times the size of a micron-sized bacterium. Indeed, maximizing the average flow with respect to z, gives $z^*=\sqrt{2/3}R$, which for a carpet of size $R\sim 50\,\mu m$ and a bacterial density

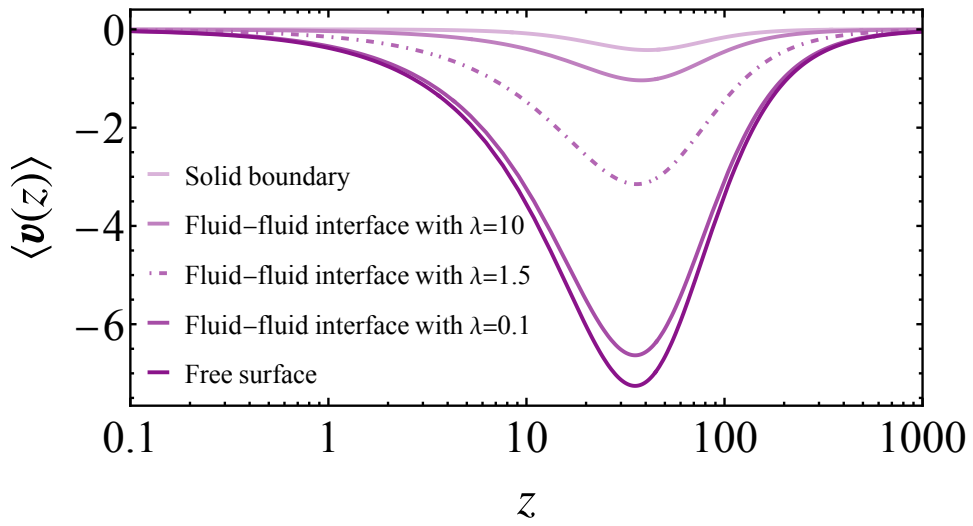

Figure 4.3: Average flow produced by an active carpet for $h = 1\,\mu m$, $n = 0.1\,\mu m^{-2}$, $\kappa = 30\,\mu m^3/s$ near five different interfaces directly above the carpet as function the height z for a carpet of radius $R = 50\,\mu m$.

$n \sim 0.1/\mu m^{-2}$(relatively high but not unphysical [116]), results in $z^* \sim 40\,\mu m$, so maximum nutrient transport is up to $|\langle \boldsymbol{v}(z^*)\rangle| \sim 0.4\,\mu m/s$.

Similarly, an active carpet near a free surface, as shown in Fig.4.4(f), also generates a steady current towards the surface, although on a order of magnitude stronger than the one near a solid boundary. In this case, there is still a down-welling region for all lateral distance $\rho < R$ and all heights $z > h$, while for $\rho > R$, although fluid is still transported back up, it does on a larger length scale and does not recirculate because of the fluid being stress-free (zero-shear stress condition) at the boundary (there is no velocity gradients,i.e., no boundary layer). Here maximum nutrient transport is up to $|\langle \boldsymbol{v}(z^*)\rangle| \sim 7\,\mu m/s$ at a height $z^* = \sqrt{2}R \sim 35\,\mu m$ for $R \sim 50\,\mu m$. Fig.4.4(c),(d),(e) are intermediate cases resulting from the action of an active carpet near a fluid-fluid interfaces.

As a final comment on the average produced by finite-sized carpets is that there is at least two configurations of uniform carpets whose individual flows combined do not lead to any net drift. The first one is a carpet of parallel Stokeslets, e.g., ciliary arrays, where force alignment is essential for microbiological transport. Indeed, since flows are symmetric, $\boldsymbol{u}(\hat{\boldsymbol{x}}) = -\boldsymbol{u}(-\hat{\boldsymbol{x}})$, they vanish when averaging over orientations $\boldsymbol{p}_s$, on the contrary to dipoles, where their flow reflection is additive, $\boldsymbol{u}(\hat{\boldsymbol{x}}) = \boldsymbol{u}(-\hat{\boldsymbol{x}})$, leading to net flow as shown above. The second configuration is a carpet of dipoles in bulk, where they are allowed to be oriented in three dimensions. Again, they do not generate any net flow since each flow is balanced due to the incompressibility condition $\nabla \cdot \boldsymbol{u} = 0$ (there is no sources nor sinks), although the may still contribute to enhanced diffusive flows. In [2], Mathijssen et al. show in detail that coherent transport arises not only from uniform concentration densities of microswimmers, but especially from gradients in density, activity or orientation, which emerge from the long-ranged order in collective behavior, such as in bacterial vortex arrays bacterial turbulence or more complex geometrical orientation patterns such as topological deffects.

4.2.3 Simulations of active carpet flows

Besides analytical and numerical integration, the average flow due to an active carpet can also be approximated in numerical simulations. To determine it, N_s microswimmers with positions $\boldsymbol{r}_{s,i}$ and orientations $\boldsymbol{p}_{s,i}$ must be placed above the interface, at $z_s = h$, then each of their (exact) individual flows are summed, such that

$$\langle \boldsymbol{v}(\boldsymbol{r})\rangle = \sum_{i=1}^{N_s} \boldsymbol{u}_i(\boldsymbol{r}, \boldsymbol{r}_{s,i}, \boldsymbol{p}_{s,i}) \tag{4.2.18}$$

where $\langle ...\rangle$ denotes averaging over a statistical number of ensembles N_e of independent active carpet configurations. Importantly, $\boldsymbol{r}_{s,i}$ and $\boldsymbol{p}_{s,i}$ are found numerically via inverse transform sampling (Smirnov

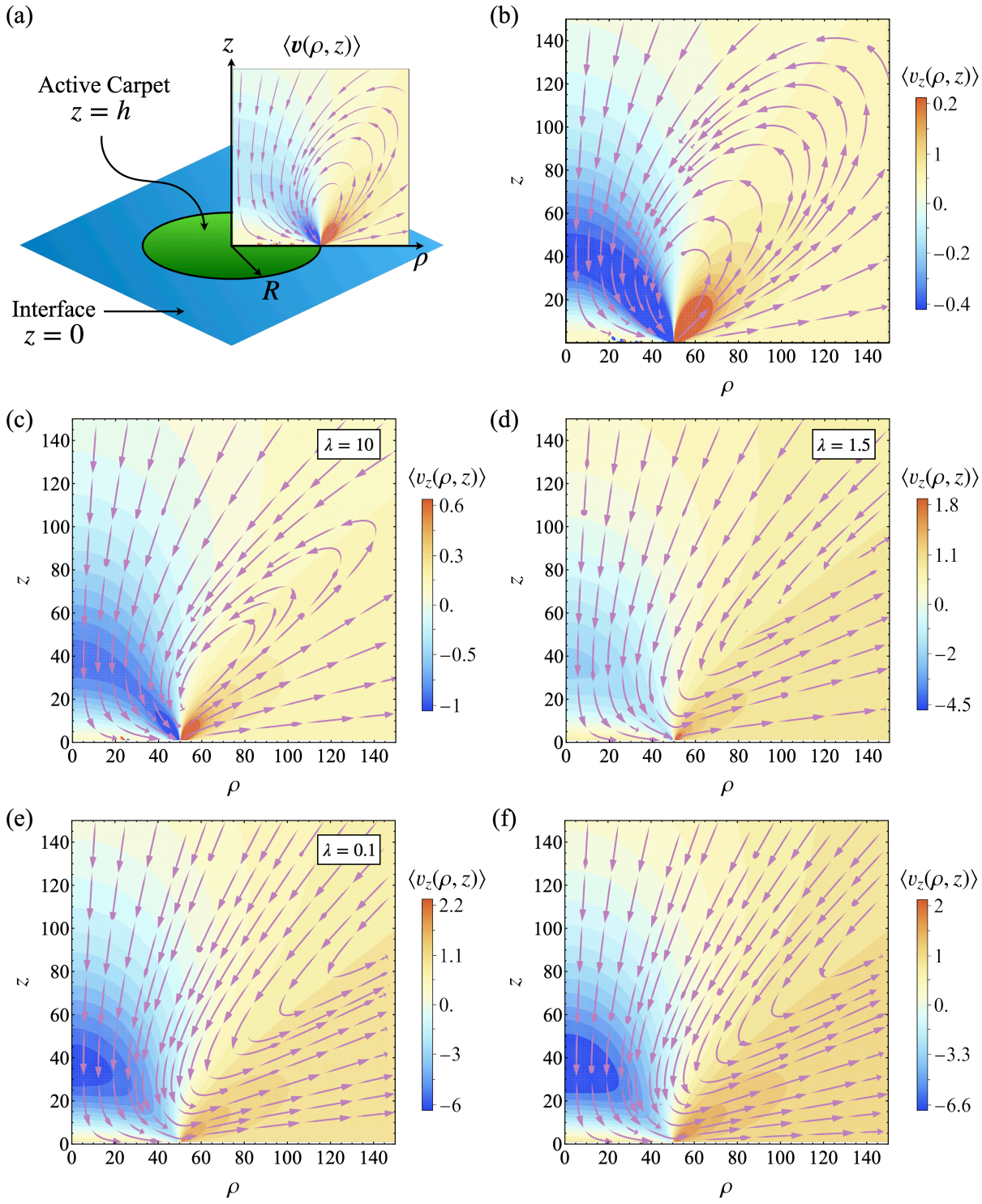

Figure 4.4: Average flow produced by an active carpet for $h = 1\,\mu m$, $n = 0.1\,\mu m^{-2}$, $\kappa = 30\,\mu m^3/s$ near five different interfaces everywhere above the carpet, $\rho \neq 0$.(a) Scheme of the physical system, where the active carpet of radius R is a height h above an interface and generates an average flow $\langle \boldsymbol{v}(\rho, z) \rangle$, shown for $\varphi = 0$, where in purple are the streamlines and contours represent the vertical average flow $\langle v_z(\rho, z) \rangle$. The latter is shown for the interface set as a (b) solid boundary, fluid-fluid interfaces with (c) $\lambda = 10$, (d) $\lambda = 1.5$, (e) $\lambda = 0.1$, and a (f) free surface.

transform) in order to satisfy the carpet probability distribution $f(\boldsymbol{r}_s, \boldsymbol{p}_s)$, Eq.(4.1.8).

Recalling that in cylindrical coordinates we have that positions are $\boldsymbol{r}_s = (\rho_s \cos\varphi_s, \rho_s \sin\varphi_s, h)$, while

orientations are $\boldsymbol{p}_s = (\cos\phi_s, \sin\phi_s, 0)$, with domain $\rho_s \in [0, R]$, $\varphi_s \in [-\pi, \pi]$ and $\phi_s \in [-\pi, \pi]$, and the carpet probability distribution is given by $f(\rho_s, \varphi_s, \phi_s) = N_s f_{\rho_s} f_{\varphi_s} f_{\phi_s}$, where $f_{\varphi_s} = f_{\phi_s} = 1/(2\pi)$ are the angular distributions, and $f_{\rho_s} = 2/R^2$ is the radial distribution, the sampling goes as follows. Consider the three random variates $w_i \in [0, 1]$ with $i \in [1, 2, 3]$ drawn from a standard uniform distribution:

- To sample the angle φ_s, we compute the cumulative distribution function (CDF)

$$F_{\varphi_s}(\varphi_s) = \int_{\varphi_s'=-\pi}^{\varphi_s'=\varphi_s} f_{\varphi_s}(\varphi_s')d\varphi_s' = \int_{\varphi_s'=-\pi}^{\varphi_s'=\varphi_s} \frac{1}{2\pi} d\varphi_s' = \frac{1}{2\pi}(\varphi_s + \pi) \tag{4.2.19}$$

  Next, we solve the inverse transform, $w_1 = F_{\varphi_s}(\varphi_s)$, obtaining the sampling

$$\varphi_s = -\pi + 2\pi w_1. \tag{4.2.20}$$

  We obtain the same sampling for ϕ_s,

$$\phi_s = -\pi + 2\pi w_2. \tag{4.2.21}$$

- To sample the distance ρ_s, we compute the cumulative distribution function (CDF)

$$F_{\rho_s}(\rho_s) = \int_{\rho_s'=0}^{\rho_s'=\rho_s} f_{\rho_s}(\rho_s')\rho_s' d\rho_s' = \int_{\rho_s'=0}^{\rho_s'=\rho_s} \frac{2}{R^2}\rho_s' d\rho_s' = \frac{\rho_s^2}{R^2} \tag{4.2.22}$$

  Next, we solve the inverse transform $w_3 = F_{\rho_s}(\rho_s)$, obtaining the sampling

$$\rho_s = R\sqrt{w_3}. \tag{4.2.23}$$

Fig.4.5 shows a visualization of the simulation sampling for an active carpet uniformly distributed within a disk.

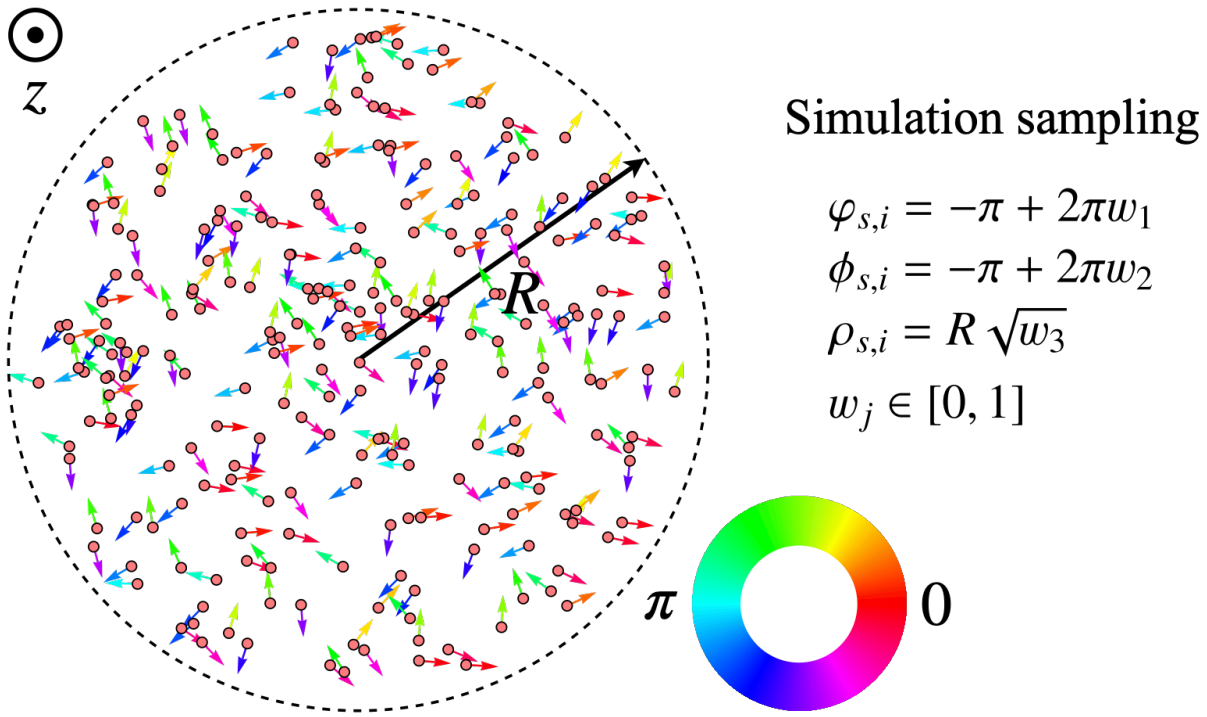

Figure 4.5: Active carpet flow simulation sampling visualization. An active carpet of $N_s = 250$ microswimmers is uniformly distributed within a disk of radius $R = 500\,\mu m$, viewed from above. The positions of the microswimmers sampled by $\rho_{s,i}$ and $\varphi_{s,i}$, are represented by pink disks, while their orientations are represented by coloured arrows coded by their orientation angles $\phi_{s,i}$, as indicated by the color wheel.

Now, the above is considering a carpet distribution within a disk of radius R. For a carpet distribution within a square of side $2L$ (see Eq.(4.1.11)) the sampling is similar. Recalling that the microswimmer positions in cartesian coordinates are $\boldsymbol{r}_s = (x_s, y_s, z_s)$ and orientations $\boldsymbol{p}_s$ are written as above, with $x_s, y_s \in [-L, L]$ and $\phi_s \in [-\pi, \pi]$, the carpet distribution is given by $f(x_s, y_s, \phi_s) = N_s f_{x_s} f_{y_s} f_{\phi_s}$ with spatial distributions $f_{x_s} = f_{y_s} = 1/(2L)$ and angular distribution $f_{\phi_s} = 1/(2\pi)$. Then, the sampling in terms of w_i is obtained as before, resulting in

$$\phi_s = -\pi + 2\pi w_1, \tag{4.2.24}$$
$$x_s = -L + 2L w_2, \tag{4.2.25}$$
$$y_s = -L + 2L w_3. \tag{4.2.26}$$

Note that the numerical sampling must be better when simulating flows of carpets at low z values. This is quite simple: at high z, many microswimmer flows contribute approximately equally, but this does not happens at low z, since only a few microswimmers are nearby. Thus, many simulations samples are needed to achieve an equivalent averaging over the microswimmer positions and orientations. This covers well the sampling for uniform carpet distributions, but see the SI from [2] for an overview of active carpet flow simulations for more complex carpet distributions.

4.3 Non-equilibrium diffusion due to an active carpet

Counterintuitively to what occurs for finite carpets, in the absence of gradients, larger homogeneous (uniform) carpets do not transport faster. Indeed, in the thermodynamic limit, $R, N_s \to \infty$ with constant n, on average, all individual microswimmer flows cancel each other out, so there is no coherent transport to the surface, i.e., the average flow (or net drift) vanishes

$$\lim_{N_s, R\to\infty} \langle \boldsymbol{v}(z, R) \rangle = \boldsymbol{0}. \tag{4.3.1}$$

Fig.4.6 shows that in this limit the average flow due to a carpet near a solid boundary decays rapidly as $1/R^3$, while near a free surface it decays noticeably more slowly, as $1/R$.

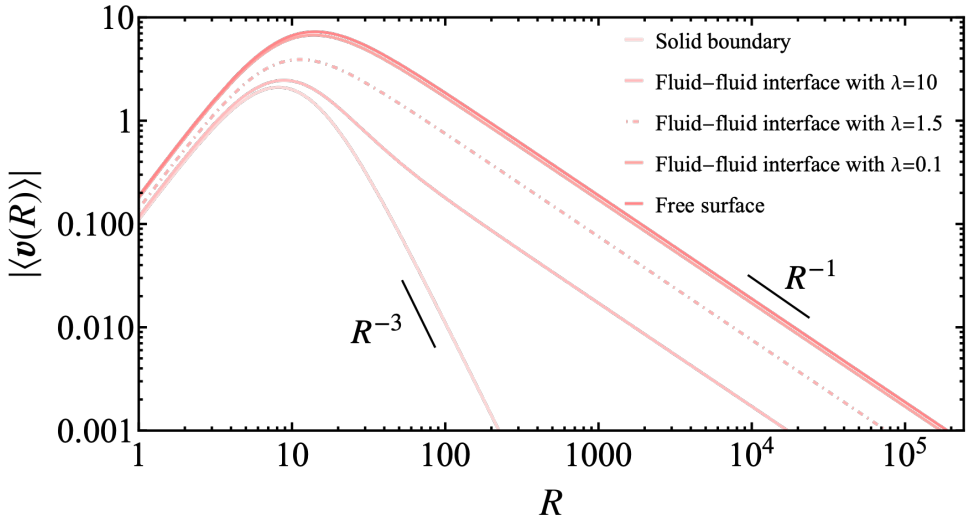

Figure 4.6: Absolute value of average flow produced by an active carpet for $h = 1\,\mu m$, $n = 0.1\,\mu m^{-2}$, $\kappa = 30\,\mu m^3/s$ near five different interfaces directly above the carpet, at $z = 10\,\mu m$, as a function of the carpet size R.

4.3.1 Active fluctuations

Importantly, even if the average flow generated by the microswimmers is equal to zero, the flow variance at any one time is not. Thus, the flows combined can lead to "active fluctuations" that push and pull on

particles near the carpet [45]. By definition, the variance-covariance matrix (or variance tensor) of the velocities is given by

$$\mathcal{K}_{v_i v_j} = \langle v_i v_j \rangle - \langle v_i \rangle \langle v_j \rangle \quad \text{where } i, j = x, y, z. \tag{4.3.2}$$

Nonetheless, as explained above, $\langle v_i \rangle = \langle v_j \rangle = 0$ for infinitely large carpets. Then, in general, the active fluctuations are defined by the elements of the variance tensor, which are determined analytically in a similar way as for the average flow in Eq.(4.2.1), as

$$\mathcal{V}_{ij}(\boldsymbol{r}) \equiv \langle v_i(\boldsymbol{r}) v_j(\boldsymbol{r}) \rangle = \int u_i(\boldsymbol{r}, \boldsymbol{r}_s, \boldsymbol{p}_s) u_j(\boldsymbol{r}, \boldsymbol{r}_s, \boldsymbol{p}_s) f(\boldsymbol{r}_s, \boldsymbol{p}_s) d\boldsymbol{r}_s d\boldsymbol{p}_s \tag{4.3.3}$$

Recalling from Sec.4.1 that $\boldsymbol{r}_s = (\rho_s \cos\varphi_s, \rho_s \sin\varphi_s, h)$, $\boldsymbol{p}_s = (\cos\phi_s, \sin\phi_s, 0)$ and that $f(\boldsymbol{r}_s, \boldsymbol{p}_s) = f(\rho_s, \varphi_s, \phi_s) = n/(2\pi)$ we explicitly can write the variance tensor as

$$\langle v_i(\boldsymbol{r}) v_j(\boldsymbol{r}) \rangle = \lim_{N_s, R \to \infty} \int_{\rho_s=0}^{\rho_s=R} \int_{\varphi_s=-\pi}^{\varphi_s=\pi} \int_{\phi_s=-\pi}^{\phi_s=\pi} u_i(\boldsymbol{r}, \rho_s, \varphi_s, \phi_s) u_j(\boldsymbol{r}, \rho_s, \varphi_s, \phi_s) \frac{n}{2\pi} \rho_s d\rho_s d\varphi_s d\phi_s \tag{4.3.4}$$

Physically, the results from integration will represent how deeply the active boundary can influence the passive bulk fluid.

Although integration is direct, the strength of these active fluctuations can be also found numerically by first computing the carpet flow distributions and then its moments (mean and variance) as a function of the distance from the boundary, z. As decribed in Sec.4.2.3, to simulate active carpet flows, a uniformly distributed carpet of N_s microswimmers with uniform surface density n is placed at $z_s = h$. Then the total flow $\boldsymbol{v}(\boldsymbol{r})$ is evaluated directly above the carpet at a tracer particle position $\boldsymbol{r} = (0, 0, z)$. To make an equivalent of averaging over swimmer positions and orientations, evaluation is repeated for a large ensemble of N_e independent carpet configurations, sampled as summarized in Fig.4.5.

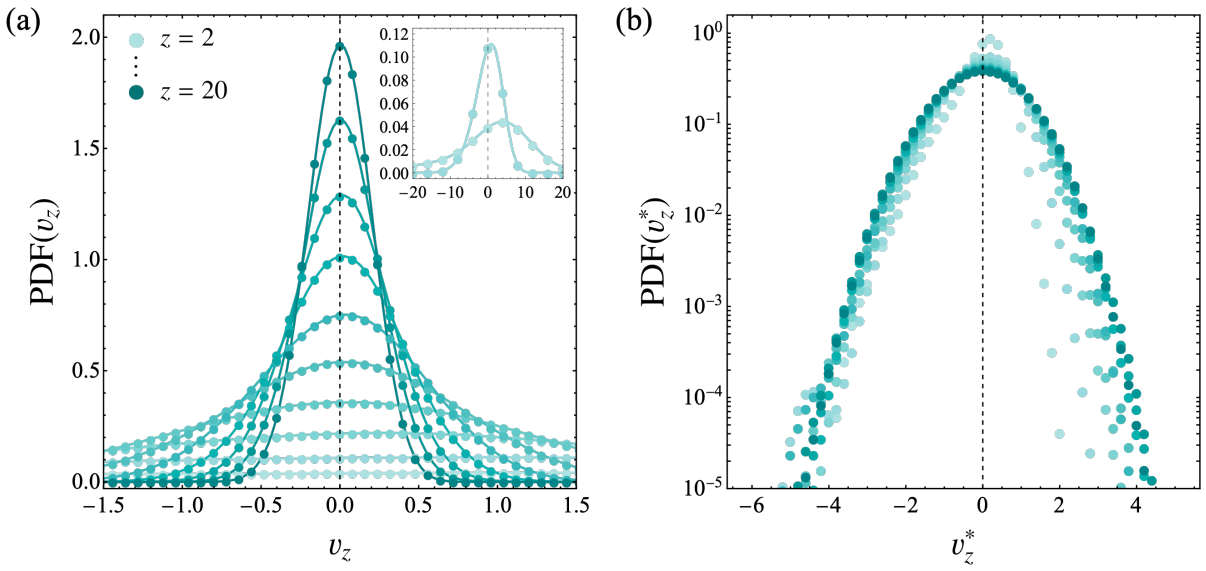

Figure 4.7: Probability distribution functions of the total vertical flow, PDF(v_z), due to an active carpet near a solid boundary.(a) PDF(v_z), of the carpet flow evaluated at different heights z. Inset shows the PDF for $z = 2\,\mu m$ and $z = 4\,\mu m$.(b) Normalized PDF(v_z^*), for the different heights z, where $v_z^* = v_z/\sqrt{\langle v_z^2 \rangle}$.

Fig.4.7 shows the probability distribution function of the vertical flow, PDF(v_z), due to an active carpet near a solid boundary for different heights $z = 2, \ldots, 20\,\mu m$ for $n = 0.1\,\mu m^{-2}$, $N_s = 10^5$ microswimmers, $\kappa = 30\,\mu m^3/s$, $h = 1\,\mu m$ and for $N_e = 10^4$ independent carpet ensembles. As evident from the inset in Fig.4.7(a), the distributions PDF(v_z) are not purely Gaussian, since they feature skewness and kurtosis, especially for low z values. Nonetheless, they still obey to the central limit theorem because the variance is finite for $z > 0$. Additionally, note they decay with z so far away from the carpet, the distributions are more Gaussian. To see the dependence of the variance on z more clearly, we now integrate Eq.(4.3.4).

In what follows, as in Sec.4.2.1, using the approximation for $z \gg h$ from Eq.(4.2.4) for the individual flows I compute Eq.(4.3.4) analytically and present the obtained results for the horizontal variance, $\langle v_x^2 \rangle = \langle v_x^2 \rangle$ (due to symmetry) and the vertical variance, $\langle v_z^2 \rangle$ (the off-diagonal elements vanish, so the only non-trivial results are $i = j$ in Eq.(4.3.4)), directly above the carpet, i.e., evaluated at position $\boldsymbol{r} = (0, 0, z)$, when the interface is a solid boundary, a free surface, and a fluid-fluid interface with viscosities ratio λ:

- For a solid boundary, the variance components are

$$\langle v_\alpha^2(z) \rangle = \frac{21\pi n h^2 \kappa^2}{4z^4} \quad \text{with } \alpha = x, y \tag{4.3.5}$$

$$\langle v_z^2(z) \rangle = \frac{45\pi n h^2 \kappa^2}{2z^4} \tag{4.3.6}$$

- For a free surface, the variance components are

$$\langle v_\alpha^2(z) \rangle = \frac{11\pi n \kappa^2}{16z^2} \quad \text{with } \alpha = x, y \tag{4.3.7}$$

$$\langle v_z^2(z) \rangle = \frac{9\pi n \kappa^2}{8z^2} \tag{4.3.8}$$

- For a fluid-fluid interface with viscosities ratio λ, the variance components are

$$\langle v_\alpha^2(z) \rangle = \frac{\pi n \kappa^2 \left(84h^2\lambda^2 + 40h\lambda z + 11z^2\right)}{16(\lambda+1)^2 z^4} \quad \text{with } \alpha = x, y \tag{4.3.9}$$

$$\langle v_z^2(z) \rangle = \frac{9\pi n \kappa^2 \left(20h^2\lambda^2 + 8h\lambda z + z^2\right)}{8(\lambda+1)^2 z^4} \tag{4.3.10}$$

  Note that in the limit $\lambda \to \infty$ one recovers Eq.(4.3.5) and Eq.(4.3.6), while for $\lambda = 0$, one recovers Eq.(4.3.7) and Eq.(4.3.8).

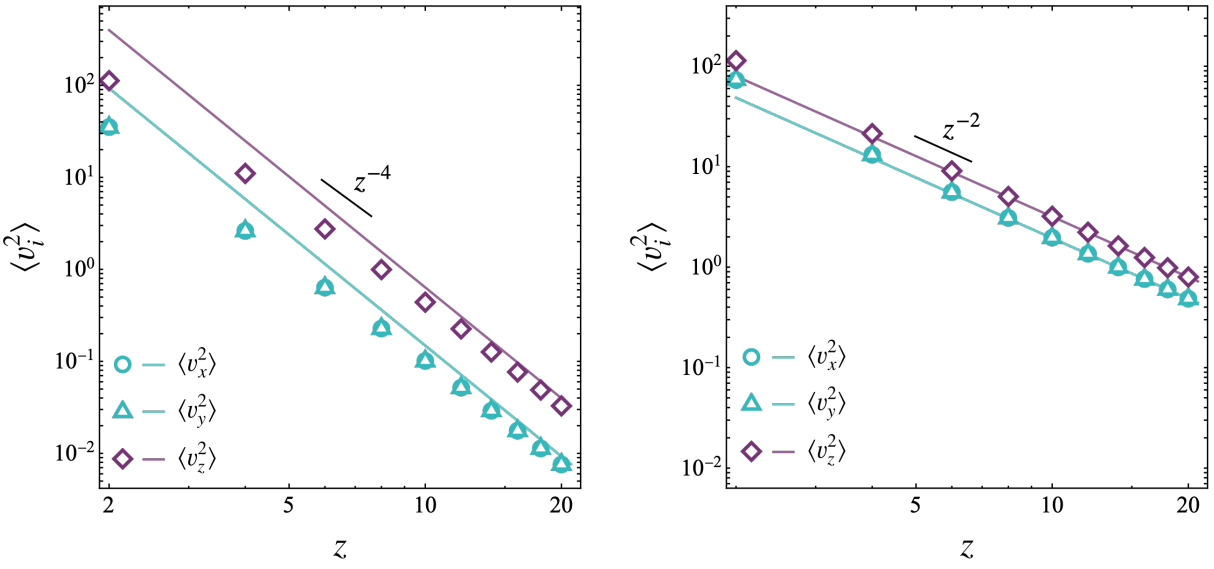

Figure 4.8: Variances of the flow distributions,$\langle v_i^2 \rangle$, corresponding to the strength of the active fluctuations in thee three directions $i = x, y, z$, as function of the distance z from an active carpet near a solid boundary (left panel) and a free surface (right panel), where $h = 1\,\mu m$, $n = 0.1\,\mu m^{-2}$, $\kappa = 30\,\mu m^3/s$.

Fig.4.8 shows the variances of the flow distributions due to active carpets near a solid boundary and an active carpet near free surface for different heights z, where solid lines are the obtained theoretical variances in the approximation $z \gg h$, Eq.(4.3.5), Eq.(4.3.7) and Eq.(4.3.6), Eq.(4.3.8) and symbols come from simulations performed for the same parameters as above, in Fig.4.7. As first seen in Fig.4.7 for the

case of a solid boundary, the mean flow of the distribution vanishes or is really small, however its width is finite and decays with distance from the surface, so the active fluctuations are stronger closer to the carpet, as seen now, and most important, they are anisotropic, so vertical fluctuations are stronger than the horizontal ones. Note that for $z \sim h$, the simulations points don't match the theoretical predictions; this is because in the simulations we use the total flow, which is not approximated as in the theory. Nonetheless, further away from the carpet they are in agreement, which is where the theory offers a good approximation. Similarly occurs for an active carpet near a free surface (see [41] for more detail given by Aguayo et al., where they analyze the active fluctuations due to active carpets near a free surface).

4.3.2 Tracer particle dynamics and space-dependent diffusivity

To this point we haven't introduced any dynamics on the active carpets. Instead, flows have only been sampled and statistics have been made over them. Nonetheless, this allowed to make a characterization of the carpet-induced active fluctuations. To understand how these active fluctuations act over tracer particles and may lead to particle diffusion, it is necessary to explain how exactly they vary over time. As reviewed in Chap.3, natural systems such as bacteria (or artificial self-propolled particles) swimming over a surface are dynamic. They move and reorient according to well-known stochastic processes generating flows that change dynamically by combining their self-propulsion dynamics (Chap.3) with hydrodynamics (Chap.2) so these perturbations are transmitted to their surrounding accordingly. Indeed, as I will show in the following, a tracer particle that is advected by these flows will trace a path that is eventually diffusive, not because of Brownian motion, but due to the active fluctuations being correlated in time: they have a memory time that is based on the history of the active carpet configuration.

Consider a (point) tracer particle with time-dependent position $\boldsymbol{r}(t) = (x(t), y(t), z(t))$ that is initially fixed above the active carpet at an initial position $\boldsymbol{r}_0 = (0, 0, z_0)$, not subjected to Brownian thermal fluctuations, but only to fluctuating flows generated by the active carpet. The tracer equation of motion is then given by

$$\frac{d\boldsymbol{r}(t)}{dt} = \boldsymbol{v}(\boldsymbol{r}(t), t) = \sum_{i=1}^{N_s} \boldsymbol{u}(\boldsymbol{r}(t), \boldsymbol{r}_{s,i}(t), \boldsymbol{p}_{s,i}(t)) \tag{4.3.11}$$

where t is the time, $\boldsymbol{v}(\boldsymbol{r}(t), t)$ is the total flow due to a carpet configuration at instant t, and $\boldsymbol{r}_{s,i}(t)$ and $\boldsymbol{p}_{s,i}(t)$ are now time-varying microswimmer positions and orientations. Then, to really solve tracer dynamics we must also solve the microswimmer's dynamics. Fig.4.9 shows a representation of how the active carpet displaces a tracer particle by transmiting the active flow fluctuations through the medium.

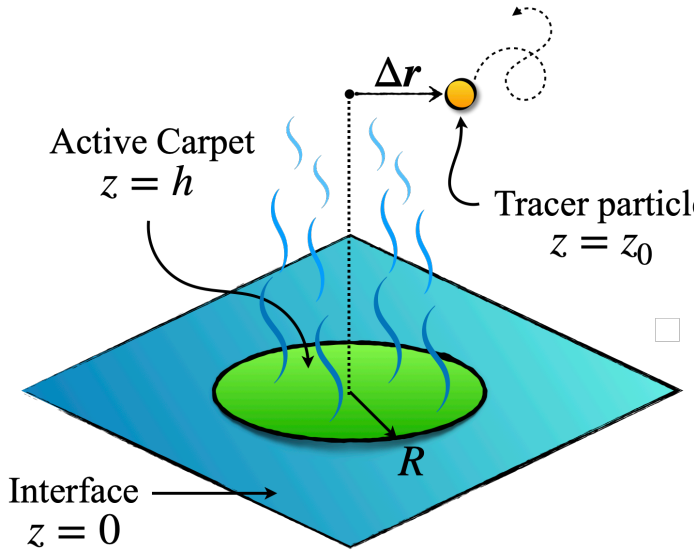

Figure 4.9: Summary scheme of microswimmer dynamics

As reviewed in Sec.3.2, single microswimmer dynamics are dominated by rotational diffusion as self-propel with speed v_s in a directed manner with persistence time $\tau_p = 1/D_R$ at short times and diffuse enhancedly at long times because of activity. An active carpet made of moving microswimmers (or moving

actuators in general) that exert known forces on their surroundings will feature the persistence time,τ_p, as time scale. Furthermore, will also feature an advection time

$$\tau_u = z/v_s \tag{4.3.12}$$

which is defined as the time taken by the microswimmers to move underneath a tracer particle. Since the speed v_s is directly related to the strength of the hydrodynamic flow produced by the microswimmers, this time can be interpreted as time for the active fluctuations to advect or induce long-range entrainment on the tracer particle [117]. The latter can make solving the dynamics of tracer particles more complex in general, but for slow microswimmers the decorrelation of the carpet memory is primarily controlled by the rotational diffusion, since $\tau_p \ll \tau_u$ for small v_s. In other words, in this regime, tracer particles will still be subjected to active fluctuations, however, their time scale of motion will be more (if not only) like the time scale proper of the motion of the microswimmers themselves. From this, one might state that tracer particles inherit the microswimmer's memory time.

Consider the tracer displacement, $\Delta\boldsymbol{r}(t) = \boldsymbol{r}(t) - \boldsymbol{r}_0$, as shown in Fig.4.9. In the slow micro-swimmer regime, where the whole system is dominated by only one time scale, the motion of the tracer particles can be solved analytically by considering small displacements of the tracer from its initial position, $|\Delta\boldsymbol{r}| \ll |\boldsymbol{r}_0|$. Then, the total active carpet flow can be expanded around $\boldsymbol{r}_0$ such that the tracer equation of motion is

$$\frac{d\boldsymbol{r}(t)}{dt} = \frac{d\Delta\boldsymbol{r}(t)}{dt} \approx \boldsymbol{v}(\boldsymbol{r}_0, t) + \mathcal{O}\left(\frac{|\Delta\boldsymbol{r}|}{r_0}\right) \tag{4.3.13}$$

where higher-order terms can expanded as power series in $1/z_0$ [117]. Consequently, the mean square displacement (MSD) can be determined locally as

$$\langle \Delta r_i \Delta r_j \rangle = \left\langle \int_0^t v_i(\boldsymbol{r}_0, t')dt' \int_0^t v_j(\boldsymbol{r}_0, t'')dt'' \right\rangle = \int_0^t \int_0^t \langle v_i(\boldsymbol{r}_0, t') v_j(\boldsymbol{r}_0, t'')\rangle dt' dt'' \tag{4.3.14}$$

where the assumption of small tracer displacements requires that

$$\langle \Delta\boldsymbol{r}^2 \rangle \ll \boldsymbol{r}_0^2 \tag{4.3.15}$$

From Eq.(4.3.14) we identify the time velocity correlation function (VCF) of the total flow at position $\boldsymbol{r}_0$, that is

$$\langle v_i(\boldsymbol{r}_0, t') v_j(\boldsymbol{r}_0, t'')\rangle = \langle v_i(\boldsymbol{r}_0, 0) v_j(\boldsymbol{r}_0, 0)\rangle \exp\left(-\frac{|t' - t''|}{\tau_p}\right) \tag{4.3.16}$$

From this result one can afirm that the decorrelation or memory time of tracer particles motion is the persistence time, τ_p. Inserting Eq.(4.3.16) into Eq.(4.3.14) we have

$$\langle \Delta r_i \Delta r_j \rangle = \langle v_i(\boldsymbol{r}_0) v_j(\boldsymbol{r}_0)\rangle \int_0^t \int_0^t \exp\left(-\frac{|t' - t''|}{\tau_p}\right) dt' dt'' \tag{4.3.17}$$

Thus, after integration, the obtained MSD is

$$\langle \Delta r_i \Delta r_j \rangle = 2\mathcal{V}_{ij}(\boldsymbol{r}_0)\tau_p \left(t + \tau_p(e^{-t/\tau_p} - 1)\right) \tag{4.3.18}$$

where $\mathcal{V}_{ij}(\boldsymbol{r}_0) = \langle v_i(\boldsymbol{r}_0) v_j(\boldsymbol{r}_0)\rangle$. This result is the equivalent to the one obtained for active Brownian particles in Sec.3.2, which captures both the short-term ballistic motion and an active diffusion after long times, but now due to the active fluctuations induced by the active carpet at position $\boldsymbol{r}_0$. Indeed, it can be shown that

$$\langle \Delta r_i \Delta r_j \rangle = \begin{cases} \langle v_i v_j \rangle t^2, & \text{if } t \ll \tau_p \\ 2\langle v_i v_j \rangle \tau_p t, & \text{if } t \gg \tau_p \end{cases} \tag{4.3.19}$$

Then for long times, $t/\tau_p \gg 1$, we may now define a local effective diffusion coefficient for the tracer particles as

$$D_{ij}^{\mathrm{s}} = \lim_{t\to\infty} \frac{1}{2t} \langle \Delta r_i \Delta r_j \rangle = \langle v_i v_j \rangle \tau_p \tag{4.3.20}$$

More simply, since only $i = j$ results in non-trivial fluctuations, we define the local space-dependent diffusivity as

$$D_i^{\mathrm{s}} \equiv \lim_{t\to\infty} \frac{1}{2t} \langle \Delta r_i^2 \rangle = \langle v_i^2 \rangle \tau_p \tag{4.3.21}$$

The analytical result for the local diffusivity of a tracer particle at height z above an active carpet near an interface in the regime of small tracer displacements is quite direct from the results obtained in Sec.4.3.1. For instance, if the interface is a solid boundary, the local vertical diffusivity is

$$D_z(z) = \langle v_z^2 \rangle \tau_p = \frac{45\pi n h^2 \kappa^2}{2z^4} \tau_p \tag{4.3.22}$$

Now, this result allows one to analyze the consequences of the assumption of small displacements. Using Eq.(4.3.15), we rewrite this condition as

$$2D_z t \ll z^2 \tag{4.3.23}$$

Then, we can rearrange this for a temporal condition

$$\frac{t}{\tau_p} \ll \frac{z^6}{45\pi n h^2 \kappa^2 \tau_p^2} \tag{4.3.24}$$

As shown above, for the tracer particle's motion to be diffusive, we also require that $t/\tau_p \gg 1$, so the theory is only expected to hold when the time scale of diffusive transport, t, is slow compared to the time scale of the active fluctuations themselves, τ_p. Thus, from Eq.(4.3.24) we get a spatial condition that dictates that the latter occurs far from the surface, where

$$z \gg \left(45\pi n h^2 \kappa^2 \tau_p^2\right)^{1/6} \tag{4.3.25}$$

An equivalent condition can be found for other interfaces (and actuator) types.

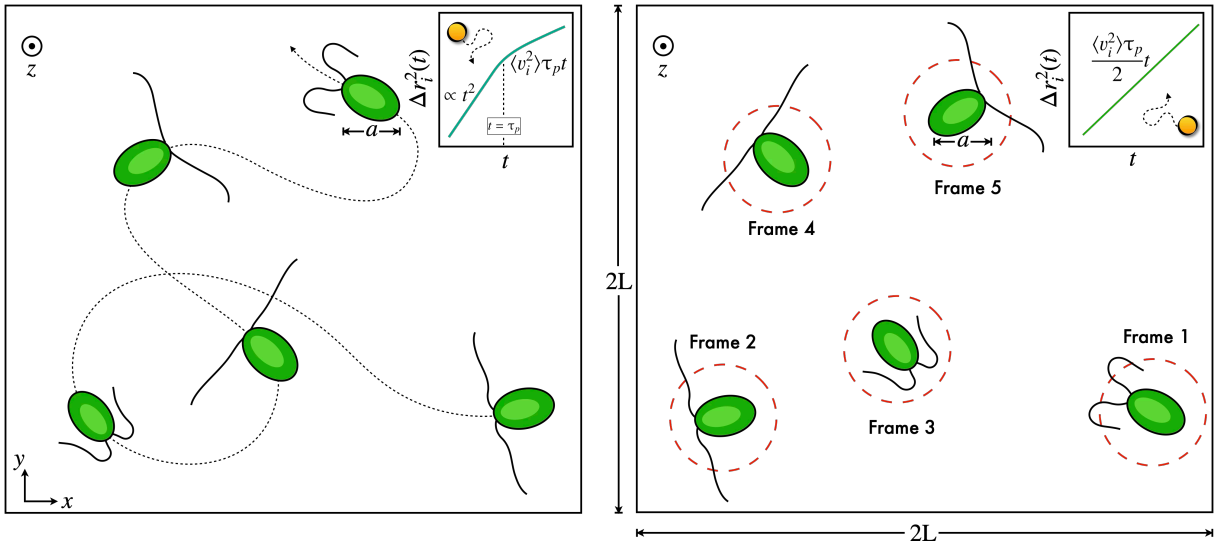

Figure 4.10: Scheme of microswimmer (green) dynamics in an $2L \times 2L$ active carpet indicating which kind of motion induces in surrounding tracer particles (orange). In the left panel, a microswimmer follows a continous path, changing its position and orientation accordingly to ABP dynamics, with persistence time τ_p. The inset shows the MSD of a tracer particle that features the same kind of motion as the microswimmer, transitioning from ballistic to diffusive motion, with local diffusivity $\langle v_i^2 \rangle \tau_p$. The right panel shows a microswimmer that does not follow any path, but change position and orientation randomly each time the carpet ensemble (or frame, as presented here) updates. The inset shows the MSD of a tracer particle that features purely diffusive motion with local diffusivity $\langle v_i^2 \rangle \tau_p / 2$.

A different approach can be made to only focus on the effects of the active carpet on tracer particles at long times, $t/\tau_p \gg 1$ [41]. For this, suppose that the active fluctuations flows are now uncorrelated in time, so as time passes, each flow is generated by a carpet ensemble that is different from the previous one, with microswimmers having randomly sampled positions and orientations each time.

Following this approach, the MSD can be defined as follows. Consider $t', t'' \in [0, t]$ as two consecutives discrete time instants, where the time interval $[0, t]$ can be partioned to $\tilde{n}$ subintervals of equal duration $\Delta t' = \Delta t'' = \Delta t = t/\tilde{n}$. Then, the MSD of a tracer particle subjected to the discrete carpet time

evolution can be approximated as the finite sum

$$\langle \Delta r_i \Delta r_j \rangle = \sum_{t'=0}^{\tilde{n}\Delta t} \sum_{t''=0}^{\tilde{n}\Delta t} \langle v_i(\boldsymbol{r}_0, t') v_j(\boldsymbol{r}_0, t'') \rangle \Delta t' \Delta t'' \tag{4.3.26}$$

where now the VCF indicates an accordingly discrete decorrelation betwen time instants, such that

$$\langle v_i(\boldsymbol{r}_0, t') v_j(\boldsymbol{r}_0, t'') \rangle = \langle v_i(\boldsymbol{r}_0, 0) v_j(\boldsymbol{r}_0, 0) \rangle \delta_{t't''} \tag{4.3.27}$$

Thus, the MSD is given by

$$\langle \Delta r_i \Delta r_j \rangle = \langle v_i(\boldsymbol{r}_0) v_j(\boldsymbol{r}_0) \rangle \sum_{t'=0}^{\tilde{n}\Delta t} \sum_{t''=0}^{\tilde{n}\Delta t} \delta_{t't''} \Delta t' \Delta t'' = \langle v_i(\boldsymbol{r}_0) v_j(\boldsymbol{r}_0) \rangle \tilde{n} \Delta t \Delta t = \langle v_i(\boldsymbol{r}_0) v_j(\boldsymbol{r}_0) \rangle t \Delta t \tag{4.3.28}$$

Now, to correctly describe the carpet-induced diffusion, the time subinterval must match the persistence time, $\Delta t = \tau_p$, so that it is equivalent to the correlated "physically correct" carpet case

$$\langle \Delta r_i \Delta r_j \rangle = \langle v_i(\boldsymbol{r}_0) v_j(\boldsymbol{r}_0) \rangle \tau_p t \tag{4.3.29}$$

Note that this result indicates that in this case there is no such thing as a ballistic regime for the tracer particle motion. Instead, the particle diffuses at all times due to the same physical reasons stated before, but with a diffusion constant different just by a factor. Indeed, one again can define the local diffusion constant for the tracer particle as

$$D_{ij}^s = \lim_{t \to \infty} \frac{1}{2t} \langle \Delta r_i \Delta r_j \rangle = \frac{1}{2} \langle v_i v_j \rangle \tau_p \tag{4.3.30}$$

which for $i = j$ writes

$$D_i^s \equiv \lim_{t \to \infty} \frac{1}{2t} \langle \Delta r_i^2 \rangle = \frac{1}{2} \langle v_i^2 \rangle \tau_p \tag{4.3.31}$$

This result can be analized as above to find the local diffusivity for tracer particles above different spatial configurations (actuators and interfaces). Importantly, this approach is especially suitable to perform numerical simulations for two reasons: first, one does not have to solve each microswimmer dynamics, but instead just update the whole carpet randomly, and second, since we are interested precisely in tracer particle diffusion, not waiting for microswimmers to become diffusive and still have a system with equivalent physical properties to work with saves computation time. That said, any tracer dynamics calculation is performed using this active carpet dynamics.

Using the small displacements relation from Eq.(4.3.23), we can write the spatial condition from Eq.(4.3.25) under this approach, which is the one used further below to estimate how far from the interface the theory holds. Then, if the interface is a solid boundary we obtain that

$$z \gg \left(\frac{45 \pi n h^2 \kappa^2 \tau_p^2}{2} \right)^{1/6} \tag{4.3.32}$$

An estimation can be done by inserting some typical numbers on the condition. For $n = 0.1\,\mu m^{-2}$, $h = 1\,\mu m$, $\kappa = 30\,\mu m^3/s$, $\tau_p = 0.13\,s$ (see Sec.3.3), we have that $z \gg 2.18\,\mu m$. Under this condition we are sure that we measure the local diffusivity $D(z)$ with small variations in z.

Fig.4.10 summarizes the two approaches to solve microswimmer dynamics and tracer particle diffusion due to an active carpet.

4.3.3 Simulation of tracer particle dynamics

To perform simulations of tracer particle dynamics one must simply solve Eq.(4.3.11). Recalling the tracer position, $\boldsymbol{r}(t) = (x(t), y(t), z(t))$, the independent equations of motion for each coordinate write

$$\frac{dx(t)}{dt} = \sum_{j=1}^{N_s} u_x(\boldsymbol{r}(t), \boldsymbol{r}_{s,j}(t), \boldsymbol{p}_{s,j}(t)) \tag{4.3.33}$$

$$\frac{dy(t)}{dt} = \sum_{j=1}^{N_s} u_y(\boldsymbol{r}(t), \boldsymbol{r}_{s,j}(t), \boldsymbol{p}_{s,j}(t)) \tag{4.3.34}$$

$$\frac{dz(t)}{dt} = \sum_{j=1}^{N_s} u_z(\boldsymbol{r}(t), \boldsymbol{r}_{s,j}(t), \boldsymbol{p}_{s,j}(t)) \tag{4.3.35}$$

with initial conditions $x(0) = y(0) = 0$ and $z(0) = z_0$. Note that there are no thermal fluctuations nor short-range interactions that can affect the tracer's motion, this only for the trajectories to feature the flow fluctuations effects whithout any bias. A more complex case was explored recently in [41], where Aguayo et al. explored tracer dynamics with a short-range Morse interaction to characterize tracer particle aggregation.

We use the method of finite differences to approximate the continous-time solution $[x(t), y(t), z(t)]$ by the discrete-time sequence $[x(t_i), y(t_i), z(t_i)] \approx [x_i, y_i, z_i]$ evaluated at time steps $t_i = i\Delta t$, where Δt is a sufficiently small time step (usually $\Delta t = 10^{-3}$) in a Euler integration scheme, such that we now solve

$$x_i = x_{i-1} + \sum_{j=1}^{N_s} u_x(\boldsymbol{r}_{i-1}, \boldsymbol{r}_{s,j}^{i-1}, \boldsymbol{p}_{s,j}^{i-1})\Delta t \tag{4.3.36}$$

$$y_i = y_{i-1} + \sum_{j=1}^{N_s} u_y(\boldsymbol{r}_{i-1}, \boldsymbol{r}_{s,j}^{i-1}, \boldsymbol{p}_{s,j}^{i-1})\Delta t \tag{4.3.37}$$

$$z_i = z_{i-1} + \sum_{j=1}^{N_s} u_z(\boldsymbol{r}_{i-1}, \boldsymbol{r}_{s,j}^{i-1}, \boldsymbol{p}_{s,j}^{i-1})\Delta t \tag{4.3.38}$$

To compute the fluctuations flows in the sum on the RHS of equations above the carpet is sampled as described in Sec.4.2.3, so an initial carpet configuration ($i = 0$) is sampled with total flow

$$\sum_{j=1}^{N_s} \boldsymbol{u}(\boldsymbol{r}_0, \boldsymbol{r}_{s,j}^0, \boldsymbol{p}_{s,j}^0) = \boldsymbol{u}(\boldsymbol{r}_0, \boldsymbol{r}_{s,1}^0, \boldsymbol{p}_{s,1}^0) + \cdots + \boldsymbol{u}(\boldsymbol{r}_0, \boldsymbol{r}_{s,N_s}^0, \boldsymbol{p}_{s,N_s}^0) \tag{4.3.39}$$

and then this is updated to a new different independent configuration, as shown in Fig.4.11.

In this chapter I presented the theory and numerical aspects of modeling active carpets near an interface. I started by giving a definition of an active carpet. Then, I continued by giving analytical definitions and numerical methods to calculate the average fluxes generated by finite active carpets. Finally, I described the out-of-equilibrium transport properties of sufficiently large active carpets. In the next chapter, I use what is described in this chapter to explore the effects of confinement on the action of active carpets, which is explored for the first time in this thesis work.

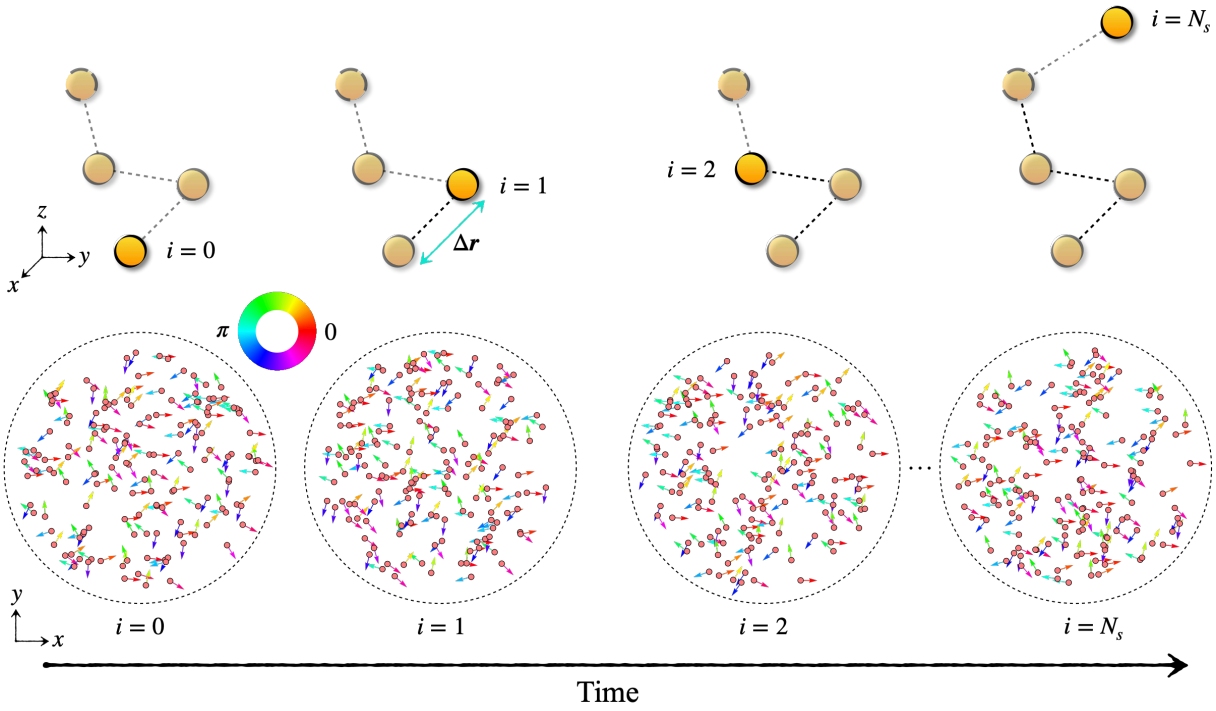

Figure 4.11: Scheme of how tracer dynamics are solved by sampling carpets each time step in the simulation. The bottom row shows the carpet sampling on a disk of radius R in the plane $z = h$, where solid disks (pink) are microswimmer positions and arrows represent their orientations with their angle following the color wheel code. The top row shows a representative trajectory of a tracer particle, which is at its initial position for $i = 0$ and displaces at distance $\Delta \boldsymbol{r}$ in any direction each time the carpet sample is updated and the flows summed, and that is repeated till $i = N_s$.

Chapter 5

Active carpets in confined environments

In the previous chapters I described all the theory and numerical methods that allow us to understand the hydrodynamics of micro-swimmers (Chapter 2), their microscopic Newtonian dynamics (Chapter 3) and the recent theory of active carpets near an interface (Chapter 4). In this chapter we use the above to model active carpets in a confined environment called floating film (sometimes just named film in the following). This environment consists of two interfaces: the first, a fluid-fluid interface located below the carpet, the second, an air-liquid interface or free surface, located above it. Fig.5.1 graphically resumes the physical system explored in this work.

First, I present the low Reynolds number hydrodynamic model for micro-swimmers confined in the floating film. Second, I recall some definitions on the active carpet theory and introduce a new one. Third, I briefly review the basic aspects to perform numerical simulations with active carpets and tracer particle dynamics, and set all the parameters used in this work.

Based on the above, I present the main results of this thesis work, starting with the analytical calculation of the velocity field produced by a single micro-swimmer inside the film, and continue with employing the active carpet theory to compute the active fluctuations, which I then characterize in detail by analytical calculations and by numerical simulations. Next, I explore the role of confinement on these fluctuations, followed by a quantitative analysis on the capacities of an active carpet, when confined, to generate large-scale coherent flow patterns and vorticity fields.

5.1 Hydrodynamics of a single microswimmer within a floating film

We model the flow field of a single flagellated microswimmer moving in a homogeneous fluid of viscosity μ_1, confined between two non-deforming boundaries [118, 4]. Here, the top boundary is a free-surface, whereas the bottom is a fluid-fluid interface, where below it there is a second fluid of viscosity μ_2. The ratio between both fluid viscosities is denoted as $\lambda = \mu_2/\mu_1$. The distance between both interfaces is H and is referred to as the film thickness, as depicted in Fig.5.1.

The fluid motion driven by microscopic swimmers is described in the low Reynolds number regime, in which viscous forces dominate the momentum balance (see Sec.2.1) [63, 64]. For a point force $\boldsymbol{F} = \boldsymbol{f}\delta(\boldsymbol{r} - \boldsymbol{r}_s)$ acting at position $\boldsymbol{r}_s = (x_s, y_s, z_s)$ on a stationary fluid of dynamic viscosity μ, the hydrodynamics flow is governed by the incompressible Stokes equations [61],

$$\nabla p(\boldsymbol{r}) - \mu\nabla^2\boldsymbol{u}(\boldsymbol{r}) = \boldsymbol{F}, \tag{5.1.1a}$$

$$\nabla \cdot \boldsymbol{u}(\boldsymbol{r}) = 0, \tag{5.1.1b}$$

where $\boldsymbol{u}(\boldsymbol{r})$ and $p(\boldsymbol{r})$ are the fluid velocity and pressure fields at position $\boldsymbol{r} = (x, y, z)$, respectively. In the absence of lateral boundaries, the solution of Eqs.(5.1.1) is the well-known Stokeslet [65, 66, 67]

$$\boldsymbol{u}(\boldsymbol{r}, \boldsymbol{r}_s) = \frac{\mathcal{G}_{ij}(\boldsymbol{r}, \boldsymbol{r}_s) \cdot \boldsymbol{F}}{8\pi\mu}, \; \mathcal{G}_{ij}(\boldsymbol{r}, \boldsymbol{r}_s) = \left(\frac{\delta_{ij}}{|\boldsymbol{d}|} + \frac{d_i d_j}{|\boldsymbol{d}|^3}\right), \tag{5.1.2}$$

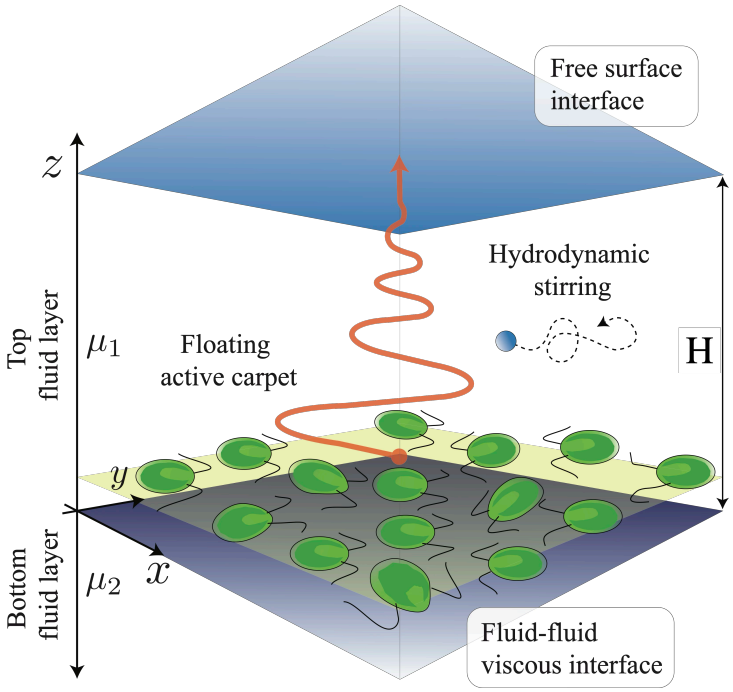

Figure 5.1: Scheme of a confined *Active Carpet* (yellow) between two fluid interfaces, at the top an air-water interface and at the bottom a fluid-fluid interface. The active carpet is formed by microswimmers living at a fixed distance σ from the bottom fluid-fluid interface (in green). The microswimmers generate hydrodynamic fluctuations in the confined fluid (orange arrow) that stir fluid parcels and suspended matter in within the layer.

where $\boldsymbol{d} = \boldsymbol{r} - \boldsymbol{r}_s$ is the relative position between the swimmer and the surrounding fluid (see Sec.2.2). Derivatives of the Stokeslet are also solutions [117, 119, 120]. For swimming microorganisms, where the thrust and the drag force balance, the Stresslet is the first dominant term in the multipole expansion to describe their far-field flow (see Sec.2.3) [68].

Here, however, we must include the boundary conditions to fulfill the system's confinement (see Sec.2.4). Following [4], we construct the first approximation to the image system for the flow field produced by a microswimmer confined between a fluid-fluid interface and a free surface interface, as described in Fig.5.2.

The Stokes equations for a point force acting on fluid 1 are

$$-\nabla p^{(1)} + \mu_1 \nabla^2 \boldsymbol{u}^{(1)} + \boldsymbol{F} = 0, \tag{5.1.3a}$$

$$\nabla \cdot \boldsymbol{u}^{(1)} = 0, \tag{5.1.3b}$$

while for fluid 2 are

$$-\nabla p^{(2)} + \mu_2 \nabla^2 \boldsymbol{u}^{(2)} = 0, \tag{5.1.4a}$$

$$\nabla \cdot \boldsymbol{u}^{(2)} = 0. \tag{5.1.4b}$$

The velocity field of both fluids must satisfy the following boundary conditions at the fluid-fluid interface [118],

$$u_\alpha{}^{(1)} = u_\alpha{}^{(2)}, \text{ at } z = 0 \tag{5.1.5a}$$

$$u_z^{(1)} = u_z^{(2)} = 0, \tag{5.1.5b}$$

$$\mu_1 \left(\frac{\partial u_\alpha^{(1)}}{\partial z} + \frac{\partial u_z^{(1)}}{\partial \alpha} \right) = \mu_2 \left(\frac{\partial u_\alpha^{(2)}}{\partial z} + \frac{\partial u_z^{(2)}}{\partial \alpha} \right) \text{ at } z = 0, \tag{5.1.5c}$$

where $\alpha = x, y$, and at the free surface interface,

$$u_z^{(1)} = 0, \text{ at } z = \mathrm{H}, \tag{5.1.6a}$$

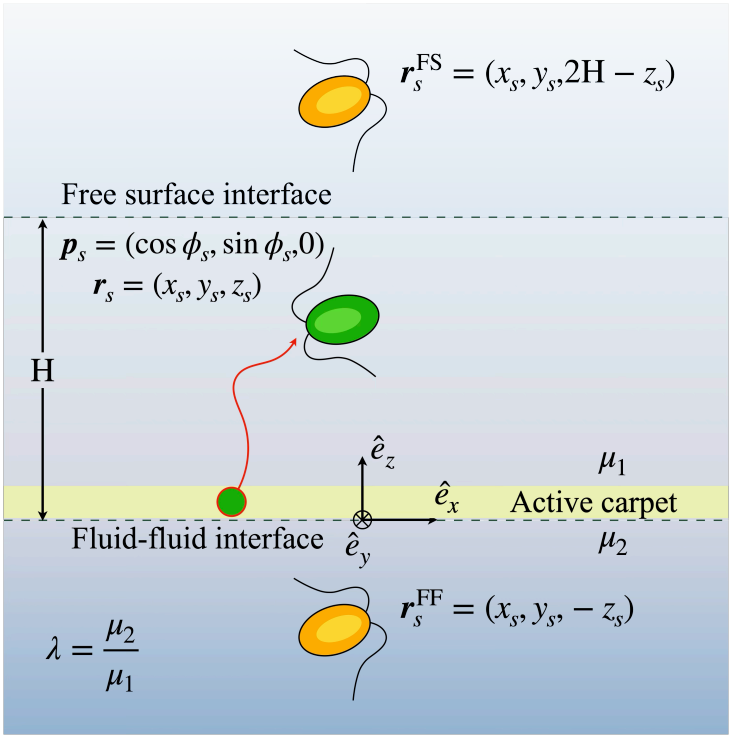

Figure 5.2: Conceptual model for a single microswimmer confined between the free surface interface (top) and the fluid-fluid interface (bottom). A microorganism swims in the x-y plane at $z = \sigma$ (in green), producing two images (in yellow) located at $\mathbf{r}_s^{\mathrm{FS}}$ and $\mathbf{r}_s^{\mathrm{FF}}$ respectively.

$$\frac{\partial u_\alpha^{(1)}}{\partial z} + \frac{\partial u_z^{(1)}}{\partial \alpha} = 0, \text{ at } z = \mathrm{H}. \tag{5.1.6b}$$

From solving Eqs.(5.1.3), Eqs.(5.1.4) and Eqs.(5.1.5), the image's system for a point force between two fluids of different viscosities leads to a generalization of the Blake tensor [118]:

$$\begin{aligned}\mathcal{A}_{ij}(\boldsymbol{r}) = &\left(\frac{1-\lambda}{1+\lambda}\delta_{j\alpha}\delta_{\alpha k} - \delta_{j3}\delta_{3k}\right)\mathcal{G}_{ik}(\boldsymbol{r}) \\ &+ \frac{2\lambda}{\lambda+1} z_s(\delta_{j\alpha}\delta_{\alpha k} - \delta_{j3}\delta_{3k})\frac{\partial}{\partial r_k}\left(\frac{z_s r_i}{r^3} + \mathcal{G}_{i3}(\boldsymbol{r})\right).\end{aligned} \tag{5.1.7}$$

Notice that for $\lambda = 0$, we recover the image flow field of a point force close to a free surface,

$$\mathcal{F}_{ij}(\boldsymbol{r}) = \mathcal{M}_{jk}\mathcal{G}_{ik}(\boldsymbol{r}), \tag{5.1.8}$$

where $\mathcal{M}_{jk}$ is a mirror matrix, $\mathcal{M} = \mathrm{diag}(1, 1, -1)$. This image system corresponds to the one satisfying the boundary condition at $z = \mathrm{H}$.

Formally, a point force $\boldsymbol{F} = \boldsymbol{f}\delta(\boldsymbol{r} - \boldsymbol{r}_s)$ is acting at position $\boldsymbol{r}_s = (x_s, y_s, z_s)$. The image system to account for the fluid-fluid interface is constructed using the propagator tensor Eq.(5.1.7) for an image force located at position $\boldsymbol{r}_s^{\mathrm{FF}} = (x_s, y_s, -z_s)$. Whereas for the free surface interface, we set a mirror image using Eq.(5.1.8) at position $\boldsymbol{r}_s^{\mathrm{FS}} = (x_s, y_s, 2\mathrm{H} - z_s)$. The velocity field produced by a point force parallel to both interfaces is then given by

$$\begin{aligned}\boldsymbol{u}(\boldsymbol{r}, \boldsymbol{r}_s, \lambda, \mathrm{H}) = &\mathcal{G}(\boldsymbol{r}, \boldsymbol{r}_s)\cdot\boldsymbol{f}_\parallel \\ &+ (\mathcal{F}(\boldsymbol{r}, \boldsymbol{r}_s^{\mathrm{FS}}, \mathrm{H}) + \mathcal{A}(\boldsymbol{r}, \boldsymbol{r}_s^{\mathrm{FF}}, \lambda))\cdot\boldsymbol{f}_\parallel,\end{aligned}$$

where the second term is the full image system added to satisfy the induced hydrodynamic boundary conditions and $\boldsymbol{f}_\parallel = \boldsymbol{f}/(8\pi\mu_1)$ is the scaled force.

We can then measure the velocity field of a force dipole (see Sec.2.3) with orientation $\boldsymbol{p}_s$ as shown in Fig.5.2,

$$\boldsymbol{u}_D(\boldsymbol{r}, \boldsymbol{r}_s, \boldsymbol{p}_s) = \kappa\,(\boldsymbol{p}_s\cdot\nabla_s)[(\mathcal{G} + \mathcal{F} + \mathcal{A})\cdot\boldsymbol{p}_s]. \tag{5.1.9}$$

Here derivatives $\nabla_s = \partial/\partial \boldsymbol{r}_s$ are taken with respect to the microswimmer's position. The coefficient $\kappa = f_{\|}\sigma$ corresponds to the dipolar strength, which characterizes the hydrodynamic distortions of each microswimmer (see Sec.2.3) and sets the timescale of the biogenically driven flow, $\tau = \sigma^3/\kappa$, with σ the microswimmer body length, therefore, the film thickness scales as $H = n_{\mu_1}\sigma$ with the varying number n_{μ_1} and the carpet size is given by $L = n_{\text{carpet}}\sigma$ with a given number n_{carpet}. On the one hand when $\kappa > 0$, the microswimmer generates an extensile flow (pusher) similar to motile bacteria powered by a helical flagella bundle. On the other hand when $\kappa < 0$, the flow field is contractile (puller) similar to the flow generated by green microalgae *Chlamydomonas reinhardtii* [69].

Here, we utilize the leading-order image system to describe the far-field flow of a dipole microswimmer [4]. It is important to note that boundary conditions are only partially satisfied when two image flow fields are added to the hydrodynamic system. To mitigate this discrepancy, recursive images of the original images must be added. However, since the first images closely approximate the confined natural system under investigation, they encapsulate most of the relevant physics. Therefore, subsequent images will inevitably be farther removed from the system [9].

In nature, sharp vertical temperature gradients or the presence of natural and artificial oils can lead to abrupt changes in fluid viscosity, especially at the skin of surface waters [121]. Also, during blooms, planktonic microorganisms have been reported to increase the effective ambient viscosity, generating strong viscosity gradients with relative viscosities $1 \lesssim \lambda \lesssim 3$ at short distances [16]. Microorganisms in mammals' guts and tracts also swim in regions of high viscosity contrast or mucus, with some bacteria performing positive viscotaxis and some other strains performing negative viscotaxis among these regions [122, 123, 124]. Recent research has studied the microorganisms' optimal swimming behavior in viscosity gradients (viscotaxis), revealing divergent trends. In some cases, microorganisms prefer swimming in low-viscosity regions, while in others, they favor high-viscosity environments [125, 126, 122, 15, 127]. For instance, the *Chlamydomonas reinhardtii*, a type of phytoplankton, shows viscophobic behavior by accumulating in the region of lower viscosity $\lambda > 1$ [17].

In recent experiments, bacterial baths within microdroplets of water in oil ($\lambda < 1$) have been studied with different bacteria. In the case of magnetotactic bacteria, it was observed that they drive a vortex flow in the center of the microdroplet in the presence of strong external magnetic fields [25]; this was also corroborated with numerical simulations showing a fragile equilibrium between high bacterial concentrations, activity, confinement, and taxis [24]. In the case of a suspension of Escherichia coli, the bacterial bath generates hydrodynamic fluctuations that self-propel the microdroplet [128], or in the case of a double emulsion, the suspended particle at the core of the microdroplet is inherent to the microscopic parameters of the bacterial suspension, such as memory time and length scales [46].

5.2 Active carpets within a floating film

Our model considers a collection of dipole microswimmers constricted to move in the x-y plane at a fixed height $z_s = \sigma$, which corresponds to microswimmers moving above the viscosity interface forming the so-called *Active Carpet*, as sketched in Fig.5.1

As explained in detail in Chapter 4, the *Active Carpet* is constituted of a dense suspension of point-like microorganisms, each of them inhabiting this environment at positions $\boldsymbol{r}_s = (x_s, y_s, \sigma)$ and orientations $\boldsymbol{p}_s = (p_x, p_y, 0)$. We consider them in a stroboscopic diffusive regime [41, 45] such that all microswimmers are uniformly distributed in space and orientations in a 2D surface as time progresses (this is well summarized in Fig.4.10, Sec.4.3.2, where I described how to solve microswimmer dynamics in the active carpet). Each microorganism stirs and energizes the confined water film, driving a flow field given by Eq.(5.1.9). Here, we probe the biogenically driven flow at positions $\boldsymbol{r}_0 = (x_0, y_0, z_0)$, corresponding to a fluid parcel between the free surface and fluid-fluid interface. To find a far-field approximation for the collective flow drive by the Active Carpet, we performed a Taylor expansion for the flow field generated by a single microswimmer, such that $z_s = \epsilon z_0$ with $\epsilon \ll 1$ (see more details in Sec.4.2, where I explained this approximation, along with Fig.4.2 for a graphical demonstration). With this analytical expression, we can measure analytically different statistical properties of the collectively generated flow.

In Sec.4.2 I defined the average flow field due to an active carpet, which I recall now. The mean flow field averaged over a finite carpet of size R with microswimmer uniformly distributed in cylindrical

coordinates, ρ_s, θ_s and orientations ϕ_s is

$$\langle \boldsymbol{v}(\boldsymbol{r}) \rangle = \int \boldsymbol{u}(\boldsymbol{r}, \boldsymbol{r}_s, \boldsymbol{p_s})\, \mathcal{F}(\boldsymbol{r}_s, \boldsymbol{p_s})\, d\boldsymbol{r}_s d\boldsymbol{p_s}, \tag{5.2.1}$$

where $\mathcal{F} = n/2\pi > 0$ is a uniform distribution of swimmers for a carpet number density n and $\langle \cdot \rangle$ is the average over the collection of swimmers. Here $\boldsymbol{r_s} = (\rho_s \cos\theta_s, \rho_s \sin\theta_s, \sigma)$ is the swimmer's position and $\boldsymbol{p_s} = (\cos\phi_s, \sin\phi_s, 0)$ the swimmer's orientation, with $\phi_s, \theta_s \in [-\pi, \pi]$. The variance, which encapsulates what we call fluctuations (see Sec.4.3.1), governs the active diffusion process that tracer particles experience over the carpet where $i, j = x, y, z$ denote its components in Cartesian coordinates; its magnitude depends strongly on the geometry of the environment and can be computed analytically using the following expression for the variance tensor

$$\mathcal{V}_{ij} = \langle v_i v_j \rangle = \int u_i u_j \mathcal{F}\, d\boldsymbol{r}_s d\boldsymbol{p_s}. \tag{5.2.2}$$

In addition, we define the average vorticity field induced by the confined *Active Carpet* as

$$\langle \boldsymbol{\omega} \rangle = \langle \nabla \times \boldsymbol{v} \rangle = \int (\nabla \times \boldsymbol{u}) \mathcal{F}\, d\boldsymbol{r}_s d\boldsymbol{p_s}. \tag{5.2.3}$$

and the average circulation over an area S,

$$\Gamma = \int \int_S \langle \boldsymbol{\omega} \rangle \cdot d\mathbf{S}. \tag{5.2.4}$$

We now turn the focus to the numerical framework utilized to simulate the dynamics of confined *Active Carpet*.

5.3 Numerical simulations

In Sec.4.2.3 and Sec.4.3.3 of this thesis work, I described in detail how to make simulations of active carpet flows and to solve tracer particle dynamics in a similar way. This numerical simulations relies essentially on the correct sampling of the carpet configuration (see Fig.4.5) to measure carpet flows and by integrating simple tracer dynamics (see Fig.4.11). In the following, I review this briefly.

As discussed in Sec.5.2, we do not follow each microswimmer's trajectory in time. Instead, we investigate the effects of the *Active Carpet* in the surrounding fluid once microswimmers have passed from the ballistic regime to a diffusive regime (see Fig.4.10) [45, 41] . In brief, as reviewed in Sec.4.3.2, we model *Active Carpets* by randomly distributing N_s microswimmers with uniformly distributed positions $\boldsymbol{r}_s = (x_i, y_i, \sigma)$ and orientations $\boldsymbol{p}_s = (\cos\phi_i, \sin\phi_i, 0)$, with $\phi_i \in [-\pi, \pi]$, $i \in [1, N_s]$ in a finite square domain, $2L \times 2L$, where $2L$ is the size of the *Active Carpet*. The microswimmers number density in the *Active Carpet* is defined as $n = N_s/(2L)^2$. The total flow generated by the active carpet is computed by superposing the flow velocity of each individual microswimmer given by Eq.(5.1.9). Thus, the collective velocity field driven by the ensemble, or the colony, is determined by

$$\boldsymbol{v}(\boldsymbol{r}, \boldsymbol{r}_s, \boldsymbol{p}_s) = \sum_{i=1}^{N_s} \boldsymbol{u}_D(\boldsymbol{r}, \boldsymbol{r}_s, \boldsymbol{p}_s). \tag{5.3.1}$$

This velocity is computed for an ensemble of N_e independent *Active Carpet* configurations. Hence, we compute the variance tensor of the flow field Eq.(5.3.1), as defined in Eq.(5.2.2), averaging over a finite number of *Active Carpet* ensembles N_e. Using this framework, we investigate the dynamics of passive tracer particles stirred by the collective action of the colony. A tracer particle, with position $\boldsymbol{r}^T(t)$, evolves following the motion equation,

$$\frac{d\boldsymbol{r}^T(t)}{dt} = \boldsymbol{v}(\boldsymbol{r}^T, \boldsymbol{r}_s, \boldsymbol{p}_s). \tag{5.3.2}$$

As illustrated in Fig.5.1, we explore tracer particle dynamics between the *Active Carpet* and the free surface with their vertical position between $\sigma < z_0 < \mathrm{H}$. We integrate Eq.(5.3.2) numerically utilizing an

Euler scheme, with a nondimensional integration time step $\Delta t = 3 \cdot 10^{-2}\tau$. At each time step, the tracer particle excursions a length $\Delta \boldsymbol{r}^T$ determined by a new random independent *Active Carpet* ensemble.

The size of the *Active Carpet* is crucial in computing every observable within this framework. In [2] Mathijssen et al. stressed that if the *Active Carpet* is too small or resembles a bacterial cluster, a drift flow can suppress the hydrodynamic fluctuations, controlling the motion of the tracer particles. To mitigate this effect, we ensure the average flow $\langle v \rangle \approx 0$, performing simulations with sufficiently large *Active Carpet* [2, 45, 41] (see also Sec.4.3 for more details)

In this work, we set the following parameters unless otherwise stated: the microswimmer's body length and length scale $\sigma = 1$, the dipole strength $\kappa = f_{\parallel}\sigma = -30$ for a puller and $\kappa = 30$ for a pusher following [70, 69], the number density $n = 0.1$, microswimmers number $N_s = 10^5$, film thickness small parameter $\epsilon = 0.1$, ensemble number $N_e = 10^3$, and the *Active Carpet*'s total length $2L = 10^3$. Our primary focus is investigating the impact of the confinement size H and the interface strength λ. In what follows, we explore how the degree of fluid confinement impacts the spatial characteristics of the hydrodynamic stirring driven by *Active Carpets*.

5.4 Results and Discussion

5.4.1 Single microswimmer flow field within the floating film

Using the mathematical methods presented in Sec.5.1 we compute the flow field of a Stokeslet and a dipole parallel to both interfaces, as shown Fig.5.3. Near the origin, $z = 0$, in Fig.5.3 (bottom left) one can observe that the fluid in dragged down when going further (left or right direction) from the force dipole, clearly showing that boundary conditions are perturbed by the top image, which also presents a level of deviation. Importantly, Fig.5.3 (bottom right) shows that streamlines recirculating sharply on the contrary of the ones of a dipole near a solid boundary.

5.4.2 Active fluctuations within the floating film

We first characterize the hydrodynamic fluctuations driven by the confined *Active Carpet* whose members swim parallel to the fluid-fluid interface, as sketched in Fig.5.1. To this point, the theory developed by [2] allows us to directly compute the variance Eq.(5.2.2) of the flow field by performing a far-field approximation of the flow field (see Sec.5.2). Note that off-diagonal components of the variance tensor vanish. Additionally, by symmetry, we have that $\langle v_x^2 \rangle = \langle v_y^2 \rangle$ [45]. Therefore, we have only two fluctuations to characterize, the horizontal $\langle v_x^2 \rangle$ and the vertical one, $\langle v_z^2 \rangle$.

As a consequence of the confined geometry and the boundary conditions, the velocity field and its variance depend upon the ratio $\lambda = \mu_2/\mu_1$, characterizing the viscous interface, the thickness of the aquatic film H, as well as the intrinsic physical and geometrical parameters of the Stokes solution and far-field approximation. Hence, each variance component is a function of $\langle v_i^2 \rangle = \langle v_i^2 \rangle(n, \kappa, \sigma, \lambda, \epsilon, \mathrm{H}, z_0)$, where z_0 is the height of a fluid parcel relative to the *Active Carpet*. The obtained analytical expressions are

$$\begin{aligned}\langle v_x^2 \rangle = \frac{\pi \kappa^2 n}{64} \Bigg(& \frac{21\sigma^2\epsilon^2 - 22\sigma\epsilon\,(z_0 - 2\mathrm{H}) + 11\,(z_0 - 2\mathrm{H})^2}{(z_0 - 2\mathrm{H})^4} + \frac{336\sigma^2\lambda^2\epsilon^2}{(\lambda+1)^2 z_0^4} + \frac{160\sigma\lambda\epsilon}{(\lambda+1)^2 z_0^3} \\ & + \frac{36 z_0 (8\sigma\lambda\epsilon(\mathrm{H} + 2\sigma\epsilon) + \mathrm{H}(2\mathrm{H} + 3\sigma\epsilon))}{\mathrm{H}^5(\lambda+1)} - \frac{36 z_0^2 (2\sigma\lambda\epsilon(2\mathrm{H} + 5\sigma\epsilon) + \mathrm{H}(\mathrm{H} + 2\sigma\epsilon))}{\mathrm{H}^6(\lambda+1)} \\ & + \frac{8\mathrm{H}(\mathrm{H} + \sigma\epsilon) - 32\sigma\lambda\epsilon(2\mathrm{H} + 3\sigma\epsilon)}{\mathrm{H}^4(\lambda+1)} + \frac{44}{(\lambda+1)^2 z_0^2} \Bigg),\end{aligned} \tag{5.4.1a}$$

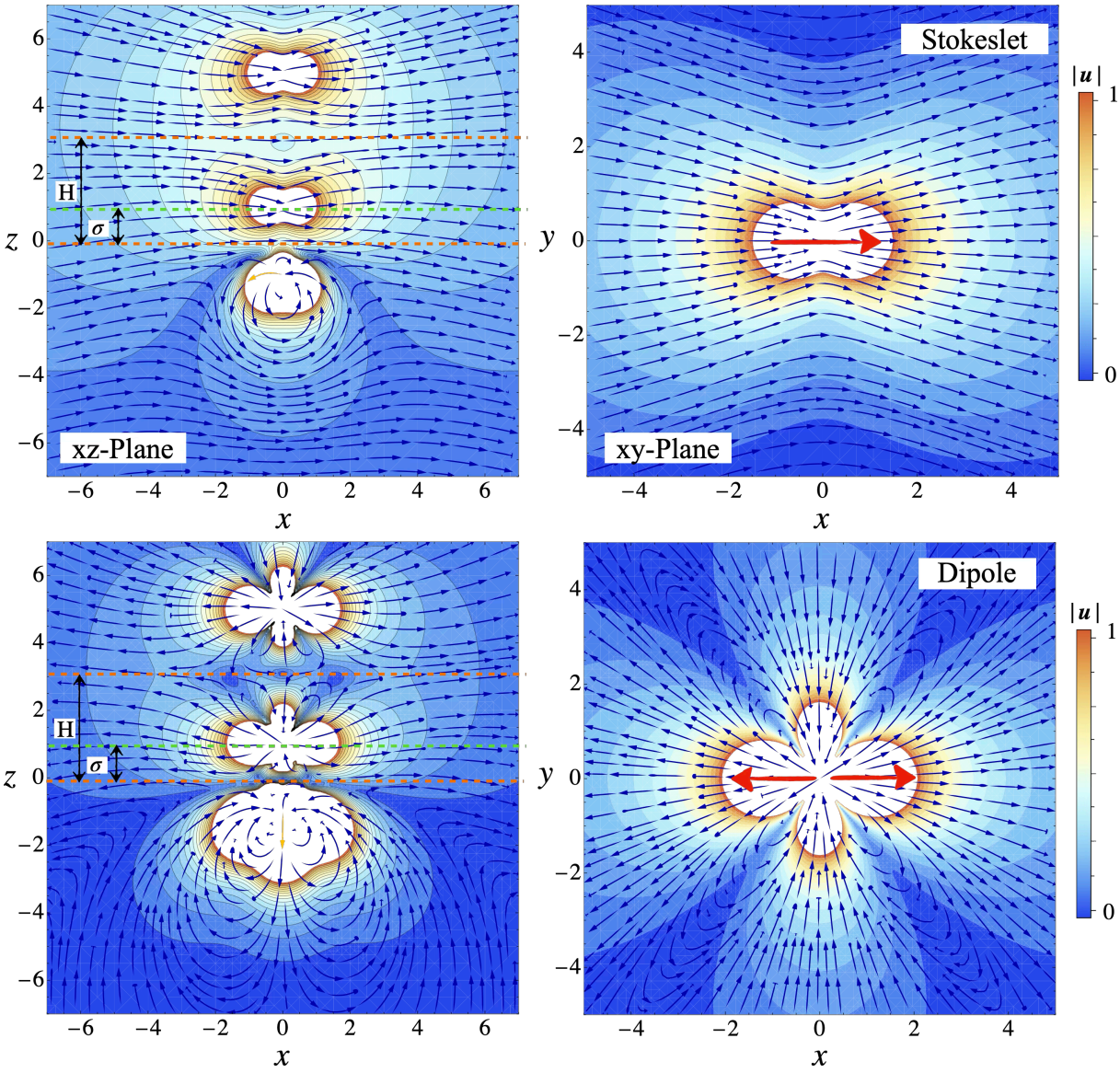

Figure 5.3: Flow field produced by a Stokeslet and a dipole within a floating film. The top row shows the flow field produced by a Stokeslet in the xz-plane (left) and in the xy-plane (right) for $\kappa = 30$, $\sigma = 1$ (green dashed line),$\lambda = 1.5$, and $\mathrm{H} = 3$ (top orange dashed line) for a better visualization of the image system. The bottom row shows the flow field by a pusher dipole for the same parameters.

$$\langle v_z^2 \rangle = \frac{9\pi\kappa^2 n}{32}\left(\frac{2\sigma^2\epsilon^2 - 2\sigma\epsilon\,(z_0-2\mathrm{H}) + (z_0-2\mathrm{H})^2}{(z_0-2\mathrm{H})^4} + \frac{80\sigma^2\lambda^2\epsilon^2}{(\lambda+1)^2 z_0^4} + \frac{32\sigma\lambda\epsilon}{(\lambda+1)^2 z_0^3}\right.$$
$$- \frac{4z_0(8\sigma\lambda\epsilon(\mathrm{H}+2\sigma\epsilon)+\mathrm{H}(2\mathrm{H}+3\sigma\epsilon))}{\mathrm{H}^5(\lambda+1)} + \frac{4z_0^2(2\sigma\lambda\epsilon(2\mathrm{H}+5\sigma\epsilon)+\mathrm{H}(\mathrm{H}+2\sigma\epsilon))}{\mathrm{H}^6(\lambda+1)} \tag{5.4.1b}$$
$$\left. + \frac{4}{(\lambda+1)^2 z_0^2}\right).$$

Note that the hydrodynamic fluctuations driven by the active carpet are proportional to the number density n and the square of the dipole strength κ^2. Hence, the behavior of these fluctuations is independent of whether the swimmer is a puller or a pusher. Also, $\epsilon \ll 1$ but not zero; the limit $\epsilon \to 0$ does not have a physical interpretation. To validate these analytical results, we performed simulations using Eq.(5.3.1) to obtain numerically the variance for a set of z_0 values within the range (σ, H).

Fig.5.4(a) presents the analytical and simulation results for the variance, in the case of pullers microswimmers, with $\lambda = 1.5$ and $\mathrm{H} = 40$. First, the theory (shown in lines and in the inset as dashed,

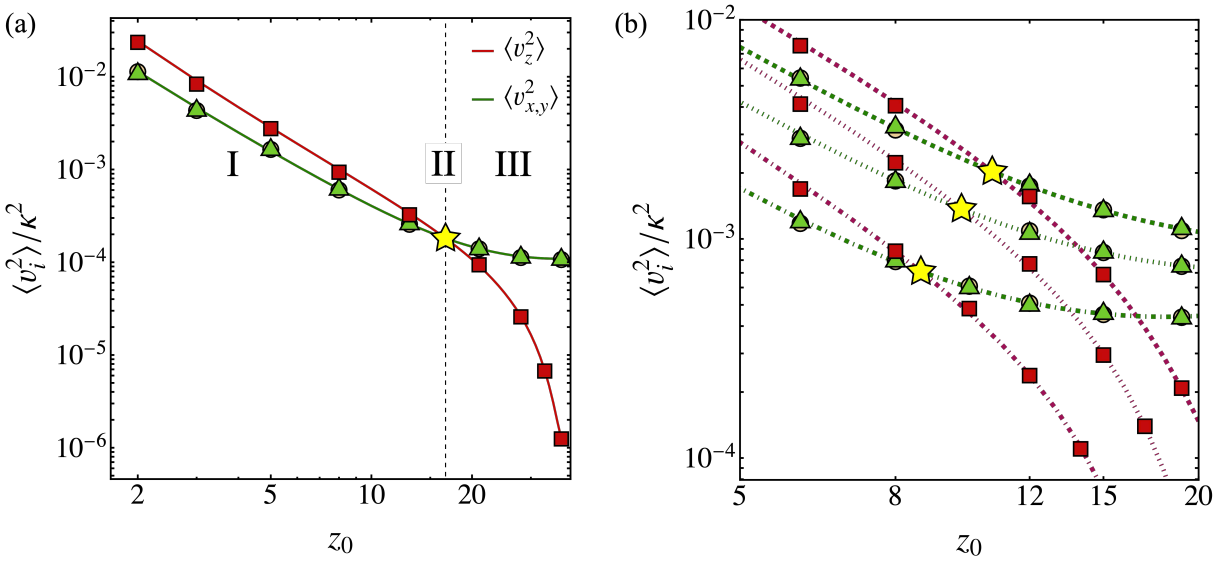

Figure 5.4: Anisotropic diffusion driven by *Active Carpets*. (a) Variance of the hydrodynamic fluctuations driven by an *Active Carpet* in the horizontal and vertical directions (green, red solid lines), as defined in Eq.(5.2.2). Markers are simulation points obtained from Eq.(5.3.1). The star marks the intersection between theoretical variances $\langle v_z^2 \rangle(z_\star) = \langle v_{xy}^2 \rangle(z_\star)$. Regions I, II and III indicate the dominance of fluctuations according to the distance from the Active Carpet. Here H = 40 and $\lambda = 1.5$. (b) Theoretical variances for H = 20, and three different values of λ, $\lambda = 0.1, 0.5, 1.5$, denoted by dashed, dotted and dash-dotted lines, respectively. Stars are cross-points.

dot-dashed lines) and simulations (in symbols) show great agreement. Second, the effect of confinement in the biogenically driven fluctuations is severe. As the plot shows, horizontal and vertical fluctuations are non-monotonic and anisotropic with a crossing at a particular height, which we denote as $z_0 = z_\star$. We found that vertical variances are more significant than horizontal ones for almost half the film thickness, $z_0 \propto 0.43\mathrm{H}$. Using the expressions Eq.(5.4.1a),and Eq.(5.4.1b), we can determine exactly that they cross at height $z_\star = 16.6$ (represented by the yellow star on the plot). At this height, we expect the fluctuations to have the same strength. Moreover, horizontal fluctuations become more significant for heights closer to the free surface, $z_0 > z_\star$. According to this unique feature, we can separate the space into three regions, denoted by I, II, and III. Region I represents the range of heights where vertical fluctuations dominate over horizontal fluctuations; Region II represents the locus where fluctuations are isotropic; whereas Region III represents the range of heights where horizontal fluctuations dominate over vertical fluctuations. To illustrate this feature, Fig.5.4(b) shows results of fluctuations for different values of λ in the list [0.1,0.5,1.5] (dashed, dotted and dot-dash, respectively) and a film thickness H = 20. The variance curves intersect in the same fashion. Results show that the cross-point $z_\star$ varies depending on the value of λ. Smaller values of λ lead cross-points closer to the top free surface, and the contrary happens for greater values, i.e., the cross-point gets closer to the *Active Carpet*.

Therefore, characterizing the locus $z_\star$ and its dependence on the parameters controlling the degree of confinement is essential since it determines where fluctuations and the flow direction become spatially biased.

5.4.3 Dispersion of tracer particles

We carried out simulations using Eq.(5.3.2) to prove that the anisotropic behavior of fluctuations effectively impacts surrounding tracer particles depending on the region where they excursion. We created an *Active Carpet* confined within a film of thickness H = 40, and the bottom interface was characterized by a viscosity ratio $\lambda = 1.5$. From the analytical solution Eq.(5.4.1), we determined the intersection height $z_\star$ by resolving the equation $\langle v_x^2 \rangle(z_\star) = \langle v_z^2 \rangle(z_\star)$. Once determined $z_\star$, we characterized the fluctuations topology by seeding passive tracers at different heights relative to $z_\star$. Thus, we released particles at a height $z_0 = 27.7 > z_\star$ to measure vertical-dominated motions, at a height $z_0 = z_\star$ to measure isotropic motions, and a height $z_0 = 10 < z_\star$ to measure horizontal-dominated motion. Then, we simulated

$\tau_e = 180$ time steps by numerically integrating Eq.(5.3.2). This time was enough to determine the characteristic topology of the space through which the hydrodynamic fluctuations transport tracers. Fig.5.5 show a single and multiple trajectories of tracer particles obtained from the simulations.

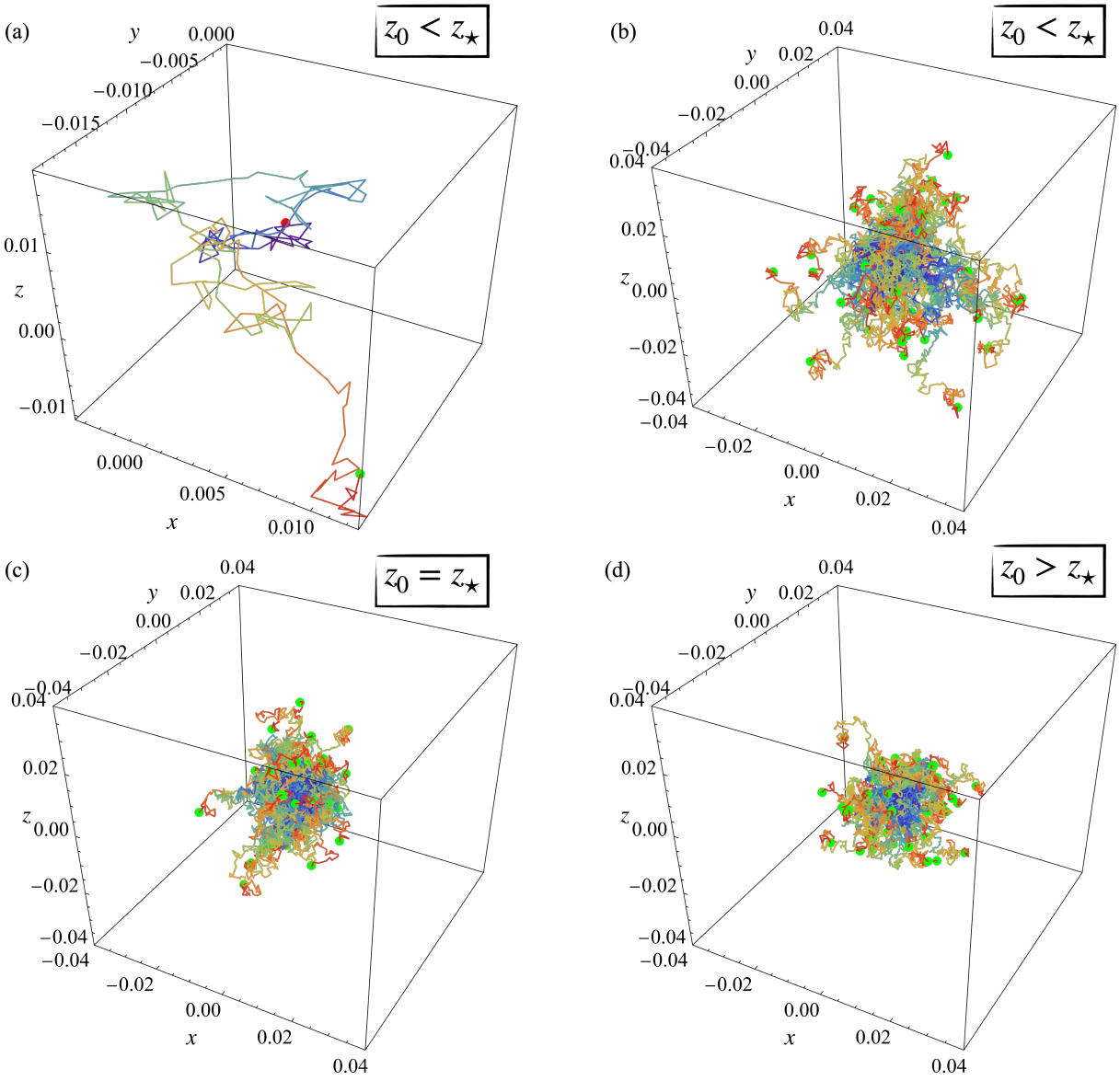

Figure 5.5: Tracer particle trajectories within the floating film for H = 40 and $\lambda = 1.5$ starting from initial position (red sphere), then displacing through the medium $\tau_e = 180$ time steps (coloured segments) to its final position (green sphere). (a) Single tracer trajectory for a particle starting at $z_0 = 10 < z_\star$. From (b) to (d) 50 tracer trajectories per each starting height z_0 are presented.

To characterize the dispersion topology we average the displacement $\overline{d}_i$ for all tracer particles in every direction $\hat{e}_i$, $i = x, y, z$. The ellipsoids in Fig.5.4(b) (scaled for visualization) show the resulting topology for each region.Thus, we confirm that tracer particles have a more prominent vertical motion at heights $z_0 < z_\star$ (red) closer to the *Active Carpet*, equal to horizontal motions at $z_0 = z_\star$ (ginger) and that horizontal motions become dominant at $z_0 > z_\star$ (green).

5.4.4 Impact of confinement on fluctuation's geometry

In the previous section, we studied a particular example that demonstrated the zonification of hydrodynamic fluctuations across the fluid layer. Throughout this section, we show how the degree of confinement,

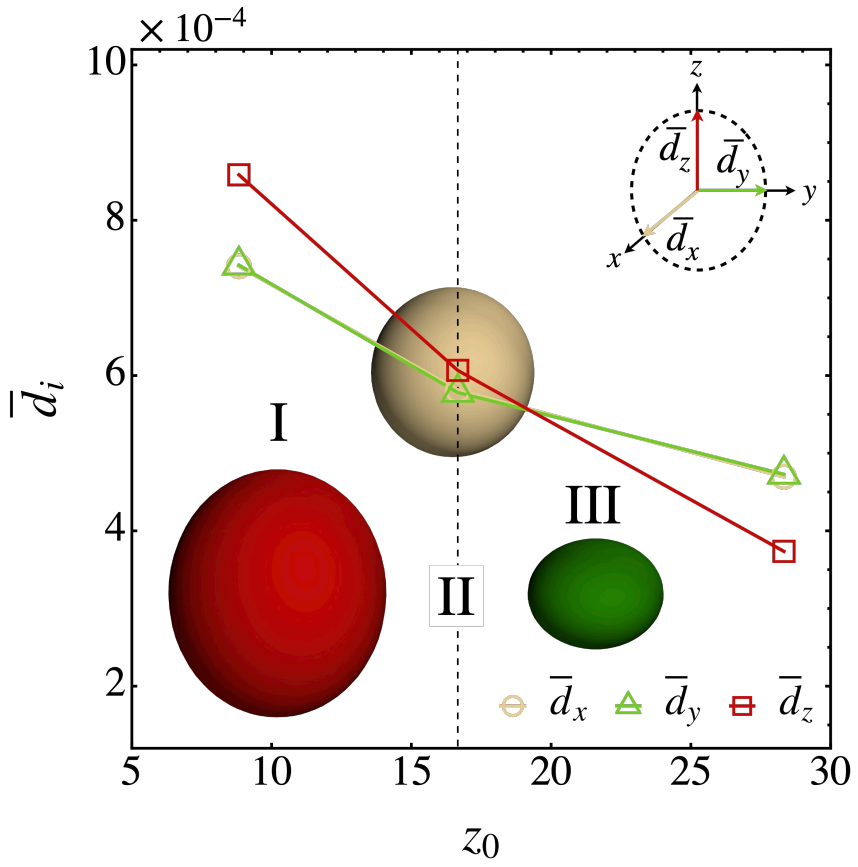

Figure 5.6: Ellipsoids represent the average displacement of tracer particles computed from Eq.(5.3.2) for each fluctuation region. In green, tracer particles start at $z_0 < z_\star$, while in red, they start at $z_0 < z_\star < \mathrm{H}$. In ginger, they start exactly at $z_0 = z_\star$.

determined by H and λ, impacts the geometry of the biogenically driven hydrodynamic fluctuations, addressing the following question: How does $z_\star$ change in terms of λ and H? Fig.5.4 reveals a significant anisotropy and non-monotonic behavior of the hydrodynamic fluctuations induced by the confined *Active Carpet*. A major result is that we found the existence of three regions whose spatial distribution is determined by $z_\star$; the height above the *Active Carpet* at which the vertical and horizontal variance of the velocity fluctuations equal, heights z lower than $z_\star$ where vertical fluctuations dominate over horizontal fluctuations, and heights between $z_\star$ and H, horizontal fluctuations dominate over vertical fluctuations. The analytical solution Eq.(5.4.1) reported in Sec.5.4.2 enables us to describe and analysis these three regions change as function of H and λ.

We computed $z_\star(\lambda, \mathrm{H})$ for a wide range of film thicknesses H, and varying the viscous fluid-fluid interface ratio λ over a range that could potentially be observed in aquatic environments [20, 16, 4]. For this, we resolve numerically the nonlinear equation for $\langle v_x^2\rangle(z, \mathrm{H}, \lambda) - \langle v_z^2\rangle(z, \mathrm{H}, \lambda) = 0$ for $z \in (\sigma, H)$, which root corresponds to $z_\star$.

Fig.5.7 illustrates the dependency of $z_\star$ with the film thickness H and λ within the range $\lambda \in [0, 4]$ and $20 \leq \mathrm{H} \leq 100$. First, we identify that $z_\star$ increases monotonically with H. This implies that thicker aquatic films create conditions where vertical fluctuations dominate over horizontal fluctuations. From an ecological viewpoint, this is relevant since the *Active Carpet* can have a longer range for attracting or repealing mass. Second, $z_\star$ is larger for smaller λ. In other words, the more viscous the layer where the *Active Carpet* habits, the longer the extent of the region where vertical fluctuations dominate over horizontal fluctuations. For the extreme case of $\lambda \to 0$, the fluid where the *Active Carpet* lives in is dramatically more viscous than the fluid below, $\mu_1 \gg \mu_2$. Such a big difference in viscosity can be observed in fresh and marine aquatic environments, where algae blooms can locally change the physico-chemical properties in the water column [129]. At some point, these significant spatial changes in viscosity push the fluid away from the Newtonian limit. Nonetheless, Newtonian rheology remains a fair approximation

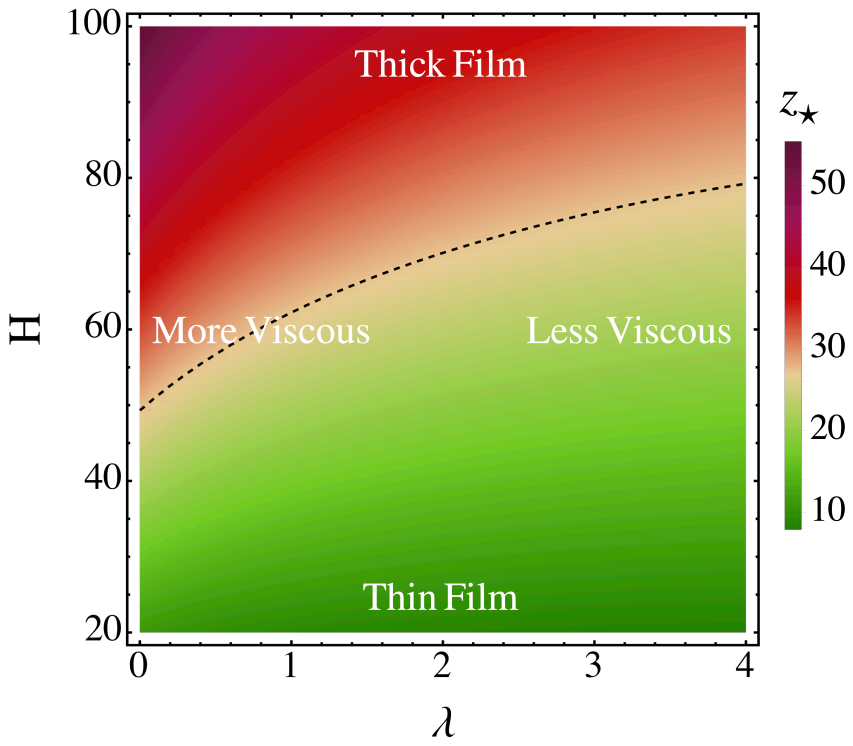

Figure 5.7: The impact of confinement of the flow structure driven by *Active Carpets*. Analytical solutions for the cross-point height $z_\star$ for a domain of the parameters λ and H are shown. The black dashed line represents a level curve when $H(\lambda) \propto \sqrt{\lambda}$.

for gently varying fluid viscosity, as in the case of liquid water [130]. For $\lambda = 0$, and the range of H values here explore, we obtain that $z_\star = 0.55$H. Whereas for a slightly larger value, $\lambda = 0.5$, we obtain that $z_\star = $ H/2. This means that fluctuations in regions I and III will have almost the same extent. At larger values of λ, the proportionality we just described changes. Fig.5.7 shows a different result for $\lambda = 4$, where we find that in average $z_\star = 0.35$H. In this scenario, the fluid-fluid interface strengthens by making λ larger. Consequently, from our framework, one would expect to recover the well-studied hydrodynamic system of a free-surface liquid film held by a rigid surface for $\lambda \gg 1$ [9]. As a result, we observe that for larger λ, the hydrodynamic fluctuations are, on average, more planar-directed motions than vertical motions since the region dominated by vertical fluctuations reduces to 35% of the film's thickness; i.e., horizontal fluctuations dominate over 75% of the film. This behavior mirrors the viscous control observed in analogous scenarios, such as superconfined subsurface faults, where viscosity drives fluid flow fluctuations towards quasi-two-dimensional states [131, 132]. From these results, it is apparent that λ plays a significant role in unbalancing the system and changing the architecture of the hydrodynamic fluctuations so that the confined *Active Carpet* may promote, for example, biogenic mass reorganization mechanisms such as aggregation, recently investigated in a semi-infinite fluid [41].

5.4.5 Active Carpet's collective flow correlation

The results in Fig.5.7 highlight the tangible influence of both geometrical and viscous confinements on the spatial structure of velocity fluctuations. This influence extends beyond fluctuations, wielding significant control over *Active Carpets* and shaping the trajectories followed by passive tracers. Consequently, an intriguing question arises: Could confine *Active Carpets* potentially catalyze the emergence of aggregated large-scale coherent flow patterns? We delve into this question by examining the coherence of fluid motions and patterns in space using pair velocity correlation and vorticity fields.

A defining feature of living systems is their ability to induce mechanical disturbances on their surroundings over scales greater than their characteristic individual size, prompting investigations into their potential for enhancing mixing in aquatic environments. This capacity of swimming organisms in stirring fluids, particularly through interactions with each other, has garnered significant attention in recent years

[33, 58, 36, 133, 35, 38, 134]. In the case of microbes swimming in stratified layered waters–characterized by sharp vertical gradients in density–theoretical arguments suggest individual swimmers have low capacity to mix fluid [3, 55]. However, whether the collective action of tiny swimming organisms can significantly affect the functioning of the fluid environment remains an open debate [55, 52, 53]. This motivates our quest for large-scale hydrodynamic structures driven by *Active Carpet* within confined layered aquatic systems. Pair velocity correlation emerges as a metric for understanding the relationships between fluid parcel dynamics and biogenic fluid perturbations [40, 2, 41].

We compute the spatial pair velocity correlation to examine how the geometrical and viscous confinement affects the coherence of the flow defined as

$$C_i(d_0) = \frac{\langle v_i(\boldsymbol{r}_1) v_i(\boldsymbol{r}_2)\rangle_e}{\sqrt{\langle v_i^2(\boldsymbol{r}_1)\rangle_e \langle v_i^2(\boldsymbol{r}_2)\rangle_e}}, \tag{5.4.2}$$

where $d_0 = |\boldsymbol{r}_2 - \boldsymbol{r}_1|$ is the Euclidean distance between two fluid parcels in position $\boldsymbol{r}_1$ and $\boldsymbol{r}_2$ with fixed height z_0, above the *Active Carpet*, as shown in Fig.5.8. The operator $\langle\cdot\rangle_e$ represents an *Active Carpet* ensemble average, and the variance tensor Eq.(5.2.2) is utilized to compute the numerator in Eq.(5.4.2). To compute Eq.(5.4.2) from numerical simulations, we first evaluate the flow induced by the *Active Carpet* at $\boldsymbol{r}_{1,2} = (\pm d_0/\sqrt{2}, \pm d_0/\sqrt{2}, z_0)$ with $z_0 = 10$ for a wide range of distances $d_0 \in [0.01, 200]$. Then, we compute Eq.(5.4.2) for each ensemble and take the average over ensembles. Results are shown and discussed next.

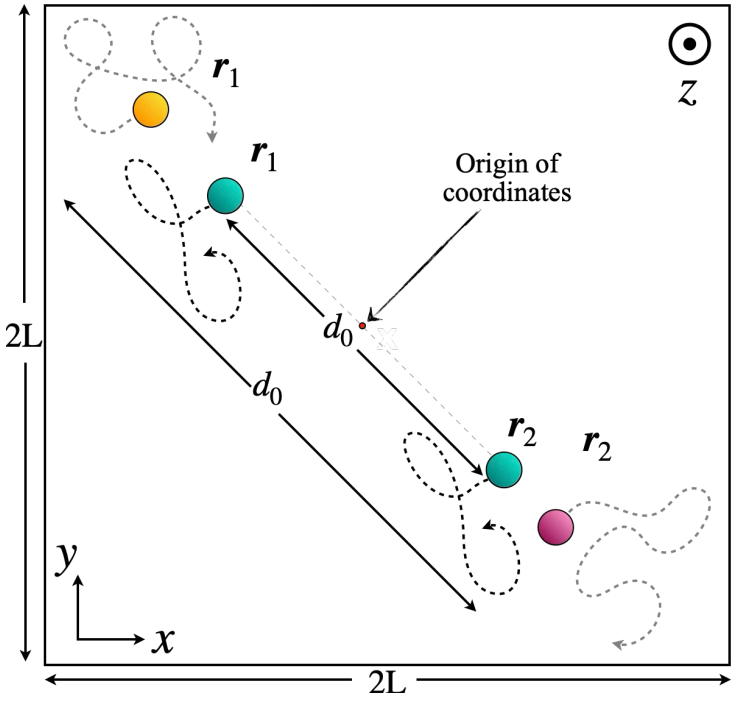

Figure 5.8: Scheme of how pair velocity correlations are measured. The active carpet flows are first measured at positions $\boldsymbol{r}_1, \boldsymbol{r}_2$ represented by cyan disks as tracer particles separated by a small distance d_0. As shown, if one would really follow their trajectories, they would be similar because they are close to each other so the measured flows are also similar in magnitude. Making d_0 larger, make the flows to differ noticeably from each other, which traduces in tracer particles following different trajectories (orange and pink disks).

Fig.5.9(a) displays the pair velocity correlation, $C_x(d_0)$, in the $\hat{e}_x$ direction, representing horizontal correlation, as a function of d_0/H for pullers microswimmers. For simplicity, we omit results for $\hat{e}_y$, which is symmetric to those in $\hat{e}_x$. We examine the horizontal velocity pair correlation between particles separated by a distance d_0 (see insets) for three H values (H $\in [20, 40, 100]$), with a fixed λ (λ = 1.5) and a representative height $z_0 = 10$ above the Active Carpet. Note that we normalize d_0 by H to gauge the characteristic length of decorrelation relative to the film thickness. The varying H range allows us to observe that increasing geometrical confinement (i.e., thinner H) expands the relative extent of positively correlated tracer motions over distance d_0. The results indicate that horizontal flows exhibit slower decorrelation, with increasing distance d_0, in more confined systems. The latter trend

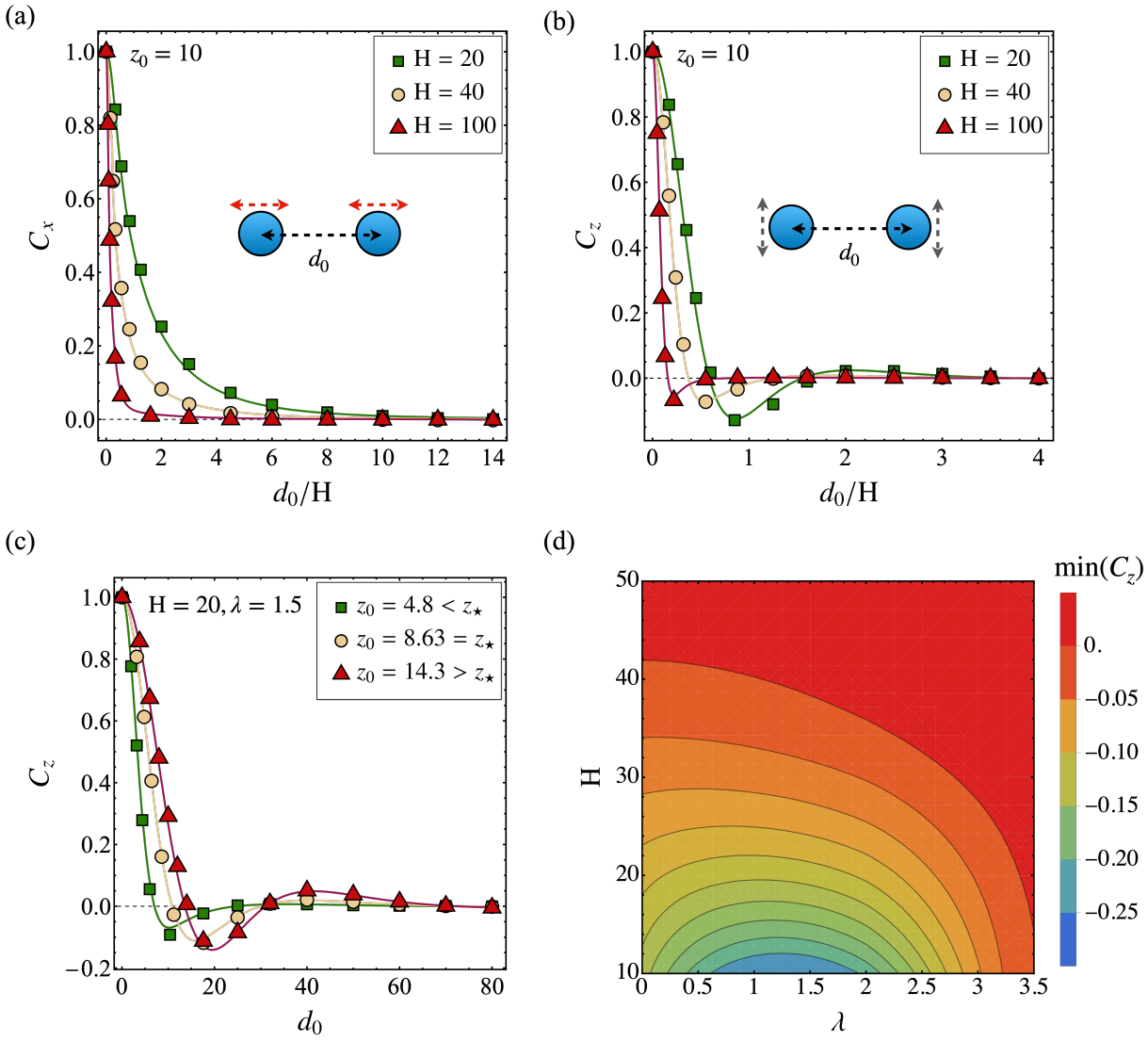

Figure 5.9: (a), (b) Velocity pair correlation function $C_x(d_0)$, $C_z(d_0)$ in terms of the relative distance between a pair of tracer particles, d_0, normalized by the confinement size relative to the Active Carpet H measured at height $z_0 = 10$, for pullers microswimmers with $\lambda = 1.5, \sigma = 1$, and $\kappa = -30$. Plot markers correspond to numerical simulations using Eq.(5.4.2) and lines to the semi-analytical far-field approximation using Eq.(5.2.1). Insets: Illustrative scheme for measuring the velocity pair correlation between two fluid parcels separated by a distance d_0. (c) Vertical velocity pair correlation function $C_z(d_0)$, for H = 20 and $\lambda = 1.5$ at different heights z_0 according to fluctuations regions described in Sec.5.4.2. (d) Phase diagram of the vertical pair correlation minima versus λ and H.

is evident when comparing the curves associated with high (H = 20) and low (H = 100) geometrical confinements, suggesting that *Active Carpets* struggle to disrupt fluid parcels parallel motion. As a side note, we remark that our numerical findings align with the semi-analytical solution for $\langle v_i(\boldsymbol{r}_1)v_i(\boldsymbol{r}_2)\rangle = \int v_i(\boldsymbol{r}_1)v_i(\boldsymbol{r}_2)F d\boldsymbol{r}_s d\boldsymbol{p}_s$, shown by solid lines in Fig.5.9.

Given that the confinement of *Active Carpets* primarily occurs in the vertical direction, we examine the horizontal pair correlation in the $\hat{e}_z$ direction, $C_z(d_0)$, which we refer to as vertical pair correlation. The results in Fig.5.9(b) for $\lambda = 1.5$ demonstrate not only good agreement between numerically obtained results (markers) and semi-analytical solutions (lines) but also reveal notable differences from horizontal pair correlation (C_x), as shown in Fig.5.9(a).

An intriguing result is the significantly shorter decorrelation distance for flow fluctuations in the vertical direction compared to horizontal fluctuations. This is evident from the distance $d_0/$ (H) over which the C_z and C_x curves decay to zero. The vertical pair correlation decays at least three times faster

than the horizontal pair correlation, suggesting a distinct behavior. Moreover, a key difference is the occurrence of negative values in C_z, indicating flow fluctuations in opposite directions at specific distances d_0. Such behavior is commonly associated with vortical flow structures, also observed in microswimmer's sheets, active turbulence experiments, and bacterial swarming [135, 136, 137, 136].

In the most confined scenario examined here (see green squares in Fig.5.9(b)), the curve reaches its minimum $\min(C_z)$ almost at $d_0 \approx \mathrm{H}$, suggesting that fluid parcels move in opposite directions at horizontal distances d_0 that scale with the size of the geometrical confinement H. The emergence of such large-scale flow structures raises intriguing possibilities. For instance, microbial colonies formed by a monolayer of swimmers, resembling an *Active Carpet*, could potentially create coherent flow structures in the water column nearly 20 times their characteristic thickness under strong confinement.

In Sec.5.4.2, we defined the region where active fluctuations exhibit a preferred direction. As this effect originates from the flow, we can thoroughly examine the vertical pair correlation C_z in detail. To illustrate how C_z changes at different heights, we fix the values of $\mathrm{H} = 40$ and $\lambda = 1.5$ while varying the position z_0 at which flows are measured. The results presented in Fig.5.9(c) demonstrate the sensitivity of C_z with respect to the height above the *Active Carpet*.

We have highlighted that the vertical pair correlation reaches a minimum, indicating a region where fluid experiences vertical flow fluctuations in opposing directions. To further explore the intensity of this negative correlation, we vary H and λ. Fig.5.9(d) presents the minimum vertical pair correlation $\min(C_z)$ for film thickness in the range $\mathrm{H} \in [10, 50]$ and viscosity ratio $\lambda \in [0, 3.5]$, computed using the semi-analytical approach. Our analysis reveals that the negative correlation, and thus the intensity of opposing flows, becomes stronger with increased geometrical confinement. Interestingly, we also observe that viscosity confinement, controlled by λ, enhances $\min(C_z)$ within the range $\lambda \in [0.5, 2]$. The nonmonotonic dependence with λ is exciting and warrants future research for extreme conditions. In the limit of a non-slip boundary at the viscosity interface, i.e., $\lambda \to \infty$, we observe the pair velocity correlations briefly take negative values in the planar and vertical directions. The latter suggests the appearance of a weak complex flow structure related to the action of the *Active Carpet* and confinement. Conversely, in the case of a free-surface and unconfined aquatic environment, i.e. $\lambda \to 0$ and $H \to \infty$, the system does not show significant evidence of an emerging fluid flow structure. For a better understanding of the fluid dynamics of this asymptotic scenario, we refer the reader to [4].

5.4.6 Roll-like formation

Whether confined fluid environments give rise to large-scale flow structures remains unanswered. In our study, we delve into the emergence of vortical flows induced by confined *Active Carpets* by examining the spatial structure of the flow vorticity Eq.(5.2.3) and the circulation Eq.(5.2.4). We investigate these quantities in a Cartesian coordinate system (x, y, z) to ensure clarity and guide our search for large-scale patterns amidst the biogenic flow fluctuations. In Fig.5.10(a)(b)(c), we illustrate the vorticity field for pullers microswimmers on the z-x plane for $H = 20$, $\lambda = 1.5$ and $\kappa = -30$, computed from Eq.(5.2.3) using a semi-analytical approach with a spatial resolution of $\Delta z = 0.5$ and $\Delta x = 0.5$. To highlight coherent trends, we show the sign of the vortical velocity j-component ω_j, coloring counterclockwise motions in red (+1), clockwise motions in blue (-1), and no motion in white (0). The findings confirm the existence of vortical flow patterns analogous to roll-like formations (exhibiting positive and negative vorticity). To reinforce this idea, we measured the circulation $\Gamma(\ell)$ over different squared-sized surfaces ℓ^2 for the vorticity ω_y normal to the plane $x - z$. In Fig.5.10(d)(e), we defined three different regions, A, B, and C, where we measured the circulation over different squared areas of side ℓ. We observe regions A (in blue) and B (in red) display circulation in opposite directions with peaks showing vortical flows of different sizes ℓ that we compare with the system size H.

Our results offer a glimpse into the ability of *Active Carpets* to drive large-scale flow structures in confined environments, bearing striking similarities to phenomena like bio-convection [33, 23], biogenic flows in extremely confined systems [137], thermally-driven convection in super confined environments [138, 139], and kitchen flows [140]. Such confined flows, characterized by roll-like patterns, are renowned for their high mixing efficiency [33, 131]. In essence, our findings raise fundamental questions about the power of *Active Carpets* inhabiting layered environments to shape their surroundings, enhance the mixing of suspended and dissolved mass in aquatic environments, and facilitate transport between fluid-fluid interfaces and layers.

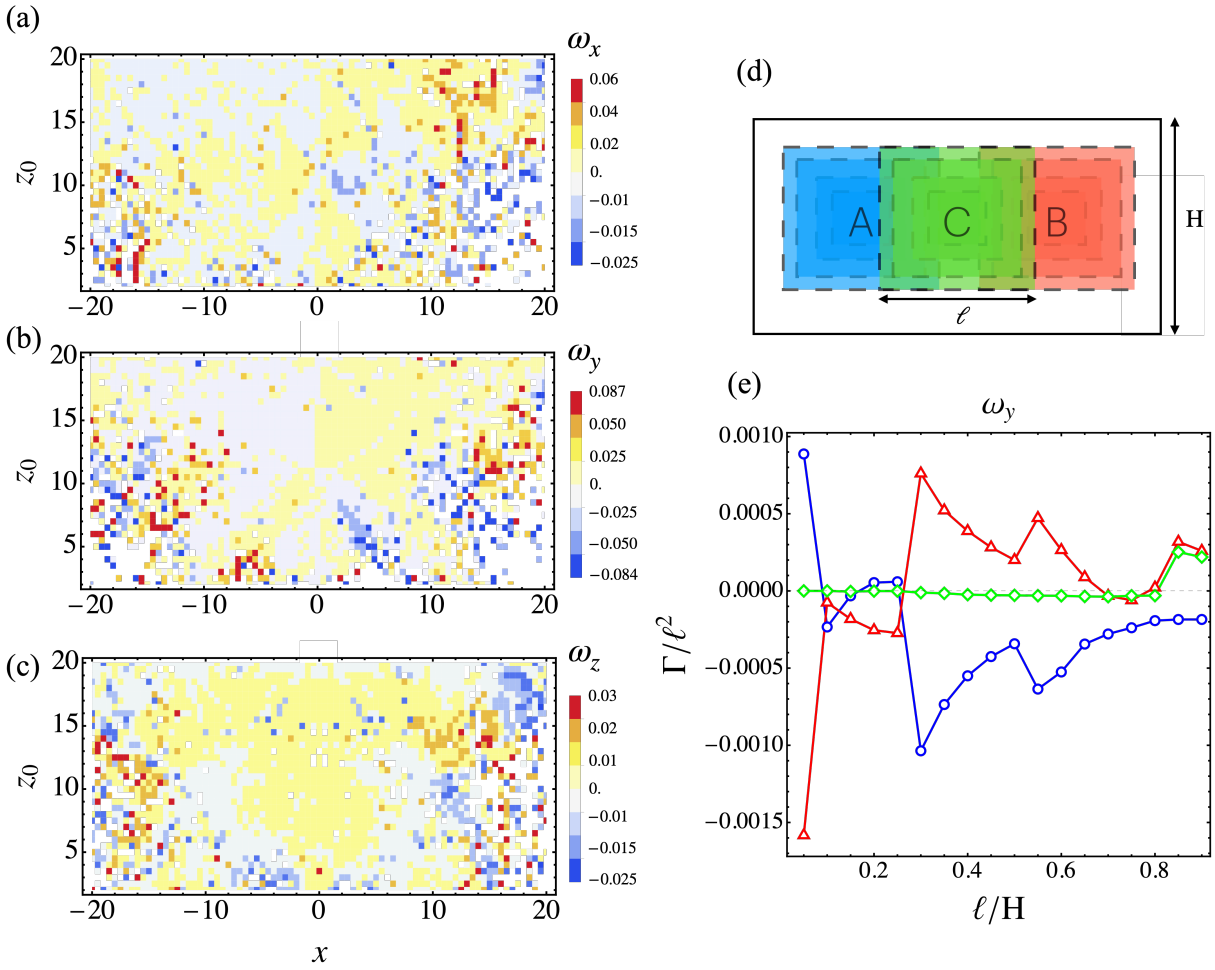

Figure 5.10: *Active Carpets* can drive large-scale recirculations. (a)(b)(c) Average vorticity exerted by an *Active Carpet* on fluid parcels across the confinement space, in the plane $x-z$, for puller microswimmers H = 20, $\lambda = 1.5$, $\kappa = -30$, and $\sigma = 1$. The color code for vortical flows is the next, Anti-clockwise rotations (blue) and clockwise rotations (red); the magnitude of the vorticity is indicated in the legends of each component. (d) Regions A, B, and C were used to evaluate the circulation Eq.(5.2.4) over the confinement space. Squares with side ℓ were utilized in each area to measure the circulation. (e) Circulation Γ associated with the vorticity in the y direction, divided by the area ℓ^2.

Chapter 6

Conclusions

In this thesis, we have delved into the hydrodynamics of confined *Active Carpets* within layered aquatic systems. This thesis work centered on three main aspects: (i) characterizing the spatial distribution of hydrodynamic fluctuations and the dispersion of passive tracers (Sec.5.4.2 and Sec.5.4.3), (ii) assessing the influence of geometrical and viscous confinement on the hydrodynamics driven by *Active Carpets* (Sec.5.4.4), and (iii) exploring the emergence of macroscopic hydrodynamic structures, referred to herein as roll-like formations (Sec.5.4.5 and Sec.5.4.6).

We derived analytical expressions for the active flow fluctuations induced by *Active Carpets* confined in a layer of thickness H, between a free surface and a fluid-fluid interface characterized by a viscosity ratio. Our solutions revealed a pronounced non-monotonic behavior in the biogenic hydrodynamic fluctuations, particularly in the vertical direction. This characteristic contrasts with observations made in an *Active Carpet* near a single surface system [45, 41]. The non-monotonic dynamics of these hydrodynamic fluctuations are intricately influenced by the degree of geometrical and viscous confinement imposed by H and the viscosity ratio $\lambda = \mu_2/\mu_1$ at the fluid-fluid interface, where μ_1 is the viscosity of the fluid where the *Active Carpet* lives, and μ_2 is the viscosity of the deeper layer. Numerical simulations corroborated the findings obtained from analytical solutions. These simulations provided a deeper exploration into the dynamics of passive tracer particles, showcasing the height-dependent topology of motions above the *Active Carpet*.

We showed how the topology of hydrodynamic fluctuations undergoes transformation depending on the degree of geometrical confinement and the intensity of the viscosity ratio at the fluid-fluid interface boundary. Notably, we have uncovered the presence of three distinct spatial regions: (I) A proximal region to the *Active Carpet* where vertical fluctuations supersede horizontal fluctuations; (II) An intermediate region characterized by isotropic hydrodynamic fluctuations; and (III) The furthest region from the *Active Carpet* where horizontal fluctuations prevail over vertical fluctuations. This newfound understanding equips us with a tool to wield control over directed motion within confined vertical spaces. Furthermore, it illustrates how both dependencies are intrinsically linked to the amplification or diminishment of regions of agitation.

By measuring the velocity pair correlation of the exerted hydrodynamic fluctuations induced by the confined *Active Carpet*, we demonstrated the existence of coherent vortical motion predominantly propelled by vertical flows. Our investigation pinpointed that the characteristic length of the formed roll-like patterns is intimately tied to the thickness of the confined layer harboring the *Active Carpet*. Remarkably, these coherent vortical structures manifest with exceptional prominence in highly confined systems and in the presence of sharp viscosity jumps at the fluid-fluid interface.

These findings carry implications for our comprehension of microbial swimmers that flourish and cultivate biofilms at interfaces in natural shallow water environments [4], such as (i) ponds etched upon soil and ice [141, 142], (ii) shallow saline lagoons and wetlands [143], (iii) streams [144], inside the human body [14, 145] and even in human habitats like the thin films of water found in kitchens, bathrooms, swimming pools and laboratories [146, 147].

To conclude, by shedding light on the dynamics of these active flows, this thesis work offers insights into the behavior of microbial communities in thin layers within aquatic ecosystems. From pristine natural

settings to human-altered landscapes, the understanding of the hydrodynamics induced by *Active Carpets* is crucial for devising strategies to manage and harness the potential of microbial populations for various applications, ranging from water remediation to microfluidics and biotechnology.

References

[1] Anup V Kanale et al. "Spontaneous phase coordination and fluid pumping in model ciliary carpets". *Proceedings of the National Academy of Sciences* 119.45 (2022), e2214413119.

[2] Arnold JTM Mathijssen et al. "Nutrient transport driven by microbial active carpets". *Physical Review Letters* 121.24 (2018), p. 248101.

[3] Rishabh V More and Arezoo M Ardekani. "Motion in Stratified Fluids". *Annual Review of Fluid Mechanics* 55 (2023), pp. 157–192.

[4] Nikhil Desai and Arezoo M Ardekani. "Biofilms at interfaces: microbial distribution in floating films". *Soft Matter* 16.7 (2020), pp. 1731–1750.

[5] Liana Vaccari et al. "Films of bacteria at interfaces". *Advances in colloid and interface science* 247 (2017), pp. 561–572.

[6] Adib Ahmadzadegan et al. "Hydrodynamic attraction of bacteria to gas and liquid interfaces". *Physical Review E* 100.6 (2019), p. 062605.

[7] Daniela Pimponi et al. "Hydrodynamics of flagellated microswimmers near free-slip interfaces". *Journal of Fluid Mechanics* 789 (2016), pp. 514–533.

[8] Jens Elgeti and Gerhard Gompper. "Microswimmers near surfaces". *The European Physical Journal Special Topics* 225 (2016), pp. 2333–2352.

[9] Arnold JTM Mathijssen et al. "Hydrodynamics of micro-swimmers in films". *Journal of Fluid Mechanics* 806 (2016), pp. 35–70.

[10] Brato Chakrabarti, Stanislav Y Shvartsman, and Michael J Shelley. "Cytoplasmic stirring by active carpets". *arXiv preprint arXiv:2311.04452* (2023).

[11] William Gilpin, Matthew Storm Bull, and Manu Prakash. "The multiscale physics of cilia and flagella". *Nature Reviews Physics* 2.2 (2020), pp. 74–88.

[12] Silvia Espada Burriel and Remy Colin. "Active Density Pattern Formation in Bacterial Binary Mixtures". *PRX Life* 2.2 (2024), p. 023002.

[13] Yuto Hosaka, Ramin Golestanian, and Abdallah Daddi-Moussa-Ider. "Hydrodynamics of an odd active surfer in a chiral fluid". *New Journal of Physics* 25.8 (2023), p. 083046.

[14] Akshay J Maheshwari et al. "Colloidal hydrodynamics of biological cells: A frontier spanning two fields". *Physical Review Fluids* 4.11 (2019), p. 110506.

[15] William M Durham and Roman Stocker. "Thin phytoplankton layers: characteristics, mechanisms, and consequences". *Annual review of marine science* 4 (2012), pp. 177–207.

[16] Òscar Guadayol et al. "Microrheology reveals microscale viscosity gradients in planktonic systems". *Proceedings of the National Academy of Sciences* 118.1 (2021), e2011389118.

[17] Michael R Stehnach et al. "Viscophobic turning dictates microalgae transport in viscosity gradients". *Nature Physics* 17.8 (2021), pp. 926–930.

[18] Michael Cohen et al. "Biofilms in chronic rhinosinusitis: a review". *American journal of rhinology & allergy* 23.3 (2009), pp. 255–260.

[19] Karen L Visick et al. "Biofilms 2015: multidisciplinary approaches shed light into microbial life on surfaces". *Journal of Bacteriology* 198.19 (2016), pp. 2553–2563.

[20] Roman Stocker. "Marine microbes see a sea of gradients". *science* 338.6107 (2012), pp. 628–633.

[21] RN Bearon and D Grünbaum. "Bioconvection in a stratified environment: experiments and theory". *Physics of Fluids* 18.12 (2006).

[22] Martin A Bees. "Advances in bioconvection". *Annual Review of Fluid Mechanics* 52 (2020), pp. 449–476.

[23] Albane Théry et al. "Self-organisation and convection of confined magnetotactic bacteria". *Scientific Reports* 10.1 (2020), p. 13578.

[24] Albane Théry, Alexander Chamolly, and Eric Lauga. "Controlling Confined Collective Organization with Taxis". *Physical Review Letters* 132.10 (2024), p. 108301.

[25] Benoit Vincenti et al. "Magnetotactic bacteria in a droplet self-assemble into a rotary motor". *Nature communications* 10.1 (2019), p. 5082.

[26] Jonathan Sharples et al. "Phytoplankton distribution and survival in the thermocline". *Limnology and Oceanography* 46.3 (2001), pp. 486–496.

[27] Bieito Fernández Castro et al. "Inhibited vertical mixing and seasonal persistence of a thin cyanobacterial layer in a stratified lake". *Aquatic Sciences* 83.2 (2021), p. 38.

[28] Jiayi Deng et al. "Motile bacteria at oil–water interfaces: Pseudomonas aeruginosa". *Langmuir* 36.25 (2020), pp. 6888–6902.

[29] Guruprakash Subbiahdoss and Erik Reimhult. "Biofilm formation at oil-water interfaces is not a simple function of bacterial hydrophobicity". *Colloids and Surfaces B: Biointerfaces* 194 (2020), p. 111163.

[30] Lisa Voskuhl and Janina Rahlff. "Natural and oil surface slicks as microbial habitats in marine systems: A mini review". *Frontiers in Marine Science* 9 (2022), p. 1020843.

[31] Alexander Morozov and Davide Marenduzzo. "Enhanced diffusion of tracer particles in dilute bacterial suspensions". *Soft Matter* 10.16 (2014), pp. 2748–2758.

[32] GL Miño et al. "Induced diffusion of tracers in a bacterial suspension: theory and experiments". *Journal of Fluid Mechanics* 729 (2013), pp. 423–444.

[33] Tobias Sommer et al. "Bacteria-induced mixing in natural waters". *Geophysical Research Letters* 44.18 (2017), pp. 9424–9432.

[34] Arnold J. T. M. Mathijssen, Raphaël Jeanneret, and Marco Polin. "Universal entrainment mechanism controls contact times with motile cells". *Phys. Rev. Fluids* 3 (3 2018), p. 033103. DOI: 10.1103/PhysRevFluids.3.033103. URL: https://link.aps.org/doi/10.1103/PhysRevFluids.3.033103.

[35] Oscar Sepúlveda Steiner, Damien Bouffard, and Alfred Wüest. "Persistence of bioconvection-induced mixed layers in a stratified lake". *Limnology and Oceanography* 66.4 (2021), pp. 1531–1547.

[36] Stefano Simoncelli, Stephen J Thackeray, and Danielle J Wain. "On biogenic turbulence production and mixing from vertically migrating zooplankton in lakes". *Aquatic Sciences* 80 (2018), pp. 1–12.

[37] Ranjiangshang Ran et al. "Bacteria hinder large-scale transport and enhance small-scale mixing in time-periodic flows". *Proceedings of the National Academy of Sciences* 118.40 (2021), e2108548118.

[38] Jaspreet Singh et al. "Bacterial activity hinders particle sedimentation". *Soft Matter* 17.15 (2021), pp. 4151–4160.

[39] Viktor Škultéty et al. "Hydrodynamic instabilities in a 2-D sheet of microswimmers embedded in a 3-D fluid". *arXiv:2302.13966* (2023).

[40] Sergey Belan and Mehran Kardar. "Pair dispersion in dilute suspension of active swimmers". *The Journal of Chemical Physics* 150.6 (2019).

[41] Gabriel Aguayo et al. "Floating active carpets drive transport and aggregation in aquatic ecosystems". *arXiv preprint arXiv:2312.11764* (2023).

[42] Shreyas Gokhale et al. "Dynamic clustering of passive colloids in dense suspensions of motile bacteria". *Physical Review E* 105.5 (2022), p. 054605.

[43] Pragya Kushwaha et al. "Phase separation of passive particles in active liquids". *Physical Review E* 108.3 (2023), p. 034603.

[44] Robert Großmann et al. "Non-Gaussian displacements in active transport on a carpet of motile cells". *Physical Review Letters* 132.8 (2024), p. 088301.

[45] Francisca Guzmán-Lastra, Hartmut Löwen, and Arnold JTM Mathijssen. "Active carpets drive non-equilibrium diffusion and enhanced molecular fluxes". *Nature Communications* 12.1 (2021), p. 1906.

[46] Cristian Villalobos et al. "Recovering the activity parameters of an active fluid confined in a sphere". *arXiv preprint arXiv:2403.11933* (2024).

[47] Xiaoxuan Zhang et al. "Tailoring flexible arrays for artificial cilia actuators". *Advanced Intelligent Systems* 3.10 (2021), p. 2000225.

[48] Anne Helene Gelebart et al. "Photoresponsive fiber array: Toward mimicking the collective motion of cilia for transport applications". *Advanced Functional Materials* 26.29 (2016), pp. 5322–5327.

[49] Ye Wang et al. "A continuous roll-pulling approach for the fabrication of magnetic artificial cilia with microfluidic pumping capability". *Lab on a Chip* 16.12 (2016), pp. 2277–2286.

[50] Fanlong Meng et al. "Magnetically-actuated artificial cilium: a simple theoretical model". *Soft Matter* 15.19 (2019), pp. 3864–3871.

[51] Vinayak V Khatavkar et al. "Active micromixer based on artificial cilia". *Physics of Fluids* 19.8 (2007).

[52] Stefano Simoncelli, Stephen J Thackeray, and Danielle J Wain. "Can small zooplankton mix lakes?" *Limnology and Oceanography Letters* 2.5 (2017), pp. 167–176.

[53] Eric Kunze. "Biologically generated mixing in the ocean". *Annual review of marine science* 11 (2019), pp. 215–226.

[54] AM Ardekani and R Stocker. "Stratlets: low Reynolds number point-force solutions in a stratified fluid". *Physical review letters* 105.8 (2010), p. 084502.

[55] Gregory L Wagner, William R Young, and Eric Lauga. "Mixing by microorganisms in stratified fluids". *Journal of Marine Research* 72.2 (2014), pp. 47–72.

[56] Shiyan Wang and Arezoo M Ardekani. "Biogenic mixing induced by intermediate Reynolds number swimming in stratified fluids". *Scientific reports* 5.1 (2015), p. 17448.

[57] Daisuke Noto and Hugo N Ulloa. "Simple tracking of occluded self-propelled organisms". *Measurement Science and Technology* 35.3 (2023), p. 035705.

[58] Isabel A Houghton et al. "Vertically migrating swimmers generate aggregation-scale eddies in a stratified column". *Nature* 556.7702 (2018), pp. 497–500.

[59] R Ouillon et al. "Active swimmers interacting with stratified fluids during collective vertical migration". *Journal of Fluid Mechanics* 902 (2020), A23.

[60] Eric Lauga. *The fluid dynamics of cell motility*. Vol. 62. Cambridge University Press, 2020.

[61] George Gabriel Stokes et al. *On the effect of the internal friction of fluids on the motion of pendulums*. Pitt Press Cambridge, 1851.

[62] Arnold Sommerfield. "Ein beitrag zur hydrodynamischen erklarung der turbulenten flussigkeisbewegung". *Atti Congr. Int. Math. 4th* (1908).

[63] Geoffrey Ingram Taylor. "Analysis of the swimming of microscopic organisms". *Proceedings of the Royal Society of London. Series A. Mathematical and Physical Sciences* 209.1099 (1951), pp. 447–461.

[64] Edward M Purcell. "Life at low Reynolds number". *American journal of physics* 45.1 (1977), pp. 3–11.

[65] GJ Hancock. "The self-propulsion of microscopic organisms through liquids". *Proceedings of the Royal Society of London. Series A. Mathematical and Physical Sciences* 217.1128 (1953), pp. 96–121.

[66] John Happel and Howard Brenner. *Low Reynolds number hydrodynamics: with special applications to particulate media*. Vol. 1. Springer Science & Business Media, 2012.

[67] Sangtae Kim and Seppo J Karrila. *Microhydrodynamics: principles and selected applications*. Courier Corporation, 2013.

[68] GK Batchelor. "The stress system in a suspension of force-free particles". *Journal of fluid mechanics* 41.3 (1970), pp. 545–570.

[69] Knut Drescher et al. "Direct measurement of the flow field around swimming microorganisms". *Physical Review Letters* 105.16 (2010), p. 168101.

[70] K. Drescher et al. "Fluid dynamics and noise in bacterial cell–cell and cell–surface scattering". *Proceedings of the National Academy of Sciences* 108.27 (2011), pp. 10940–10945.

[71] Saverio E Spagnolie. "Complex fluids in biological systems". *Biological and Medical Physics, Biomedical Engineering* (2015).

[72] Eric Lauga and Sébastien Michelin. "Stresslets induced by active swimmers". *Physical review letters* 117.14 (2016), p. 148001.

[73] David Saintillan. "Rheology of active fluids". *Annual Review of Fluid Mechanics* 50 (2018), pp. 563–592.

[74] Jeffrey S Guasto and Karl A Johnson. "Oscillatory flows induced by microorganisms swimming in two dimensions". *Physical review letters* 105.16 (2010), p. 168102.

[75] Raymond E Goldstein. "Green algae as model organisms for biological fluid dynamics". *Annual review of fluid mechanics* 47 (2015), pp. 343–375.

[76] Suddhashil Chattopadhyay et al. "Swimming efficiency of bacterium Escherichia coli". *Proceedings of the National Academy of Sciences* 103.37 (2006), pp. 13712–13717.

[77] Nicholas C Darnton et al. "On torque and tumbling in swimming Escherichia coli". *Journal of bacteriology* 189.5 (2007), pp. 1756–1764.

[78] Robert Brown. "XXVII. A brief account of microscopical observations made in the months of June, July and August 1827, on the particles contained in the pollen of plants; and on the general existence of active molecules in organic and inorganic bodies". *The philosophical magazine* 4.21 (1828), pp. 161–173.

[79] Pawel Romanczuk et al. "Active Brownian particles: From individual to collective stochastic dynamics". *The European Physical Journal Special Topics* 202 (2012), pp. 1–162.

[80] Gouy. "Note sur le mouvement brownien". *Journal de Physique Théorique et Appliquée* 7.1 (1888), pp. 561–564.

[81] Albert Einstein. "Über die von der molekularkinetischen Theorie der Wärme geforderte Bewegung von in ruhenden Flüssigkeiten suspendierten Teilchen". *Annalen der physik* 4 (1905).

[82] Albert Einstein. "Zur theorie der brownschen bewegung". *Annalen der physik* 324.2 (1906), pp. 371–381.

[83] Marian Von Smoluchowski. "Zur kinetischen theorie der brownschen molekularbewegung und der suspensionen". *Annalen der physik* 326.14 (1906), pp. 756–780.

[84] Chen-Pang Yeang. *Transforming Noise: A History of Its Science and Technology from Disturbing Sounds to Informational Errors, 1900-1955*. Oxford University Press, 2024.

[85] Jean Perrin. *Les atomes*. CNRS éditions, 1909.

[86] Paul Langevin et al. "Sur la théorie du mouvement brownien". *CR Acad. Sci. Paris* 146.530-533 (1908), p. 530.

[87] George E Uhlenbeck and Leonard S Ornstein. "On the theory of the Brownian motion". *Physical review* 36.5 (1930), p. 823.

[88] Ludwig Eduard Boltzmann. *Einige allgemeine sätze über Wärmegleichgewicht*. K. Akad. der Wissensch., 1871.

[89] Adolf Fick. "Ueber Diffusion". *Annalen der Physik* 170.1 (1855), pp. 59–86. DOI: https://doi.org/10.1002/andp.18551700105. eprint: https://onlinelibrary.wiley.com/doi/pdf/10.1002/andp.18551700105. URL: https://onlinelibrary.wiley.com/doi/abs/10.1002/andp.18551700105.

[90] Herbert B Callen and Theodore A Welton. "Irreversibility and generalized noise". *Physical Review* 83.1 (1951), p. 34.

[91] Rep Kubo. "The fluctuation-dissipation theorem". *Reports on progress in physics* 29.1 (1966), p. 255.

[92] Sriram Ramaswamy. "The mechanics and statistics of active matter". *Annu. Rev. Condens. Matter Phys.* 1.1 (2010), pp. 323–345.

[93] Karl Przibram. "Über die ungeordnete Bewegung niederer Tiere". *Pflüger's Archiv für die gesamte Physiologie des Menschen und der Tiere* 153.8 (1913), pp. 401–405.

[94] Karl Przibram. "Über die ungeordnete Bewegung niederer Tiere. II". *Archiv für Entwicklungsmechanik der Organismen* 43.1 (1917), pp. 20–27.

[95] Reinhold Fürth. "Die brownsche bewegung bei berücksichtigung einer persistenz der bewegungsrichtung. mit anwendungen auf die bewegung lebender infusorien". *Zeitschrift für Physik* 2.3 (1920), pp. 244–256.

[96] Jonathan R Howse et al. "Self-motile colloidal particles: from directed propulsion to random walk". *Physical review letters* 99.4 (2007), p. 048102.

[97] Vladimir Lobaskin, Dmitry Lobaskin, and IM Kulić. "Brownian dynamics of a microswimmer". *The European Physical Journal Special Topics* 157.1 (2008), pp. 149–156.

[98] Borge ten Hagen, Sven van Teeffelen, and Hartmut Löwen. "Brownian motion of a self-propelled particle". *Journal of Physics: Condensed Matter* 23.19 (2011), p. 194119.

[99] M Reza Shaebani et al. "Computational models for active matter". *Nature Reviews Physics* 2.4 (2020), pp. 181–199.

[100] Hartmut Löwen. "Inertial effects of self-propelled particles: From active Brownian to active Langevin motion". *The Journal of chemical physics* 152.4 (2020).

[101] Jens Elgeti, Roland G Winkler, and Gerhard Gompper. "Physics of microswimmers—single particle motion and collective behavior: a review". *Reports on progress in physics* 78.5 (2015), p. 056601.

[102] Andreas Zöttl and Holger Stark. "Emergent behavior in active colloids". *Journal of Physics: Condensed Matter* 28.25 (2016), p. 253001.

[103] Matthew T Downton and Holger Stark. "Simulation of a model microswimmer". *Journal of Physics: Condensed Matter* 21.20 (2009), p. 204101.

[104] Xu Zheng et al. "Non-Gaussian statistics for the motion of self-propelled Janus particles: Experiment versus theory". *Physical Review E—Statistical, Nonlinear, and Soft Matter Physics* 88.3 (2013), p. 032304.

[105] Clemens Bechinger et al. "Active particles in complex and crowded environments". *Reviews of modern physics* 88.4 (2016), p. 045006.

[106] Giorgio Volpe, Sylvain Gigan, and Giovanni Volpe. "Simulation of the active Brownian motion of a microswimmer". *American journal of physics* 82.7 (2014), pp. 659–664.

[107] Howard C Berg. *E. coli in Motion*. Springer, 2004.

[108] Julio Bastos-Arrieta et al. "Bacterial biohybrid microswimmers". *Frontiers in Robotics and AI* 5 (2018), p. 97.

[109] Linda Turner, William S Ryu, and Howard C Berg. "Real-time imaging of fluorescent flagellar filaments". *Journal of bacteriology* 182.10 (2000), pp. 2793–2801.

[110] Howard C Berg. *Random walks in biology*. Princeton University Press, 1993.

[111] Jonathan Saragosti, Pascal Silberzan, and Axel Buguin. "Modeling E. coli tumbles by rotational diffusion. Implications for chemotaxis". *PloS one* 7.4 (2012), e35412.

[112] S Tavaddod et al. "Probing passive diffusion of flagellated and deflagellated Escherichia coli". *The European Physical Journal E* 34 (2011), pp. 1–7.

[113] Jeffrey S Guasto, Roberto Rusconi, and Roman Stocker. "Fluid mechanics of planktonic microorganisms". *Annual Review of Fluid Mechanics* 44.1 (2012), pp. 373–400.

[114] Marco Polin et al. "Chlamydomonas swims with two "gears" in a eukaryotic version of run-and-tumble locomotion". *Science* 325.5939 (2009), pp. 487–490.

[115] Rachel R Bennett and Ramin Golestanian. "A steering mechanism for phototaxis in Chlamydomonas". *Journal of The Royal Society Interface* 12.104 (2015), p. 20141164.

[116] J Gachelin et al. "Collective motion in an active suspension of Escherichia coli bacteria". *New Journal of Physics* 16.2 (2014), p. 025003.

[117] Arnold JTM Mathijssen, Dmitri O Pushkin, and Julia M Yeomans. "Tracer trajectories and displacement due to a micro-swimmer near a surface". *Journal of Fluid Mechanics* 773 (2015), pp. 498–519.

[118] K Aderogba and JR Blake. "Action of a force near the planar surface between two semi-infinite immiscible liquids at very low Reynolds numbers". *Bulletin of the Australian Mathematical Society* 18.3 (1978), pp. 345–356.

[119] Saverio E Spagnolie and Eric Lauga. "Hydrodynamics of self-propulsion near a boundary: predictions and accuracy of far-field approximations". *Journal of Fluid Mechanics* 700 (2012), pp. 105–147.

[120] Allen T Chwang and T Yao-Tsu Wu. "Hydromechanics of low-Reynolds-number flow. Part 2. Singularity method for Stokes flows". *Journal of Fluid mechanics* 67.4 (1975), pp. 787–815.

[121] Miki Hondzo et al. "Measurement and scaling of lake surface skin temperatures". *Geophysical Research Letters* 49.6 (2022), e2021GL093226.

[122] Vaseem A Shaik and Gwynn J Elfring. "Hydrodynamics of active particles in viscosity gradients". *Physical Review Fluids* 6.10 (2021), p. 103103.

[123] Marianne G Petrino and RN Doetsch. "'Viscotaxis', a new behavioural response of Leptospira interrogans (biflexa) strain B16". *Microbiology* 109.1 (1978), pp. 113–117.

[124] M Yu Sherman, EO Timkina, and AN Glagolev. "Viscosity taxis in Escherichia coli". *FEMS Microbiology Letters* 13.2 (1982), pp. 137–140.

[125] Charu Datt and Gwynn J Elfring. "Active particles in viscosity gradients". *Physical Review Letters* 123.15 (2019), p. 158006.

[126] Benno Liebchen et al. "Viscotaxis: Microswimmer navigation in viscosity gradients". *Physical review letters* 120.20 (2018), p. 208002.

[127] Marcos et al. "Bacterial rheotaxis". *Proceedings of the National Academy of Sciences* 109.13 (2012), pp. 4780–4785.

[128] Gabriel Ramos, María Luisa Cordero, and Rodrigo Soto. "Bacteria driving droplets". *Soft Matter* 16.5 (2020), pp. 1359–1365.

[129] Magdalena M Mrokowska, Anna Krztoń-Maziopa, and Maciej Dbowski. "Effect of exopolymer gels on the viscoelasticity of mucus-rich saltwater and settling dynamics of particles". *Marine Chemistry* 246 (2022), p. 104163.

[130] Marco G Mazza. "The physics of biofilms—an introduction". *Journal of Physics D: Applied Physics* 49.20 (2016), p. 203001.

[131] Hugo N Ulloa and Juvenal A Letelier. "Energetics and mixing of thermally driven flows in Hele-Shaw cells". *Journal of Fluid Mechanics* 930 (2022), A16.

[132] Daisuke Noto, Juvenal A Letelier, and Hugo N Ulloa. "Plume-scale confinement on thermal convection". *Proceedings of the National Academy of Sciences* 121.28 (2024), e2403699121.

[133] Isabel A Houghton and John O Dabiri. "Alleviation of hypoxia by biologically generated mixing in a stratified water column". *Limnology and Oceanography* 64.5 (2019), pp. 2161–2171.

[134] Bieito Fernandez Castro et al. "Intense upper ocean mixing due to large aggregations of spawning fish". *Nature Geoscience* 15.4 (2022), pp. 287–292.

[135] Joshua Tamayo et al. "Swarming bacterial fronts: Dynamics and morphology of active swarm interfaces propagating through passive frictional domains". *Biophysical Journal* 123.3 (2024), 541a.

[136] Dóra Bárdfalvy et al. "Collective motion in a sheet of microswimmers". *arXiv preprint arXiv:2310.05554* (2023).

[137] Debasmita Mondal et al. "Strong confinement of active microalgae leads to inversion of vortex flow and enhanced mixing". *Elife* 10 (2021), e67663.

[138] Megumi Akashi et al. "Transition from convection rolls to large-scale cellular structures in turbulent Rayleigh-Bénard convection in a liquid metal layer". *Physical Review Fluids* 4.3 (2019), p. 033501.

[139] Daisuke Noto, Hugo N Ulloa, and Juvenal A Letelier. "Reconstructing temperature fields for thermally-driven flows under quasi-steady state". *Experiments in Fluids* 64.4 (2023), p. 74.

[140] Arnold JTM Mathijssen et al. “Culinary fluid mechanics and other currents in food science”. *Reviews of Modern Physics* 95.2 (2023), p. 025004.

[141] Vani Mohit et al. “Hidden biofilms in a far northern lake and implications for the changing Arctic”. *npj Biofilms and Microbiomes* 3.1 (2017), p. 17.

[142] Alexandre M Anesio et al. “The microbiome of glaciers and ice sheets”. *npj Biofilms and Microbiomes* 3.1 (2017), p. 10.

[143] Alberto de la Fuente. “Heat and dissolved oxygen exchanges between the sediment and water column in a shallow salty lagoon”. *Journal of Geophysical Research: Biogeosciences* 119.4 (2014), pp. 596–613.

[144] Tom J Battin et al. “The ecology and biogeochemistry of stream biofilms”. *Nature Reviews Microbiology* 14.4 (2016), pp. 251–263.

[145] Nuris Figueroa-Morales et al. “Mechanical shear controls bacterial penetration in mucus”. *Scientific reports* 9.1 (2019), p. 9713.

[146] Gilberto E Flores et al. “Diversity, distribution and sources of bacteria in residential kitchens”. *Environmental microbiology* 15.2 (2013), pp. 588–596.

[147] Monika Novak Babič, Cene Gostinčar, and Nina Gunde-Cimerman. “Microorganisms populating the water-related indoor biome”. *Applied microbiology and biotechnology* 104 (2020), pp. 6443–6462.

Appendix A

Elements of Fluid Mechanics

A.1 Velocity gradient tensor

$$\nabla \boldsymbol{u} = \frac{\partial u_i}{\partial x_j} = \begin{pmatrix} \frac{\partial u_1}{\partial x_1} & \frac{\partial u_1}{\partial x_2} & \frac{\partial u_1}{\partial x_3} \\ \frac{\partial u_2}{\partial x_1} & \frac{\partial u_2}{\partial x_2} & \frac{\partial u_2}{\partial x_3} \\ \frac{\partial u_3}{\partial x_1} & \frac{\partial u_3}{\partial x_2} & \frac{\partial u_3}{\partial x_3} \end{pmatrix} \tag{A.1.1}$$

A.2 Strain rate tensor

In vector notation, $\boldsymbol{E} = \frac{1}{2}\left(\nabla \boldsymbol{u} + (\nabla \boldsymbol{u})^{\mathrm{T}}\right)$ for an incompressible fluid, $\nabla \cdot \boldsymbol{u} = 0$

$$E_{ij} = \frac{1}{2}\left(\frac{\partial u_i}{\partial x_j} + \frac{\partial u_j}{\partial x_i}\right) = \begin{pmatrix} \frac{\partial u_1}{\partial x_1} & \frac{1}{2}\left(\frac{\partial u_1}{\partial x_2} + \frac{\partial u_2}{\partial x_1}\right) & \frac{1}{2}\left(\frac{\partial u_1}{\partial x_3} + \frac{\partial u_3}{\partial x_1}\right) \\ \frac{1}{2}\left(\frac{\partial u_2}{\partial x_1} + \frac{\partial u_1}{\partial x_2}\right) & \frac{\partial u_2}{\partial x_2} & \frac{1}{2}\left(\frac{\partial u_2}{\partial x_3} + \frac{\partial u_3}{\partial x_2}\right) \\ \frac{1}{2}\left(\frac{\partial u_3}{\partial x_1} + \frac{\partial u_1}{\partial x_3}\right) & \frac{1}{2}\left(\frac{\partial u_3}{\partial x_2} + \frac{\partial u_2}{\partial x_3}\right) & \frac{\partial u_3}{\partial x_3} \end{pmatrix} \tag{A.2.1}$$